EMPLOYING SHEAR INDUCED HYDRODYNAMIC LIFT TO ACHIEVE SIEVE-FREE SEPARATION BASED ON SIZE IN CROSS-FLOW FILTRATION

A Thesis

Presented to the Faculty of the Graduate School

of Cornell University

In Partial Fulfillment of the Requirements for the Degree of

Master of Science in Chemical Engineering

By

Sharanya Subramony

August 2017

ABSTRACT

Cross-flow filtration is a high throughput method of separating particles (including cells and macromolecules) from fluid and from smaller sized particles. This study has two major purposes: (1) to demonstrate experimentally that lift-based cross-flow techniques allow for sieve-free separation based on size that follow the theoretical predictions and (2) investigate the effects of an alternative sieve-free separation mechanism based on ratcheting of particle trajectories. Through utilizing the shear rates accessible in cross flow filtration along with control of the permeate, feed and retentate fluxes, we can precisely regulate the transmission of particles through membranes with pore sizes about 10 times larger than the particle diameter by utilizing transport processes occurring in the channel. By increasing the shear rate, the transmission of particles through the membrane significantly decreases, and the decrease follows the theoretical predictions for inertial lift based separation. Additionally, adjusting to lower permeate flux allows for less transmission of particles. The trends exhibited for the transmission as a function of parameters such as shear rate, permeate flux, etc. agree with the theoretically predicted trends. The study shows the critical shear rates and permeate fluxes that allow only ~1% of the particles to transmit through the membrane, which optimizes selectivity. Finally, the sieve free separation mechanism based on the ratcheting of particle trajectories is investigated. This mechanism can lead to sieve-free separation of nanoparticles or proteins which are too small to separate based on hydrodynamic lift. Using 1.5 nm and 3.4 nm nano-spheres, we can show that at shear rates that would have no inertial lift effects on the particles, there is some evidence of particle retention and separation. A mechanistic understanding of sieve-free separation of proteins could enable cross-flow separation of product proteins in the bio-pharmaceutical industry, while lift based separation can reduce fouling in waste water recovery.

BIOGRAPHICAL SKETCH

Sharanya got her B.Sc degree from Drexel University in 2015 and completed her M.Eng from Cornell University in 2016. She is currently a MS student in the Chemical and Biological Engineering department under the supervision of Dr. Donald Koch. Her main research interest is in experimental studies dealing with membrane separation and purification.

ACKNOWLEDGEMENTS

I would like to give my thanks to Professor Koch, Professor Hurwitz, and Professor Cathles for their guidance in my research. I would also like to express my appreciation for Pall Corporation for providing the materials and cross-flow equipment required to conduct this research project. A big thank you to Yuxi Chen for assisting me with some of the experiments. Finally, I would like to thank my family for supporting me.

TABLE OF CONTENTS

Page

LIST OF FIGURES

LIST OF TABLES

LIST OF ABBREVIATIONS

RAMS – Research and Modeling System

ppm – parts per million

RO – Reverse Osmosis

RPM – Revolutions per minute

VFD – Variable frequency drive

Hp – Horsepower

BSA – Bovine Serum Albuminum

LIST OF SYMBOLS

μ	Viscosity
ω	Angular velocity
ν	Kinematic viscosity
ρ	Density
γ	Shear rate
R_P	Pore radius
a	Particle radius
Pe	Peclet number
Re	Reynolds number
Re_p	Particle Reynolds number
Φ	Porosity
ϕ	Particle volume fraction
ϕ_b	Bulk volume fraction
v_L	Lift velocity
v_p	Permeate velocity
D	Particle diffusivity

D_{B0}	Brownian diffusivity
D_H	Hydrodynamic diffusivity
D_E	Eddy diffusivity
r_2	Radius of outer cylinder
r_1	Radius of inner cylinder
A	Area of membrane
q	Particle flux through the membrane pore
d	Diameter of pore
R_G	Porous medium grain radii
C_b	Transmission ratio based on bulk volume fraction
C	Transmission ratio
P	Pressure
σ	Surface tension
Q	Dimensionless fluid flux through the pore
v	Particle velocity
y	Coordinate normal to the porous surface

Chapter 1

Introduction

1.1 Overview

Cross-flow filtration is a high throughput method of separating particles (including cells and macromolecules) from fluid and from smaller sized particles using pores that are the same size as the particles that are to be separated. The process occurs by having an incoming feed stream that passes tangentially across the surface of a membrane, rather than into the filter[1]. This counteracts transport of particles by filtrate flow towards the membrane and limits their accumulation on its surface and in its pore structure[2]. The primary goal of our study is to show that cross flow filtration can separate particles when using membranes whose pores are significantly larger than the particles to be separated. This can otherwise be termed as "sieve-free" separation. The way this is done is to utilize hydrodynamic processes in the system to lift the particles away from the membrane and extract nearly pure fluid. In addition, we also want to show that sieve-free separation can also occur with nanoparticles by showing that the particles ratchet the surface of the membrane and move away from the pores. This study has two major purposes: (1) to demonstrate experimentally that lift-based cross-flow techniques allow for sieve-free separation based on size that follow the theoretical predictions and (2) investigate the effects of an alternative sieve-free separation mechanism based on ratcheting of particle trajectories for nanoparticles.

Cross-flow filtration is typically selected for feeds containing a high proportion of small solid particles. The primary disadvantages to this method are that the membrane will tend to get fouled frequently and there is a lack of selectivity in separation. Figure 1.1 shows a schematic of the conventional operation of cross-flow filtration.

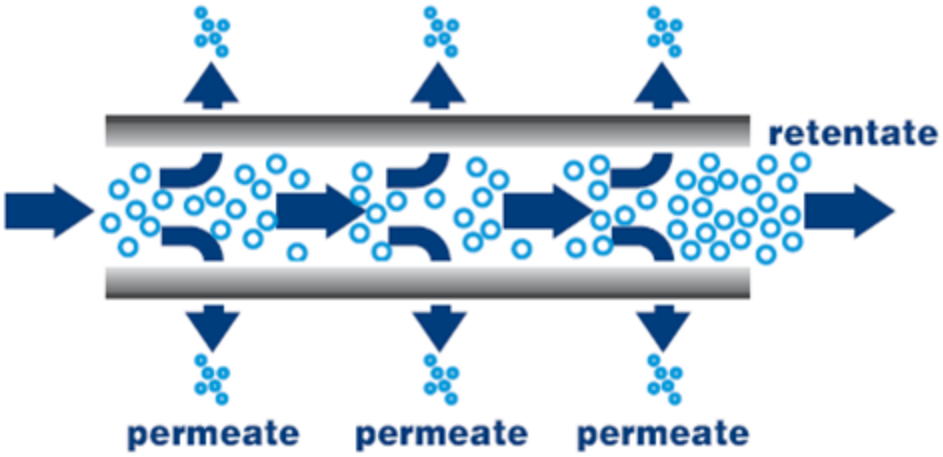

Figure 1.1: Schematic of cross-flow filtration[3]

An approach to overcome these disadvantages and improve the quality of separation is to utilize hydrodynamic transport processes in the channel rather than just membrane exclusion as in conventional methods. The membrane used in the optimized process will have pore diameters that are significantly larger than the largest particle diameter present in the solution and thus can be termed as "sieve-free membranes". Theoretical models have been developed to describe the roles of molecular diffusion[4], shear-induced hydrodynamic interactions[5,6] and inertial lift[7] in limiting the accumulation of particles near the membrane surface. However, they use membranes that have pores smaller than the particle that they want to separate. This means that the particles can be lifted away from the membrane due to hydrodynamic lift, but the particles tend to get stuck in the pores or adsorbed on the membrane surface, causing membrane fouling to occur eventually.

Cross-flow filtration generates high shear, which induces a shear-induced diffusion in the boundary layer above the membrane[4]. This force counters the drag of the particles towards the membrane and thus separation can be achieved for particles larger than 200 nm. For shear induced diffusion to work the turbulent effects in the fluid needs to be minimal. This means that there

should be slight turbulent effects, but not so much that it induces fluid instabilities, which make it hard to predict the particle behavior theoretically. For low turbulent effects, the shear rates need to be low enough, which corresponds to a low, for example have a low particle Reynolds number, which depends on the shear rate of the fluid and the particle radius. The significance behind having a low particle Reynolds number will be discussed later.

For particles that are smaller than 200 nm, separation based on trajectory ratcheting is investigated. Typically, these sizes of particles will follow the fluid streamline and thus experience a drag force as it moves from one pore to the next. However, the particle can also experience a short-range repulsive interaction with the membrane, causing it to be displaced upward from the surface by the order of its radius, a [20]. If the displacement is larger than the downward drag, then the particle can stay above the membrane and essentially ratchet along the surface. Figure 1.2 shows a mechanism for trajectory based ratcheting as represented by the blue line.

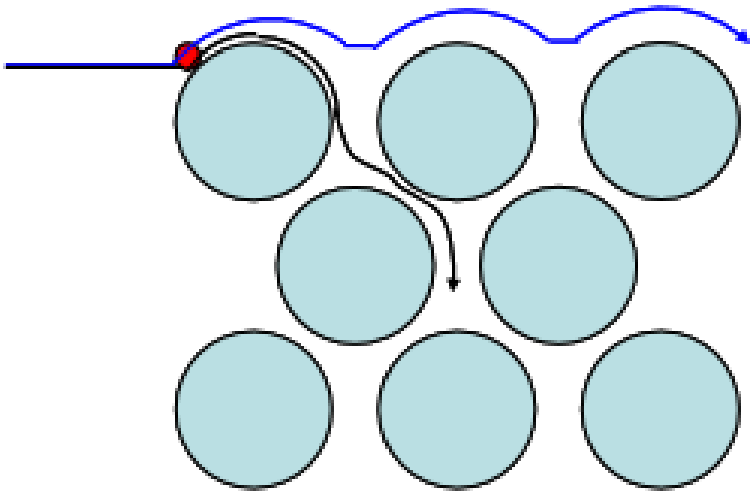

Figure 1.2: Sketch of particle trajectory ratcheting. The blue circles represent grains that make up the porous media

A potential shortcoming to using sieve-free operations is the need to have higher operating (pumping) costs due to the need to exceed a critical flow rate. However, it has been shown that these additional costs can be counterbalanced by lower capital costs. Also, sieve free membranes exhibit very little to no fouling, which not only reduces the membrane area required, but also reduces cleaning and membrane replacement costs. Minimizing membrane replacement costs is an important economic driver, especially in water filtration, where porous membranes are used as pre-filters to protect expensive dense film reverse osmosis (RO) membranes.

1.2 Background

To date, there has been no experimental demonstration of inertial lift based sieve free separation for micron sized particles in both laminar and turbulent regimes. This is a significant size range of particles to explore because in typical industrial applications, particles that typically need to be separated from the fluid are bacteria, other cells, and cell debris in the 0.5-5 μm range where shear lift can work. There have been a few experiments dealing with the idea of sieve-free separation [8,9,10,11], but the conditions under which they happened or the particles that were used are different from what we choose to study. For instance, Levesley and Bellhouse[9] conducted experiments of sieve-free separation using inertial lift forces, but they used particles that were about 0.5 mm and 0.74 mm in diameter and carried out their experiments using oscillatory laminar flow in a narrow rectangular channel. By using oscillatory flow, they controlled the shear rate by varying the frequency and amplitude of oscillation. van Dinther conducted sieve free cross-flow filtration experiments with emulsions of silicone oil that were in the size range of 2.7 – 5.5 μm[11], but focused the effect of separation based on the hydrodynamic particle-particle and particle-wall interactions and only conducted experiments in laminar flow regimes.

Another class of particles that are important to separate in industry are macromolecules in the 1-10 nm range. An experimental study done by Hurwitz and Brantley[10] showed that 1-3 nm sized globular proteins could be separated in a coarse membrane in the presence of strong shear flows. They had attributed the separation due to inertial lift, but theoretical calculations later showed that the size of the particles made the lift velocity negligible. An alternative explanation is that excluded volume interactions with the top surface of the membrane can keep the particles within the channel while the fluid passes through the pores. This mechanism can be referred to as particle-trajectory ratcheting separation. An experiment by van Dinther provided an additional demonstration of trajectory-ratcheting separation of yeast cells[8]. They used particles that were large enough to experience inertial lift (4 μm – 6 μm), but the shear rate provided was not high enough for the particles to achieve the needed lift velocity. In addition, the particle volume fraction was low to minimize particle-particle interaction. Despite the low shear rates, the yeast cells didn't flow through the membrane, which was attributed to the particles skimming or ratcheting along the surface of the membrane, However, van Dinther didn't take in to account the Brownian diffusion and particle shape, which are important factors when looking at it from an industrial standpoint and trying to theoretically predict trends.

1.3 Experimental objective

Spherical polystyrene beads 0.5 μm and 5 μm in diameter were used to simulate cells and other micron sized particles. Macromolecules were simulated by fluorescent carbon nanospheres with two sizes, 1.5 nm, and 3.4 nm, to investigate the effects of particle trajectory ratcheting. The cross-flow apparatus used was a Couette cell that had been custom made by Pall Corporation with the inner cylinder as the stationary porous structure and the outer cylinder providing the shear forces through spinning. The benefit of using a Couette cell is that is allows the independent control

of the shear rate at the membrane surface along with the feed, permeate and retentate fluxes. This allows for a better mechanistic understanding of the process.

As mentioned previously, this sieve-free experimental method will be an improvement on the current technology of cross-flow filtration with regards to reduction of fouling and improved selectivity in particle separation. One of the primary experimental objectives is to demonstrate that sieve-free cross flow filtration separation is possible when lift conditions are appropriate for separation of cells or other micron or protein particles by using more idealized particles than proteins and cells. The use of spherical particles, distinguishes current experiments from those of less ideally shaped particles. Our experiments differ from those of Hurwitz & Brantley and van Dinther by having higher shear rates.

A second objective is to provide understanding of the mechanism of separation by showing that the trends of the transmission ratio with shear rate, permeate velocity, particle size, and fluid regime are as one would expect physically and through theoretical calculations. We can show this by plotting the change/transition from inertial lift forces keeping the particle suspended in the retentate to the point at which the particles flow into the permeate stream. This is useful when the mixture being passed through the cell contains particles of different shapes and sizes. Knowing the transition state for each of the sizes of particles in various fluid regimes can allow parametric adjustments of the spin rates and flux rates in a way that they retain a certain size range of particles and the rest flow through the membrane pores.

Table 1: Summary of the experiments conducted

Experiment	Purpose
Laminar experiments using 5 μm spheres and a 50 μm membrane	Observe the effects of lift separation in the laminar regime and determine if separation is primarily due to the shear induced hydrodynamic interaction of the particles
Lift induced separation of 0.5 μm spheres in turbulent channel flows using a 5 μm porous membrane at different fluid viscosities	Observe the effects of hydrodynamic lift and turbulent diffusivity on particles and determine how change in centrifugal forces and viscosity affect the transmission of particles.
Lift induced separation of 0.5 μm spheres in turbulent channel flows using a 5 μm porous membrane	Observe the effects of hydrodynamic lift and turbulent diffusivity on particles smaller than 1 μm using a membrane that has pores 10 times larger than the particle diameter. Show that separation can be achieved over a range of shear rates and permeate velocities.
Lift induced separation of 0.5 μm spheres in turbulent channel flows using 10 μm and 20 μm porous membranes	Examine the effect of membrane pore diameter on hydrodynamic lift based separation.
Lift induced separation of 5 μm spheres in turbulent channel flows using a 20 μm porous membrane	Observe separation in the turbulent regime for particles that are large enough to experience very high lift velocities (~10^5) and very large Re (~10^5)
Sieve-free separation due to particle trajectory ratcheting using nanospheres (1.5 nm and 3.4 nm)	Determine if sieve-free separation can occur by trajectory particle ratcheting in the turbulent regime

Chapter two of the thesis will cover the methods and materials used for conducting the cross-flow experiments. An overview of the different membranes used along with the particles will be covered in this section. This will be followed by the theoretical predictions that outline the theory used to estimate the transmission ratio values for the different set of experimental conditions. Finally, the results will be shown with the experimental values along with the theoretical predictions obtained by using the theoretical equations. Further adjustments will be made to the theory and discussed for each of the cases laid out in Table 1 to match the theoretical predictions to the experimental results.

Chapter 2

Materials and Methodology

2.1 Cross-flow equipment schematic and layout

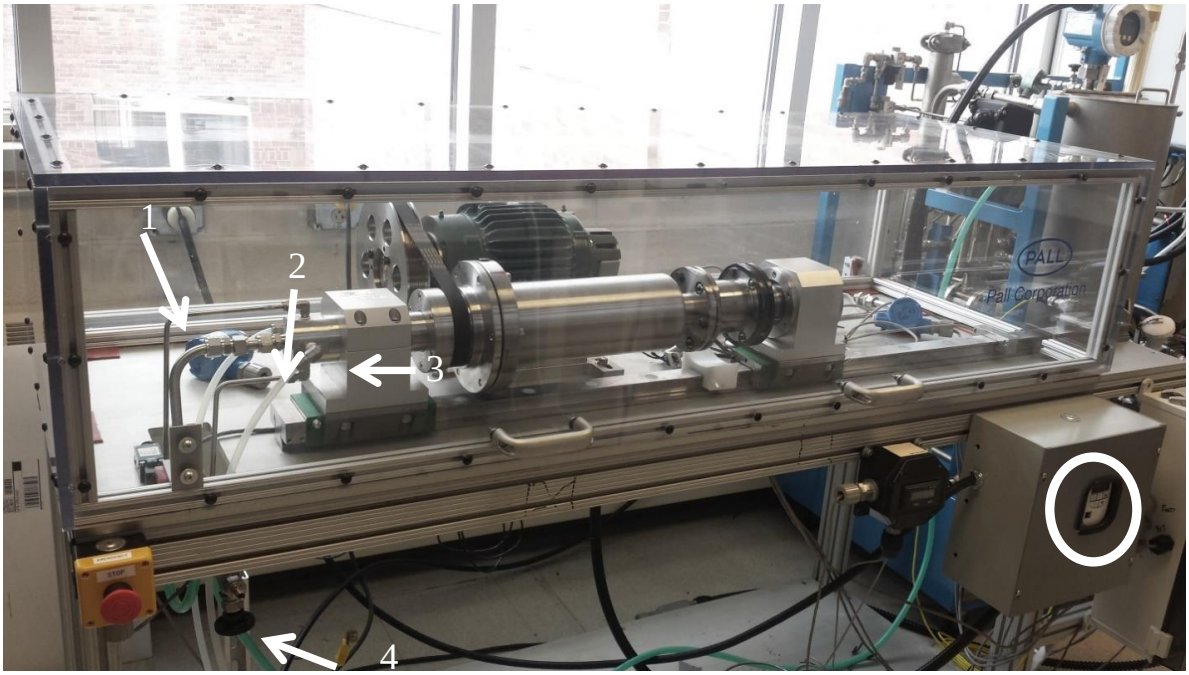

Figure 2.1: Layout of Cross-flow system supplied by Pall Corporation

Figure 2.1 shows the cross-flow system that has been donated by Pall Corporation to demonstrate the effects of hydrodynamic lift and particle trajectory ratcheting in sieve free cross-flow separation. The setup includes a rotating Couette cell filter in which the membrane is housed. Typically, cross-flow filtration is usually performed in a channel or hollow fiber geometry. The advantage of using a Couette cell geometry for these experiments allows for independent control of the shear rate at the membrane surface and the feed and permeate fluxes. The labeled arrows in Figure 2.1 indicate the ports through which the feed, retentate and permeate flow in and out of the system. The arrow labeled 1 in Figure 2.1 indicates the retentate outflow pipe. The arrow labeled 3 indicates one of the tubes, attached to the top and bottom of the cylinder, that carry the feed into

the Couette cell and surround the membrane. The arrow labeled 2 indicates one of the tubes that the permeate comes out of, which is connected to a valve indicated by the arrow labeled 4 shown in the bottom to collect samples of the permeate to measure the concentration and classify the permeate velocity. The retentate stream gets recycled back to the main feed tank (not shown in image) so that the process is continuous. The white circle indicates the variable frequency drive which controls the spin rate of the Couette cell and the shear rate of the fluid.

Figure 2.2 shows a cutaway of the precision machined Couette flow cell. The cell consists of three concentric cylinders. The outermost cylinder is a nonporous stainless-steel cylinder (5.4 cm radius and 30 cm height), which generates shear by rotating under digital frequency control at 10 RPM to 3600 RPM. The innermost cylinder is a non-rotating perforated stainless-steel tube through which the permeate flow is removed. The membrane is attached to a stainless steel porous cylinder that is attached to the innermost cylinder and sits between the outermost and innermost cylinder. The gap thickness between the surface of the membrane and rotating cylinder is about 10 mm. The feed inflow is the red path, the green is the retentate outflow and the blue path is the permeate outflow.

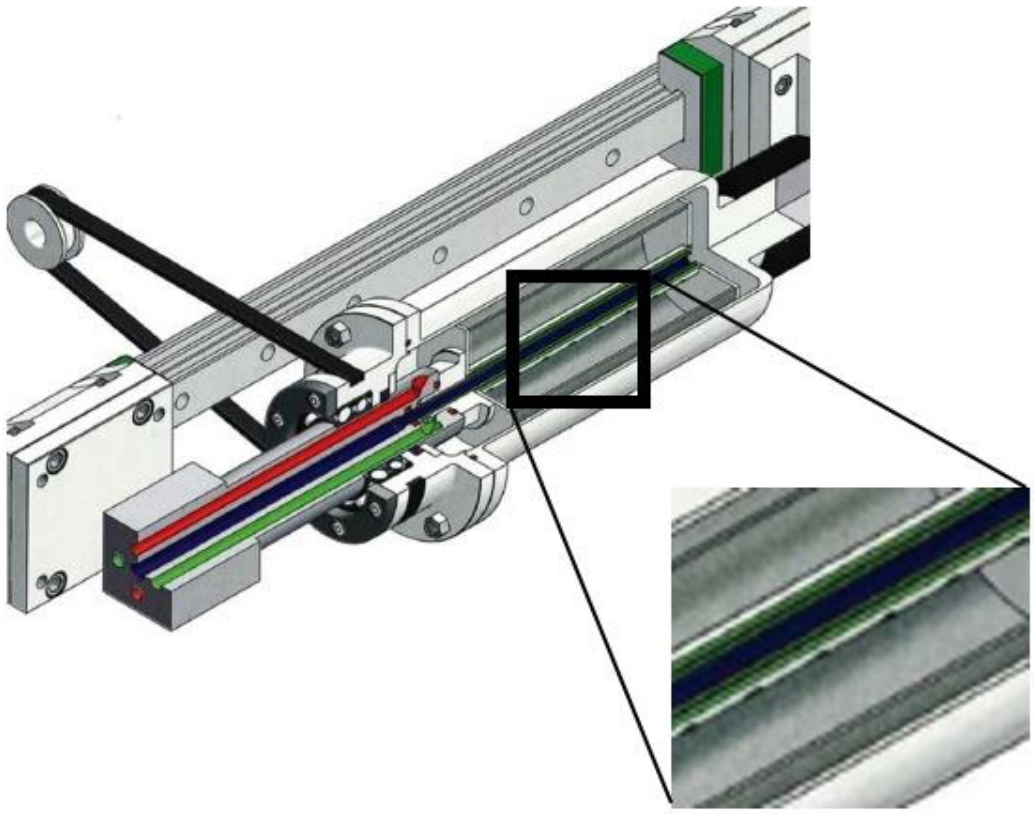

Figure 2.2: Couette cell filter cutaway

The motor being used to spin the Couette cell has a maximum power rating of 1.5 Hp, which sets a cap for spin that can be generated by the system. The system provides automated control of the spin rate and automated flow control valves for the suspension feed, retentate and permeate flow rates. Laminar flow experiments can be done for shear rates in the range of 15 to 2,000 s^{-1} and turbulent flow experiments can be done for shear rates of 7,000 to 200,000 s^{-1}. For laminar experiments, the gap thickness needs to be minimized to around 1 mm to prevent turbulent effects and run experiments under reasonable shear conditions. This is done by 3D printing a plastic sleeve with a lattice structure to increase the diameter of the stationary cylinder. The nylon membrane used for laminar experiments is secured over to the sleeve. This 3D printed sleeve is also used for the turbulent experiments with the nanospheres, with the 100 kDa membrane being wrapped around the printed sleeve.

The bulk feed is stored and pumped into the Couette cell using a separate research and modeling scale (RAMs) cross-flow system, also donated by Pall corporation. On its own, the system functions as a small-scale industrial hollow fiber cross-flow system. For our experiments, only the 30-gallon feed tank and the centrifugal pump is used. The feed flow rate and subsequently the cross-flow velocity is controlled manually using a variable frequency drive (VFD) control unit. The fluid that passes through the retentate gets recycled back to the tank to ensure a closed and continuous system. For all the experiments, we want to operate in a mode with little to no variation of the particle volume fraction along the axis of the Couette cell. This is done by ensuring that the volumetric flow of the permeate is small compared to the volumetric flow of the retentate. Consequently, we also ensure that the retentate flow is small enough that the shear is dominated by the rotation of the Couette and not by the flow of the feed and retentate through the gap. The axial shear was calculated for the feed flow rates used to ensure that it was significantly lower than the shear rates caused by rotation of the Couette cell. The feed flow rates used for both turbulent and laminar experiments were 5 GPM and 2 GPM respectively. The axial shear rate for flow rates was around 0.5 1/s for the turbulent experiments and 1.82 1/s for the laminar experiments.

2.2 Membrane characterization

Pall Corporation supplied the porous membranes that are used in the experiments. The stainless steel porous cylinders that are used for the laminar and turbulent experiments involving the micron sized particles have pore diameters of 5 µm, 10 µm and 20 µm. To conduct experiments to investigate nanoparticle trajectory ratcheting, sheets of 100K Omega™ Ultrafiltration membranes that have pore diameters of approximately 10 nm are used. Characterization of these membranes was done using a bubble point test and atomic force microscopy measurements to ensure that the pores were the correct size. The characterization data can be found in Appendix A.

2.3 Particle Characterization

The particles used to characterize separation are polystyrene spheres with diameters of 0.5 µm and 5 µm and nanospheres organic hybrids sized 1.5 nm and 3.4 nm. The polystyrene spheres were synthesized and supplied by Pall Corporation and the nanoparticle organic hybrids were synthesized using a method developed by Krysmann et al[16]. The synthesis notes from Pall are found in Appendix B. The polystyrene particles were fairly monodispersed with a size distribution of 0.5 µm ± .067 µm and 5 µm ± 0.193 µm.

Scanning electron microscope (SEM) images of the polystyrene particles were taken to ensure that the particles were indeed the correct size and fairly monodisperse. Cryo-TEM and dynamic light scattering measurements were taken of the nanospheres to again ensure that the correct size was synthesized in a monodisperse batch. The size characterization data and images obtained by using these techniques can be found in Appendix A. Detailed information regarding the nanospheres synthesis and characterization can also be found in Appendix A and C.

2.4 Creating the feed stock solutions

The solution mix that is used for the experiments is a combination of the polystyrene spheres dispersed in water using an anionic surfactant, PEG-PPG-PEG. It was found that the optimal ratio between the particles and surfactant was that for every gram of particles used, 1.5 g of the surfactant was used. For every experiment, the volume fraction was ensured to be less than was around a value of 7E-04, which corresponded to 0.7g/L. These two materials are dispersed in water using an ultrasonic bath system. To minimize the density mismatch between polystyrene and water, approximately 20% by volume of glycerin is added to the solution. The amount of glycerin needed to reach this volume fraction along with the viscosity of the mixture was calculated

using a paper written by Cheng[26]. To make sure that the density matching was accurate, small vials were made with sample solutions of the polystyrene, surfactant, and water. Different amounts of glycerin were added and the volume ratio between water and glycerin was noted and the vials were set aside for a couple of days. If there was a density mismatch the particles either settled to the bottom or rose to the top of the vial.

It was found that using these materials combined in the solution allowed the polystyrene spheres to flow through the system without sticking to the stainless-steel membrane or any other part of the apparatus. The reasoning behind using the surfactant and other trials that were conducted with a different surfactant is detailed in Appendix A. To get the transmission ratio between the concentration of particles in the permeate versus the bulk solution, the absorbance of the solution was measured using a UV-Vis Spectrophotometer. The reason for using this method was mainly convenience, since there was a spectrophotometer in the same lab space that the equipment was housed in. This allowed samples to be taken and measured at any given time. The volume fraction of particles in solution needs to be less than 10^{-3} to minimize particle-particle interaction, which corresponds to a maximum concentration of 1000 parts per million (1 mg/ml) of particles in solution.

Chapter 3

Theoretical Predictions

3.1 Modeling the concentration profile and transmission rate for spheres in laminar and turbulent channel flows

The goal of sieve-free separation is to achieve a maximum possible concentration of particles in the retentate stream flowing within the channel, while drawing of nearly pure fluid through the membrane. Assuming a fully developed particle volume fraction profile in the channel, the particle volume fraction satisfies the convection-diffusion equation:

$$\frac{d}{dy}\left[v\phi - \mathrm{D}\frac{d\phi}{dy}\right] = 0, \qquad [1]$$

where y is the coordinate normal to the porous surface, and v and D are the particle's velocity and diffusivity in the y-direction. The velocity, v, is the sum two components, the lift velocity, v_L and the permeate velocity, v_p. If the suspension is dilute and the particle Reynolds number as calculated in Equation 2 is small, the lift velocity can be obtained from perturbation analyses and takes the form as shown in Equation 3.

$$Re_p = \frac{\gamma a^2}{\nu}. \qquad [2]$$

$$v_L = \left(\frac{du}{dy}\right)^2 \frac{a^3}{\nu} f_L\left(\frac{y}{a}, \frac{y}{(\nu/\gamma)^{\frac{1}{2}}}\right), \qquad [3]$$

u is the x-component of the average fluid velocity, a is the particle radius, γ is the wall shear rate and ν is the kinematic viscosity.

This expression is obtained using lift force calculations of Cherukat and McLaughlin [18] along with resistance functions [19,20]. We want the particle volume fraction to be small to minimize the particle-particle interaction in the fluid. There are two regions where the lift velocity is considered; the inner region, where $Re_p << 1$ and $y << (\nu/\gamma)^{\frac{1}{2}}$ and the outer region where $Re_p << 1$ and $y >> a$. $(\nu/\gamma)^{\frac{1}{2}}$ is the region that is viscous dominated. Beyond that, the outer region is where the inertial and viscous effects are comparable. Figure 3.1 shows curves of the uniformly valid approximations to the maximum lift velocity for any y position at different Re_p values in a composite form with both the inner and outer regions.

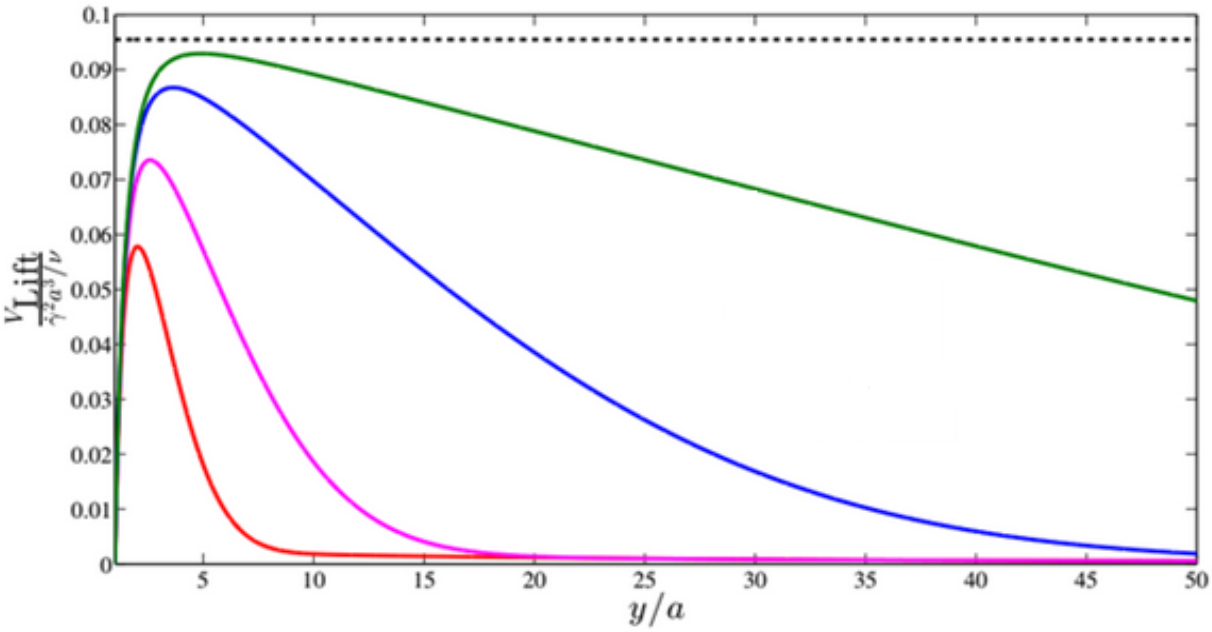

Figure 3.1: Composite expression for the lift velocity as a function of distance from the wall at different particle Reynolds numbers. (--- Maximum lift velocity obtained when $Re_p << 1$, the green line represents the max lift velocity at $Re_p = 0.001$, the blue line represents the max lift velocity at $Re_p = 0.01$ the purple line represents the max lift velocity at $Re_p = 0.1$, and the red line represents the max lift velocity $Re_p = 0.5$)

As can be seen from the graph, as the particle Reynolds number gets smaller, the value of the lift velocity becomes closer to the maximum attainable lift velocity for $Re_p << 1$. If the value of Re_p is 10^{-3} or lower, as shown by the green line, the inner region has a peak lift velocity very close to the dashed line. Thus, if the experimental conditions are such that the $Re_p < 0.001$ we can use the following equation to find the maximum lift velocity $v_{L,}$ over the range of y:

$$v_L = 0.1\frac{\gamma^2 a^3}{\nu}. \qquad [4]$$

While this condition can be satisfied for the 0.5 µm particles in turbulent flow, the justification for using Equation 4 to calculate lift doesn't hold true for the 5 µm particles in turbulent flows. This is because the Re_p range that can be experimentally obtained for these particles is 0.1 – 0.5. A Re_p of around this value will correspond to a curve near the red line shown in Figure 3.1. The peak for such a curve is about 2-3 times lower than the dashed line value, which means that the equation used for calculating lift for this case would be over calculating the lift velocity. For the 5 µm particles in laminar, the Re_p is in the range of 0.0008 to 0.005, which also satisfies the condition for using Equation 4 to calculate the lift velocity.

We must also consider whether the particle diffusivity has any contributions to the transmission of the particles. The particle diffusivity, D, has three contributions, Brownian diffusivity D_B, hydrodynamic diffusivity D_H, and a turbulent eddy diffusivity, D_E. The hydrodynamic diffusivity scales with the volume fraction. We have set the volume fraction to a low value to minimize the particle-particle interactions. We can also establish that the Brownian diffusivity is small, by using the Stokes-Einstein equation to calculate the diffusivity for both the particle sizes.

$$D_{B0} = \frac{k_B T}{6\pi\mu a}. \quad [5]$$

For the 0.5 μm particles, D_{B0} = 5.11E-13 m^2/s and for the 5 μm particles, D_{B0} = 5.11E-14 m^2/s. Another justification for neglecting the Brownian diffusivity is to compare it to the Peclet number based on the lift velocity and particle radius. If the value is large in comparison to the Brownian diffusivity, then it shows that the Brownian motion is not important compared with the convection by the lift velocity. The equation for calculating the Peclet number is shown below in Equation 6:

$$Pe_L = \frac{v_L a}{D_{B0}}. \quad [6]$$

Using this equation, we find that for turbulent experiments, with the range of lift velocities calculated for the 0.5 μm particles the Pe_L is around 0.25 – 10.02. For the 5 μm particles in the turbulent regime, the Pe_L is around 2.5E04 – 6.2E05. For laminar, the Pe_L is between 8 and 200. Most of these values are much larger than D_{B0} so we can neglect it. For the case of the 0.5 μm particles, the Pe_L at the lowest shear rate is not that high. However, another criterion for neglecting Brownian diffusion is if $D_{B0}/D_E << 1$ at the value of y = a. Using Equation 7 to calculate D_E, we can show that D_{B0}/D_E for the 0.5 μm particles is 0.0002, which is << 1. Therefore Brownian diffusion can be neglected even if Pe_L is not that high.

The only contribution left is the eddy diffusivity, which will only present itself in turbulent flows. An approximation for calculating D_E [24] has been derived to give the following correlation:

$$D_E = \frac{9x10^{-4}y^{+3}\nu}{(1 + 6.7x10^{-3}y^{+2})^{\frac{1}{2}}}, \quad [7]$$

where y^+ is the position, y, non-dimensionalized by the shear inertial length, $\delta_I = (\nu/\gamma)^{\frac{1}{2}}$.

To solve Equation 1 for laminar flows, D is small enough to be neglected and so only the $v\phi$ term remains. This allows ϕ to be a delta function at the point where v=0. We then have a criterion that there will be a point where v=0 in the channel when $v_p < v_{Lmax}$, and this means the particles will never come near the membrane and will be retained in the channel. If $v_p > v_{Lmax}$, then the particles will come to the membrane and be transmitted.

To solve Equation 1 for turbulent flows, there are two boundary conditions that need to be considered. The first boundary condition is that $\phi \rightarrow \phi_b \; as \; y \rightarrow \infty$, where ϕ_b is the bulk volume fraction. In turbulent flow, the turbulent eddy diffusivity dominates the particle dispersion, causing it to dominate the bulk flow and cause $\phi_b \neq 0$. In laminar flow, the bulk volume fraction is likely to be zero owing to the convective focusing of the particles. The second boundary condition is the flux boundary condition at the wall:

$$q = v_p\phi - D\frac{d\phi}{dy} = v_p\phi C \qquad \text{at } y = y_{min}, \qquad [8]$$

where q is the particle flux and $C\phi$ is the ratio of the particle volumetric flux to the fluid volumetric flux. y_{min} is the smallest value of y for which we solve the ODE. We assume that the particles that reach y_{min} will interact with the pore.

The base case for the theoretical predictions will assume that C = 1 and that y = a for Equation 8. By setting C = 1, we are saying that the membrane gives no resistance to the passage of particles. Setting y = a is saying that any particle that nearly touches the membrane will interact with the pore. As shown in the results section in Chapter 4, the trends obtained by using these theoretical predictions are like the experimental trends, but the fraction of particles transmitted (magnitude) are different.

To bring the theoretical predictions closer to the experimental values, the theory is modified following the assumptions and derivations made by Yan et al[14]. Yan developed the theoretical framework that would explain quantitatively how the concentration of particles entering a single pore in a planar wall is related to the local shear in the upstream boundary layer.[14] A three-dimensional theory was developed to describe the fluid capture tube upstream of the pore and then applied to a dilute suspension of rigid spheres to determine the particle entrapment. The theory in Yan et al[14] relates fluid flux through a pore, wall shear rate, and pore size to the particle flux. The dimensionless volume discharge rate through a pore according to Yan et al[14] is $2\pi Q$, which is non-dimensionalized by the wall shear rate (γ) and the pore radius (R_p). The flux through the pore can be written in terms of the permeate velocity and pore radius to relate the non-dimensional Q to factors that are experimentally set or known. Since Yan only focused on a single pore, we need to incorporate the porosity term, Φ, to account for the array of pores in the membrane We also need to assume that the pores act as if there is no interference.

$$\frac{v_p \pi R_p^2}{\Phi} = 2\pi Q \gamma R_p^3 \Rightarrow Q = \frac{v_p}{2\gamma \Phi R_p}. \quad [9]$$

To relate the particle flux to the transmission ratio, C, Yan derived an expression relating Q to the transmission ratio. He presented closed form results for both large and small Q limits from asymptotic analytical solutions. In the case of our predictions, we assume that Q is small (approx. 1), which corresponds to small suction through the pores. For small Q, the simplest estimate of the transmission ratio of particles can be obtained from Yan et al [14] analysis of non-Brownian spheres interacting with an isolated pore in a planar boundary to a shear flow:

$$C = \begin{cases} \left(1 - \frac{\bar{a}^2}{3\pi Q}\right)^{\frac{3}{2}} & if \quad Q > \frac{\bar{a}^2}{3\pi} \\ 0 & if \quad 0 \leq Q \leq \frac{\bar{a}^2}{3\pi} \end{cases}, \qquad [10]$$

where C is the local transmission through the pore based on the local volume fraction next to the membrane . In these equations, $\bar{a}$ is the particle radius that has been non-dimensionalized by the pore radius, $R_{p:}$

$$\bar{a} = \frac{a}{R_p}. \qquad [11]$$

Therefore, solving for Equation 1 using the conditions expressed in Equations 4-6 allow for calculating the transmission ratio of particles at different shear rate, permeate velocity, particle radius, and pore radius. However, it should be noted that the theory presented in Yan et al is for a single pore in a planar wall. It leaves out interference between neighboring pores and any roughness of the membrane. Thus, we should not expect it to be quantitatively accurate, though it can give an indication of how the boundary condition changes with the shear rate, pore radius and permeate velocity. In addition to that, it can show if the experimental trends obtained with changing parameters like the shear rate or permeate velocity match with the theoretical predictions obtained by using this analysis. Looking further at the details of Yan analysis, the concentration of particles develops far away from the pore along the wall which makes the presence of neighboring pores and its effects even more significant.

To account for these differences, there are scaling that are eventually used from Yan, that are presented in the results section. One such scaling is to present y_{min} as a function of the shear

rate, permeate velocity, and pore radius rather than the particle radius. This relation was obtained from Yan's analysis for small Q. What this relation allows for is a change in the boundary layer length to account for how far above the wall a particle upstream can be and still flow into the pore. This means that rather than just if the boundary layer is fixed at y = a, the particles are also found between y = a and y = a+z, where z is the height of the mixed boundary region. The value for z considers the pore radius, permeate velocity, and shear rate and introduces a fitting parameter k, which has units of length and can be adjusted accordingly for each set of experiments. This adjustment is more important at larger pore radii, where the region of suspension that gets sucked in the pore is larger:

$$z = k\sqrt{\frac{R_P v_p}{\gamma}}. \qquad [12]$$

The other scaling factor is a form of Equation 10, but omits the 3π, pore radius, and porosity and includes a dimensional fitting parameter to allow for modifications to be made to fit the theoretical data to the experiments. Another fitting parameter, k_1, is introduced which is incorporated to consider the aspect of neighboring pores and roughness of the membrane. The initial assumption only considered the particle flux through a single pore. The equation for C is included below, which is basically a scaling of the original C in Equations 8 and 10. The equation contains a fitting parameter k_1, which can be adjusted accordingly based on the type of experiments. In this case k_1 has units of length. This effect is important for small pores where there is more of a tendency of the pore to block the entrance of some particles:

$$C = \left(1 - \frac{k_1 \gamma}{v_p}\right)^{\frac{3}{2}}. \qquad [13]$$

Therefore, Equation 8 is modified as shown below to account for the two assumptions made with the two fitting parameters.

$$q = v_p \phi C \qquad \text{at y = a + z,} \qquad [14]$$

To reiterate, for the base case theoretical predictions, the assumption is that C = 1 and y = a. Using the adjusted conditions of C not being equal to 1 and z being non-zero, the transmission values obtained theoretically in the base case is adjusted using Equation 14 to try to better fit the theoretical predictions to the experimental results.

Experimentally, the particle flux equation is defined as $q = v_p \phi_b C_b$, where C_b is the overall transmission ratio based on the bulk volume fraction and accounting for the transport processes in the channel.

3.2 Experimental calculations

Values such as the shear rate and permeate velocity need to be calculated using the parameters that can be experimentally manipulated such as the spin rate and fluid fluxes. To calculate the shear rate, the angular velocity generated by the spinning of the outer cylinder is used. The angular velocity ω, is calculated from the spin rate of the spinning cylinder that can be read from the digital readout on the controller by using the following equation:

$$\omega = \frac{2\pi(RPM)}{60}, \qquad [15]$$

where the spin rate units are in rotations per minute (RPM).

The equation for estimating the shear rate from the calculated angular velocity depends on the fluid regime. For laminar flow in a Couette cell, the maximum shear rate is at the surface of the inner cylinder and is derived in Batchelor[12] as:

$$\gamma = 2\omega \left(\frac{r_2^2}{(r_2^2 - r_1^2)} \right), \quad [16]$$

where ω is the angular velocity which is calculated from Equation 15, r_2 is the radius of the outer cylinder and r_1 is the radius of the inner cylinder.

For turbulent flow, the shear estimate is derived from Schlichting[13] and the Blasius relation for shear stress at the wall to get the following:

$$\gamma = \frac{0.3164(r_2^2 \omega^2)}{32\nu Re^{\frac{1}{4}}}, \quad [17]$$

where Re is the Reynolds number for the Couette Flow. The appropriate Reynolds number for this type of geometry can be calculated using:

$$Re = \frac{\omega r_2 (r_2 - r_1)}{2\nu}. \quad [18]$$

The permeate flux can be controlled by the cross-flow apparatus and output in the units of ml/min. To convert the flux into cross-stream velocity, the surface area, A, of the porous structure is used along with the volumetric flux, q':

$$v_p = \frac{q'}{A}. \quad [19]$$

For laminar flow, the gap between the porous cylinder and the spinning outer cylinder needs to be around 1 mm. This allows for reasonable spin rates to be set to achieve shear rates in the laminar regime. The range of Re and subsequently the shear rates deemed acceptable for the laminar range was estimated based on a paper by Ravelet et al[21], which had a system with the same geometry as the experimental set-up, but with different cylinder radii. With the gap thickness they had (10 mm with r_o =120mm and r_i=110 mm), they found that the laminar regime could be achieved at high Re upto 4000. The gap thickness that was used for the laminar experiments was 1 mm (r_o =54 mm and r_i=53 mm). From this information, an estimate was made to the range of Reynolds number that would ensure that the experiments were run in a laminar regime. To stay on the safe range of Re set was 160 – 410, which corresponded to a shear rate range of 570 1/s – 1400 1/s. For turbulent flow, the gap thickness was like that of the paper of 10 mm (r_o =54 mm and r_i=44 mm). There the ranges of Re and shear rates that were run were 38,000 – 68,000 and 69,000 1/s – 187,000 1/s respectively.

3.3 Sieve-free separation due to particle trajectory ratcheting using nanospheres

Lift based separation can occur for particles with diameters larger than about 200 nm. However, Hurwtiz and Brantley[10] showed sieve-free separation for globular proteins such as bovine serum albuminum (BSA) and cytochrome C. The particle radii for these proteins were 3.4 nm and 1.8 nm respectively. Using a 36-nm pore diameter membrane, they showed transmission ratios as low as 0.1 at shear rates around 10^5 1/s could be obtained. They had initially attributed the separation to inertial lift, but the lift velocity calculated from Equation 4, for a shear rate of 3.6 x 10^5, the BSA had a lift velocity of no more than 0.8 nm/s, which was significantly lower than the permeate velocity which ranges from 2.8 µm/s to 140 µm/s.

The flux of the particles through the membrane, evaluated as for the micron sized particles is:

$$q = v_p \phi Q, \qquad [20]$$

where Q is again the dimensionless fluid flux through the pore that we can estimate in the simplest case from Yan et al. Assuming that Q is small, we can use Equation 10 to estimate the transmission ratio:

$$Q = \left(1 - \frac{2\gamma a^2}{3\pi\Phi v_p R_p}\right)^{\frac{3}{2}} H\left(1 - \frac{2\gamma a^2}{3\pi\Phi v_p R_p}\right), \qquad [21]$$

where the dimensional form of Q = $\frac{v_p R_p}{2\gamma}$ and H(x) represents the Heaviside step function. The comparison of the theoretical predictions and experimental results obtained by Hurwitz and Brantley is shown in Figure 3.2.

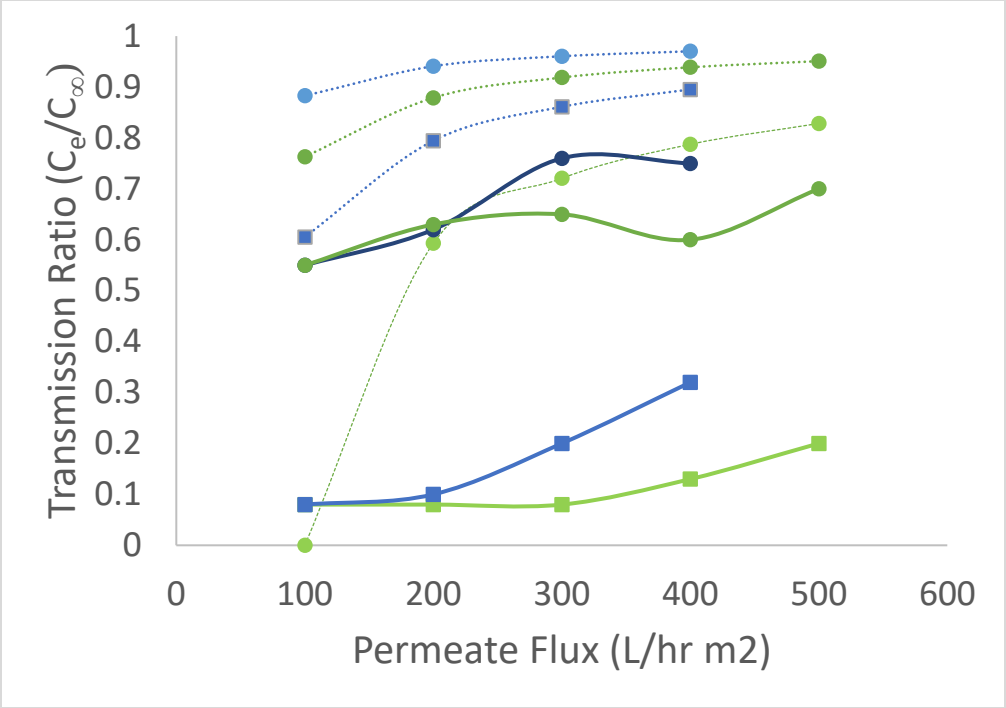

Figure 3.2: Fraction of proteins transmitted to the filtration stream in sieve-free separation of BSA a=3.4nm (squares) from Cytochrome C a=1.8 nm (circles) at $\gamma = 5.8 \times 10^4\ s^{-1}$ (blue) and $\gamma = 1.2 \times 10^5\ s^{-1}$ (green). Solid lines are experimental measurements [10] and dashed lines are predictions for skimming of non-Brownian particles by isolated pores [24]

We expect to see similar trends with the nanospheres, especially since using spherical particles will allow us to visualize the results for a more ideal case rather than using irregularly shaped proteins. The gap thickness for these sets of experiments differ from the turbulent experiments with the micron sized particles. The gap thickness is 2.5 mm (r_o =54 mm and r_i= 51.5 mm) which correspond to a Re range of 17,000 – 27,000 and a shear rate range of 100,000 1/s – 150,000 1/s.

In sieve-free separation, an additional criterion for the separation to work is that the Peclet number for the particle should be large enough. This value can be calculated for the proteins and the nanoparticles using the following Equation.

$$Pe_p = \frac{\gamma R_p^2}{D_{B0}}. \qquad [22]$$

For BSA, the range of Pe_p is between 0.12 to 0.24 respectively. For Cytochrome C, the range of Pe_p is between 0.26 to 0.54. For the two sets of nanospheres (1.5 nm and 3 nm), the Pe_p ranges are 0.06 to 0.12 and 0.12 – 0.24 respectively. All these values are smaller than 1, which means that the particles diffuse into the pores as they pass by it. This is evident in the results when we show that high transmission of particles is achieve for the particle radius and pore size used. Further experiments need to be conducted in the future where the particle radius and pore radius are increased to bring the Pe_p up.

Chapter 4

Results and Discussion

To validate the experimental results, theoretical predictions have been developed by a former post-doc student, Dr. Anubhab Roy, for both lift and trajectory-ratcheting separation in an idealized Couette cross-flow filtration geometry. There are six sets of experiments that will be evaluated using particles of sizes 0.5 µm, 5 µm, 1.5 nm, and 3.4 nm in diameter and membranes with pore diameters of 10 nm, 5 µm, 10 µm, 20 µm, and 50 µm. Predictions will first be shown using the baseline assumptions of C = 1 and y = a, followed by the results made with the modifications derived from Yan et al. to match the predicted transmission ratios closer to the experimental results obtained.

Table 4.1 presents a short summary of the subsections that will be discussed in the results section. The second column indicates the different physics involved in matching the theoretical predictions with the experimental results and how either changing the particle radius or pore radius accounts for using different physics for each case. The transport in the channel for all the different cases remains the same.

Table 2: Summary of subsections

Laminar experiments of 5 μm spheres using 50 μm membrane	Separation occurs due to convection by lift and permeate flow balance
Separation of 0.5 μm spheres in turbulent channel flows using a 5 μm porous membrane	Need to consider the skimming of the fluid and rejection of particles by the excluded volume of the pore (Eq. 13). The lift velocity, permeate velocity, and turbulent dispersion are the competing transport processes that determine the magnitude of transmission.
Separation of 0.5 μm spheres in turbulent channel flows using a 10 μm and 20 μm porous membrane	Don't need to consider the skimming of the fluid, but rather the capture layer thickness (Eq. 12). The lift velocity, permeate velocity, and turbulent dispersion are the competing transport processes in the channel that determine the magnitude of transmission
Separation of 5 μm spheres in turbulent channel flows using a 20 μm porous membrane	Re_p is finite, so we need to consider its effect on the maximum lift velocity. Also need to consider the fact that the turbulent diffusivity scales with the shear rate more than with the maximum lift velocity to account for the increase in transmission ratio. Finally, the capture layer thickness is considered (Eq. 12). The competing transport processes in the channel that determine the transmission in this case are the lift velocity and turbulent dispersion.

The simplest case that can be theoretically analyzed is when the channel flow is laminar and separation is observed for the larger spherical particles. For experiments conducted in the laminar regime for the larger particles (5 μm spheres), the simplest assumption of the conditions yielding lift-based separation is obtained by neglecting particle dispersion and only having the convective terms of the lift and permeate velocity. The predominant dispersion mechanism is the

convective balance between the permeate and lift velocities This means that in the ideal case, below a critical shear rate, the transmission of particles reaches 1, and above the critical shear rate the transmission shifts to 0.

Since only the permeate and lift velocity contribute to the transmission, the critical shear rate, γ_c, can be calculated by equating the permeate velocity, $v_{p,}$ to the lift velocity, $v_{L,}$ calculated in Equation 4 This gives:

$$\gamma_c = \sqrt{\frac{10\nu v_p}{a^3}}. \qquad [23]$$

For typical channel thicknesses of order millimeters, the volumetric flow rate in the channel needed to generate v_L=v_P will result in turbulent flow for particle radii smaller than about 1 μm and laminar flow for larger particles. The fluid is a mixture of glycerin and water set so that the fluid density is equal to the particle density. This means that the fluid mixture density and viscosity are 1.05 g/cm^3 and 0.0016255 Pa s respectively. Additionally, the Re_p for these experiments is in the range of 0.0008 - 0.005, which is small enough for the simple lift assumption to be valid. Figure 4.1 shows the predicted and experimental results for the 5 μm particles at two different permeate velocities and a range of shear rates.

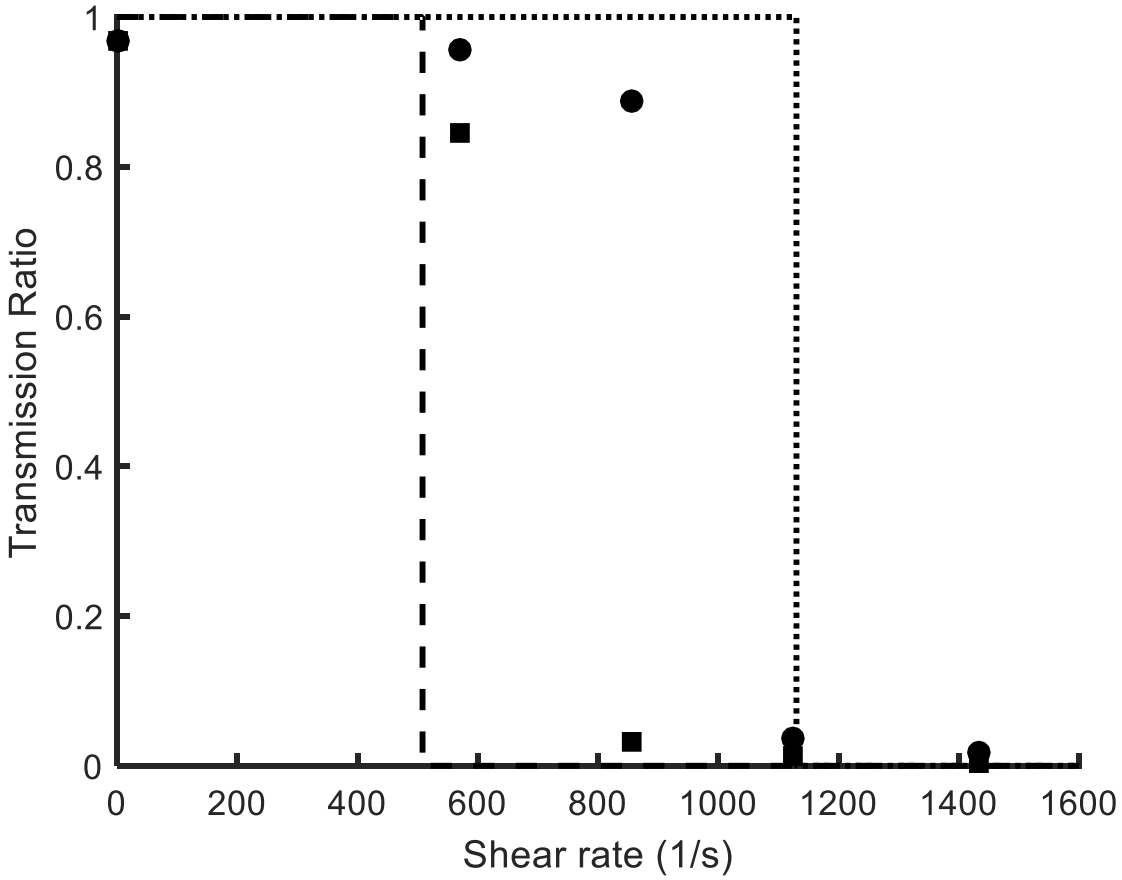

Figure 4.1: Transmission ratio as a function of shear rate for two different permeate velocities when the particle size is 5 μm**.** The closed squares and circles (experimental) and long and short dashed lines (predicted) represent the results obtained when the permeate velocities are 0.23 μm/s and 1.16 μm/s respectively.

As shown in the figure, the dashed lines represent the idealized predicted case, which is a step function showing the transition of the transmission rate from 0 to 1 at a critical shear rate. For these two permeate velocities of 0.23 μm/s and 1.16 μm/s, the critical shear rates fall in the range of 600 1/s to 850 1/s and 900 1/s to 1150 1/s respectively. The experiment follows a similar trend to the theoretical predictions and that below a critical shear rate, there is complete transmission and above the critical value, there is little to no transmission.

Since the case of separation due to convective balances of lift and permeate velocities have been shown to match the theoretical prediction for the 5 μm particles, the next step is to observe the effect of running 0.5 μm particles with a membrane whose pore size is 10 times larger. 0.5 μm polystyrene spheres were used to conduct turbulent experiments using a 5 μm porous membrane. The purpose of this was to observe the effects of hydrodynamic lift and turbulent diffusivity on particles smaller than 1 μm using a membrane that had pores 10 times larger than the particle diameter. Experiments were conducted at four different permeate velocities over a range of shear rates to observe the transmission of particles through the membrane as a function of shear rate. Figure 4.2 shows the experimental results of transmission over a range of shear rates at the 4 different permeate velocities along with the theoretical predictions obtained for the same set of conditions with the base case assumptions.

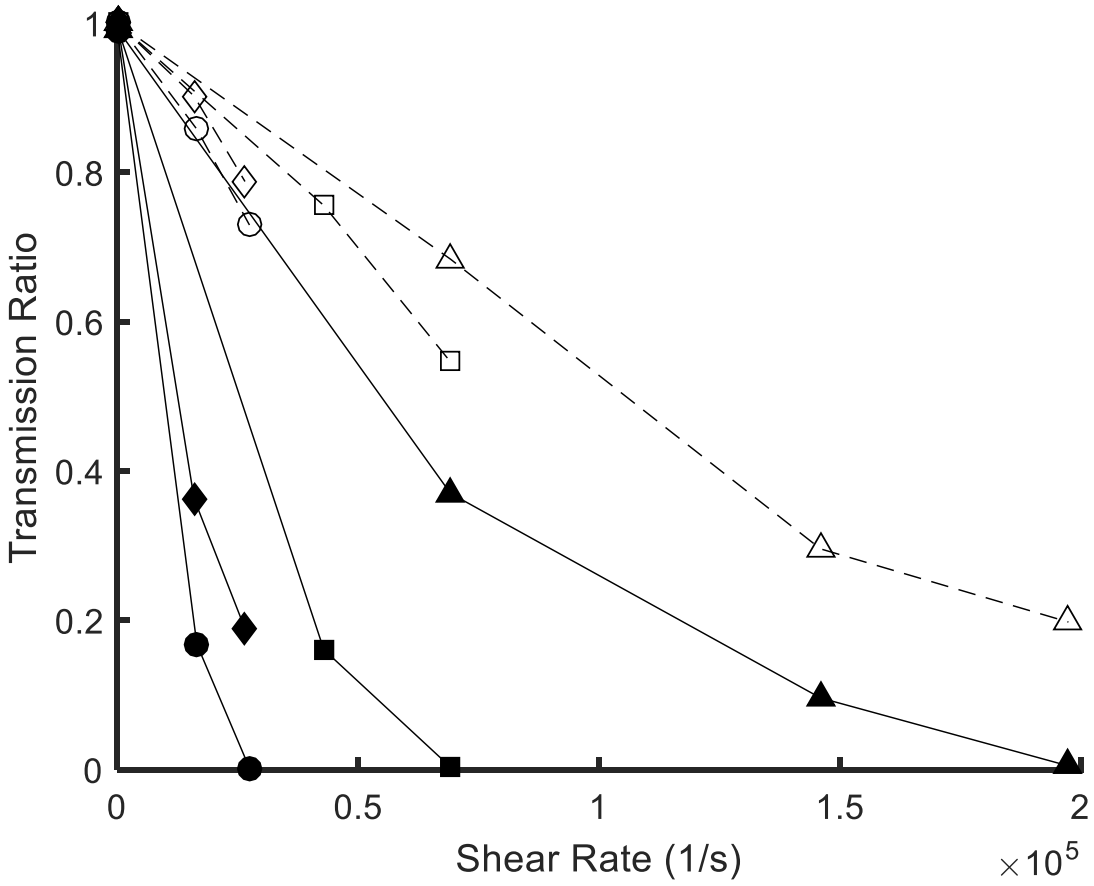

Figure 4.2: Transmission ratio as a function of shear rate at four different permeate velocities for the 0.5 μm particles with a 5 μm porous membrane using the base case. Closed symbols indicate experimental results and open symbols indicate theoretical predictions. (▲ – 10.68 μm/s, ■ – 5.19 μm/s, ♦ - 1.83 μm/s, ● – 0.93 μm/s)

The graph shows two important trends. One is that at all permeate velocities, the trend is that as the shear rate increases, the transmission ratio decreases. The second trend observed is that as the permeate velocity decreases, the transmission decreases at the same shear rate. It can also be observed that for different permeate velocities, the shear required for almost zero transmission decreases as the permeate velocity decreases. This is significant because lower shear rates mean

less power consumption by the equipment to separate the particles. However, the tradeoff is that the overall process will take long for lower permeate velocities.

Theoretically, the predictions show the transmission ratio decreasing as the shear rate increases. However, the experimental results have a much sharper decrease in transmission ratio as compared to the theoretical predictions. Additionally, the magnitude between the two sets of results are off by a magnitude of around 3 for the higher permeate velocities and by a factor of 8 for the lower permeate velocities.

Adjustments were made to the particle flux boundary condition using Equation 23. In the case of these set of experiments, it was found that keeping the value of $z = 0$ and having a value of $k_1 = 53.59$ µm provided the best fit for the theoretical predictions and experimental results. This was because as mentioned previously in the theory section, adjusting the k_1 parameter is more important for smaller pores since there is more of a tendency of the pore to block the entrance of some particles. It was also found that calculating z for this pore size gave a value close to zero, so there was little effect. Figure 4.3 shows the comparison of the two sets of data at the four different permeate velocities, using the adjusted boundary condition equation. The value for k_1 is the same for all the different permeate velocities and z is set to zero for all the data sets. The prediction of measurements is compared in Figure 4.3

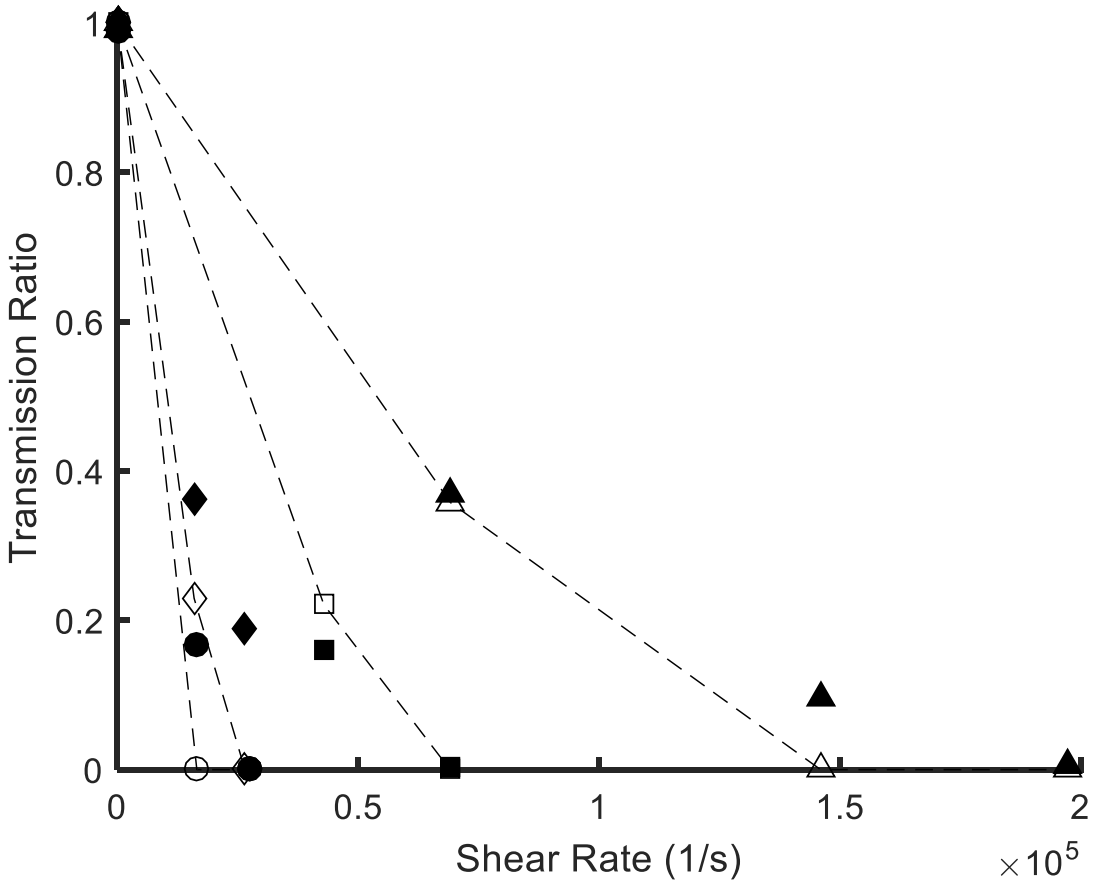

Figure 4.3 Transmission ratio as a function of shear rate at four different permeate velocities for the 0.5 μm particles with a 5 μm porous membrane using the adjusted boundary condition. Closed symbols indicate experimental results and open symbols with the dashed line indicate theoretical predictions with z = 0 and k_1 = 53.59 μm. (▲ – 10.68 μm/s, ■ – 5.19 μm/s, ♦ - 1.83 μm/s, ● – 0.93 μm/s)

By using the modified particle flux equation with C, the theoretically predicted values for the transmission ratio match much closer to the experimental values than by using the base case. Not only are the trends similar in both cases, but the data points also overlay each other, indicating transmission ratio values of the same magnitude at a set shear rate and permeate velocity. This

confirms the trends in Yan's predictions in Equation 13 for how C varies with shear rate and permeate velocity.

Since the fluid being used for the experiments is a mixture of water and glycerin, we briefly want to observe the effect of changing the viscosity on the transmission of the particles. While this is not as important of a factor to observe unlike the effect of shear rate and permeate velocity, observing the effect of viscosity helps validate the dependence of lift velocity and turbulent dispersion on viscosity. This allows the theoretical model to capture any additional aspects of the experimental conditions.

Since polystyrene is denser than water, the fluid density needs to be matched with glycerol to eliminate the effects of centrifugal forces acting on the particles and contributing to the transmission. Experiments were done where the fluid density deviated from the matched case at a fixed permeate velocity and a range of shear rates to observe the transmission. By changing the density of the fluid, the fluid viscosity was also changed, which was an important factor to observe to see if a change in viscosity affected the transmission in any way. The density was varied from 1.04 kg/m^3 to 1.06 kg/m^3, which corresponds to a change in fluid viscosity from 0.0014 Pa s to 0.0018 Pa s.

Figure 4.4 shows the experimental effects of slight variations in the fluid viscosity on the transmission ratio of the 0.5 μm particles through a 5 μm membrane when the permeate velocity is fixed at 10.68 μm/s. The equations used to calculate the predicted trends follow baseline assumptions made to the particle flux boundary condition for solving Equation 1. This means that $C = 1$ and $y = a$.

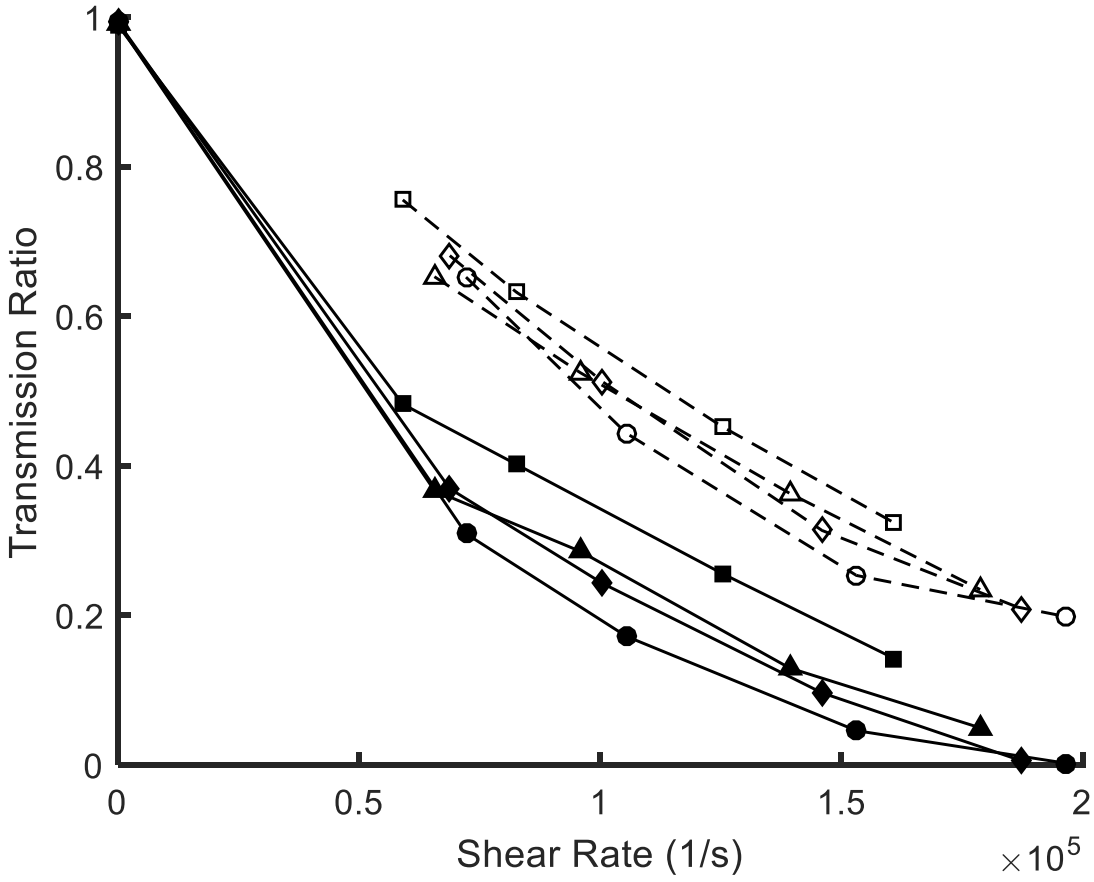

Figure 4.4: Experimental and predicted results for transmission for 0.5 µm particles using a 5 µm membrane and a permeate velocity of 10.68 µm/s. Closed symbols indicate experimental results and open symbols indicate theoretical predictions. (●- 1.44E-03 Pa s, ♦ – 1.51E-03 Pa s, ▲ – 1.62E-03 Pa s, ■ – 1.85E-03 Pa s)

As can be observed from the figure, the trends of both the theoretical predictions and experimental results are the same for the different conditions. However, the curves for the theoretical predictions are shifted towards higher transmission than the experimental results at the same shear rate.

To bring the data together to match in magnitude as well as trends, the modifications that were made to the particle flux boundary condition based on Yan's analysis need to be taken into

consideration. As mentioned in the previous section, Yan's predictions only considered the effects of inertial lift on a single pore and only to a distance of one particle radius away from the porous surface.

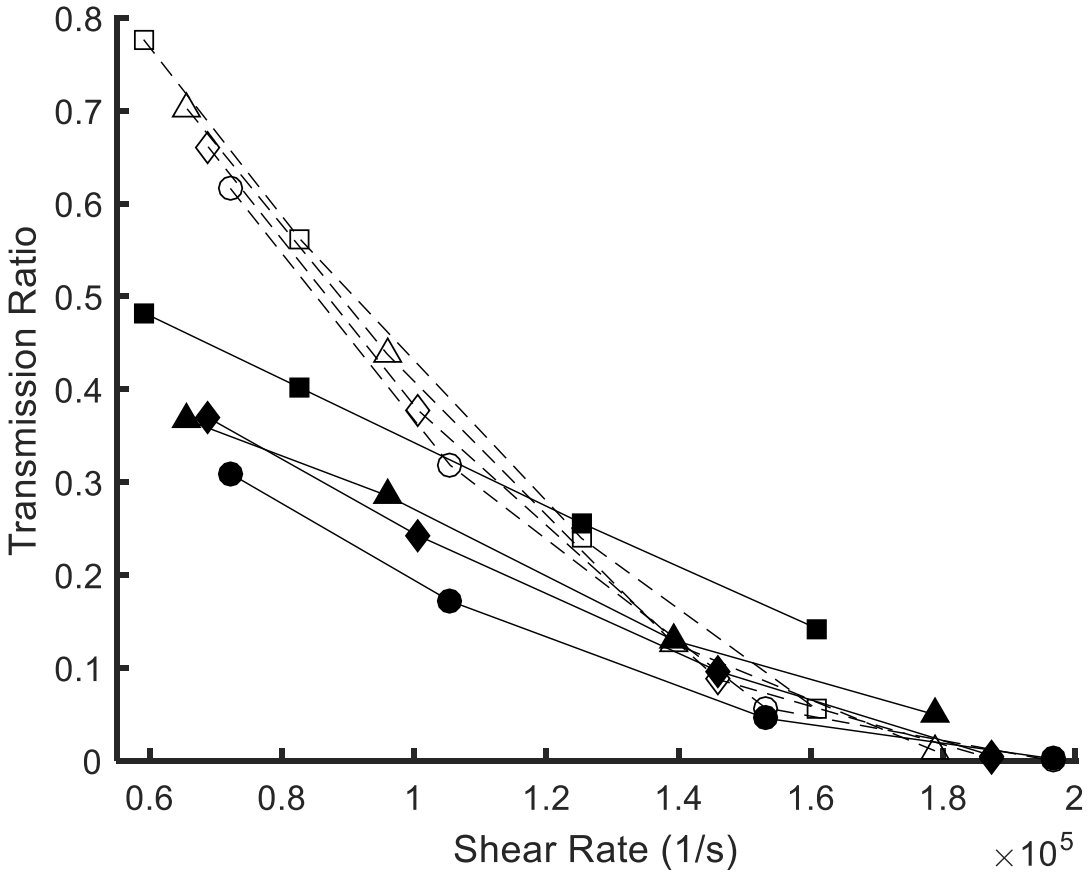

Figure 4.5: Experimental and predicted results for transmission for 0.5 µm particles using a 5 µm membrane and a permeate velocity of 10.68 µm/s. Closed symbols with the lines indicate experimental results and the open symbols with the dashed lines indicate the theoretical predictions of the effect of viscosity on transmission. (●- 1.44E-03 Pa s, ♦ – 1.51E-03 Pa s, ▲ – 1.62E-03 Pa s, ■ – 1.85E-03 Pa s)

Figure 4.5 shows the theoretical predictions of the transmission ratio when the fluid viscosity is changed. The effect of centrifugal velocity was also considered, but it was shown that

it played little to no effect on the transmission and any change in the transmission is purely due to viscous effects as shown by the dashed lines. For example, at a shear rate of 10^5 and a viscosity of 1.62E-03 Pa s, the transmission ratio because of both centrifugal velocity and viscous effects was 0.4413 as compared to a transmission ratio of 0.4382, where only the viscous effects were considered. Additionally, as was shown in the experiments, changing the viscosity (by changing the fluid density) makes only slight changes to the transmission ratio, which just confirms that being approximately close to the matched fluid density case is enough when running the experiments. The theoretical data more closely matches the experimental data in this case, especially when the shear rates are higher. Overall, compared to the base case, the magnitude between the theory and experiments match better and the trend of decreasing transmission with increasing shear rate holds true in both cases.

Now that it has been shown that separation occurs with the 0.5 μm particles using a 5 μm pore sized membrane and that effects such as centrifugal velocity or fluid viscosity doesn't affect the theoretical predictions, other factors such as changing the pore radius can be tested to observe any changes in transmission ratio.

To examine the effects of pore size on separation, turbulent experiments were run with the 0.5 μm particles using both 10 μm and 20 μm pore diameter membranes. All the other experimental conditions remained the same and the effect of transmission as a function of shear rate was observed at a fixed permeate velocity of 5.19 μm/s. Using the same base case assumption of C = 1 and y=a, theoretical predictions were made for these conditions for both sets of experiments. Figure 4.6 shows the theoretical predictions compared with the experimental results of the transmission ratio for both the membranes.

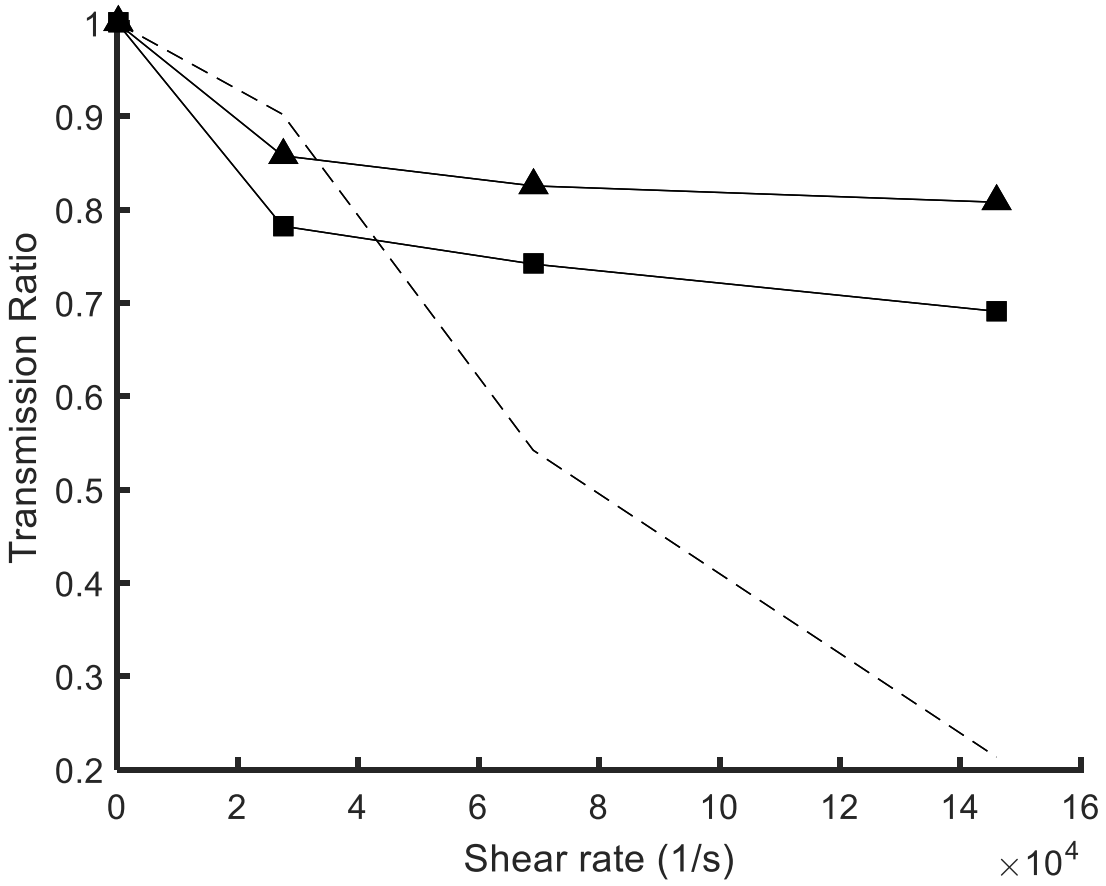

Figure 4.6: Transmission ratio as a function of shear rate for the 0.5 µm particles through both a 10 µm and 20 µm membrane at a fixed permeate velocity of 5.19 µm/s. The dashed represents the theoretical predictions for the base case for both the membranes. The closed symbols with the solid lines represent the experimental results for both membranes (▲ – 20 µm membrane, ■ – 10 µm membrane)

What is observed with these experiments is that there isn't as sharp of a decrease in transmission ratio of particles when the shear rates increase, not only when compared to the theoretical predictions, but also to the results obtained from using a 5 µm pore membrane. To account for the large difference between the predicted values and experimental results, the mixed boundary layer thickness, z, was adjusted to try to minimize the discrepancy. The value of z is

adjusted for all the experimental conditions, keeping the k value consistent across the data points for both the 10 µm and 20 µm membrane. It was found that having k = 75.31 µm gave the best fit for all the data points. C remained as 1 since as mentioned in the theory chapter, more of a difference is made by changing z for larger pore sizes to account for the change in the region of suspension that gets sucked into the pore. It was also found that computing C for both the membrane sizes gave a value close to 1, so it had little effect. Figure 4.7 shows the adjusted transmission ratios using Equation 23, where C = 1 and k = 75.31 µm.

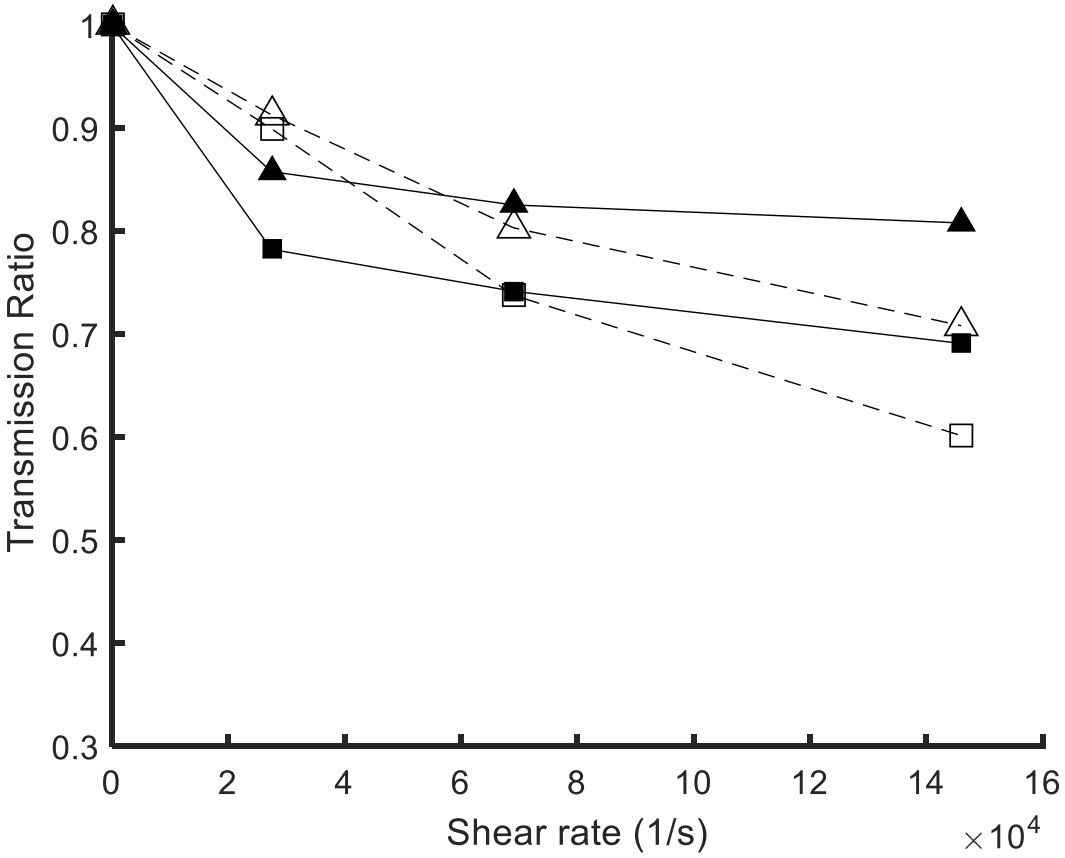

Figure 4.7: Transmission ratio as a function of shear rate for 0.5 µm particles using a 10 µm and 20 µm membrane. Closed symbols indicate experimental results and the open symbols indicate theoretical predictions where C = 1 and k = 75.31 µm. (▲ – 20 µm membrane, ■ – 10 µm membrane)

Using the fitting parameter value and modified boundary condition, the theoretical predictions fit the experimental results much better than in the base case. Compared to the base case, the adjusted case follows the same trend as the experimental results for both the membranes. While the theoretical predictions are still off by a factor of around 1.25, the fit is a lot better than the base case. Both the experimental results and predictions also show that as the pore radius increases, the slope of both the lines is less sharp. The difference is more pronounced in the predicted case than in the experimental results, where the decrease in transmission ratio as the shear rate increases is not as drastic.

However, the difference in transmission ratio is more pronounced when the shear rate is set and the permeate velocity is changed to observe the change in transmission. It was observed in the case with the 0.5 μm particles and the 5 μm membrane that as the permeate velocity decreased, the transmission ratio decreased when observed at a set shear rate. Figure 4.8 shows a plot of the transmission ratio as a function of changing permeate velocity for the 0.5 μm particles and the 20 μm membrane. The theoretical predictions are by using the adjusted boundary condition and fitting parameter of k =75.31 μm.

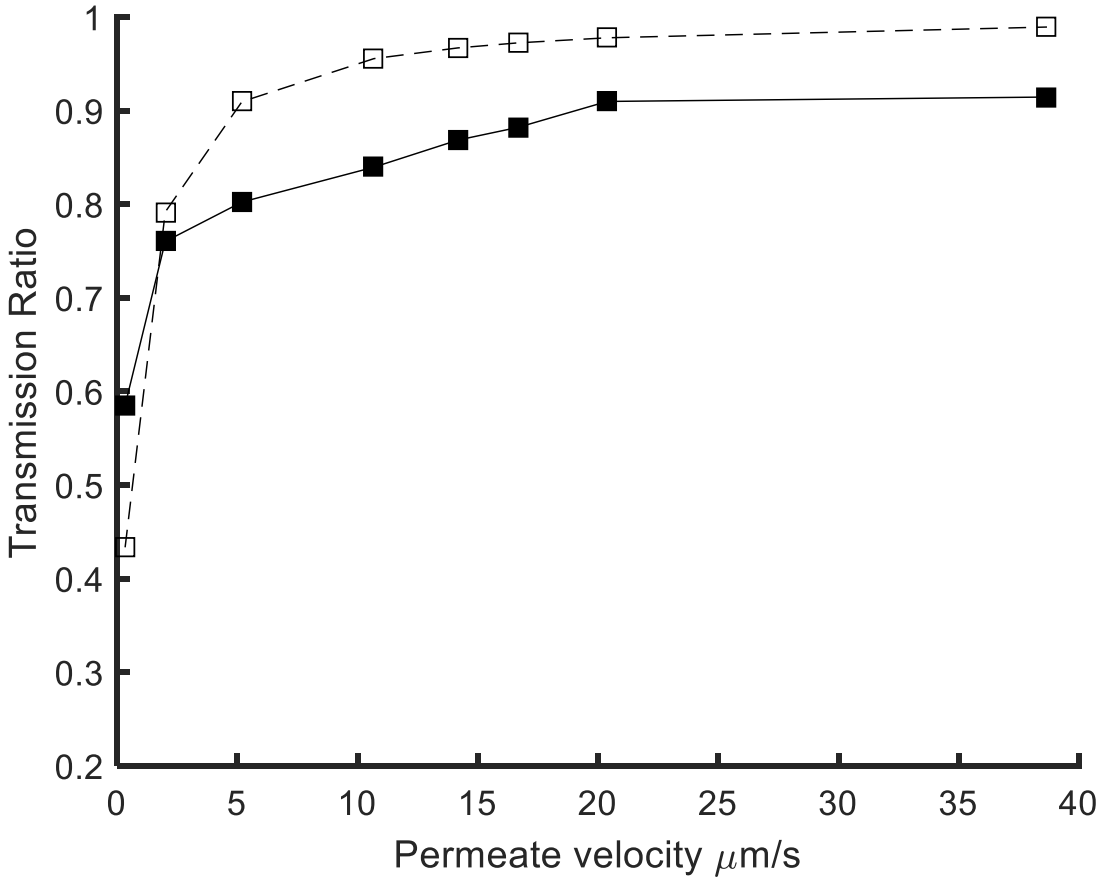

Figure 4.8: Transmission ratio as a function of permeate velocity for the 0.5 μm particles using a 20 μm membrane. The shear rate is fixed at a constant value of 73,087 1/s. The closed symbols and solid line indicates experimental results and the open symbols with the dashed line indicates theoretical predictions.

The final set of experiments that were done with the micron size polystyrene spheres was to investigate the effects of separation in turbulent flows using 5 μm particles and a 20 μm membrane at a permeate rate of 10.74 μm/s. Figure 4.9 shows a plot of the transmission ratio as a function of shear rate both experimentally and theoretically.

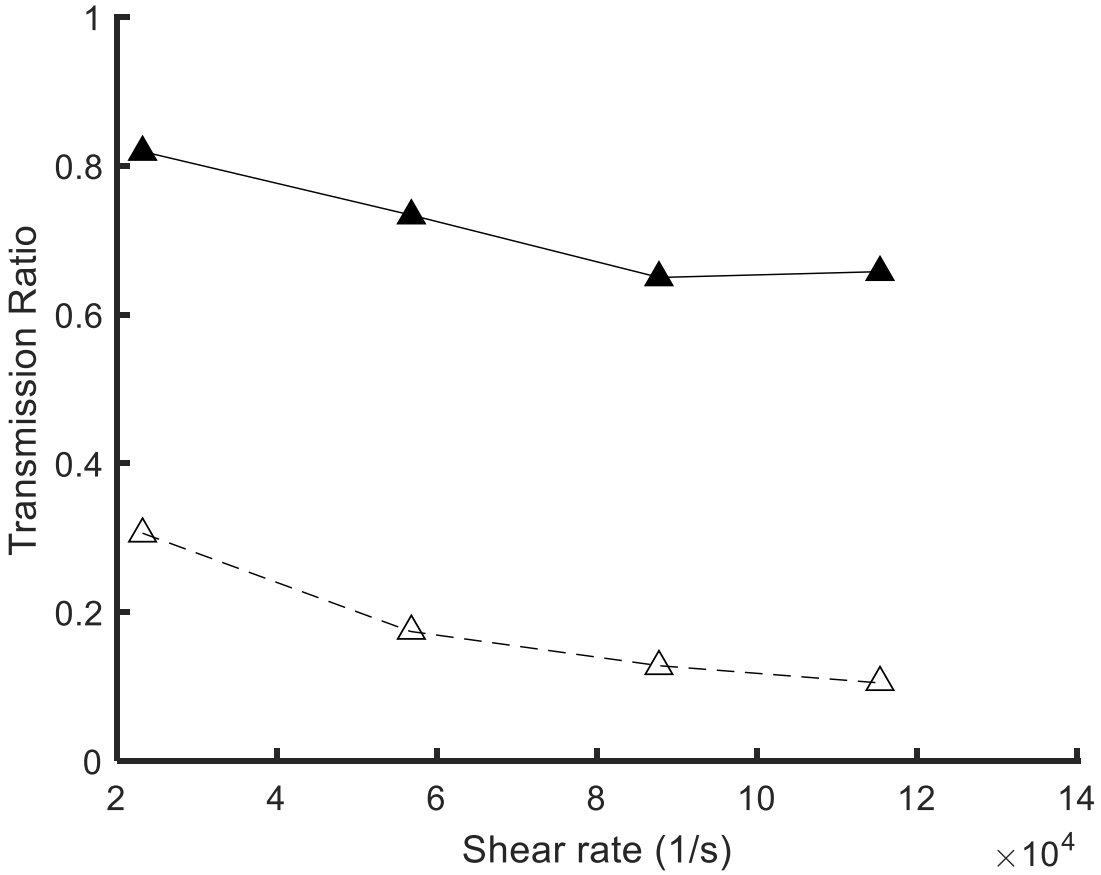

Figure 4.9: Plot of the transmission ratio as a function of shear rate for the 5 μm spheres through the 20 μm membrane. The closed triangles represent the experimental results and the open triangles represent the theoretical results.

Using the base case assumptions that were used for the 0.5 μm particles yielded transmission ratio values that were very close to zero. For example, at the lowest shear rate of 23,197, the transmission ratio calculated was 1.3E-06. The calculated values were many magnitudes off from the experimental results, so an intermediate step was taken to try to bring up the values to match the experimental results. The modified theoretical results were calculated by decreasing the maximum lift velocity by a factor of 3 and increasing the turbulent diffusivity by a factor of 2. The maximum lift velocity was decreased because the finite Re_p makes it so that the

low Re_p estimate we were initially using was not reliable. By increasing the turbulent diffusivity, this corresponded to averaging the D_E over the volume of a particle rather than using the point tracer results. Using these assumptions results in transmission ratios that are lower than the experimental results achieved, but both sets of data show the same trend. In the case of these particles another thing that can be noted in the results is the transmission ratio seems to start increasing slightly as the shear rate increases. The reason for this increase is that D_E increases with the shear rate faster than the lift velocity. The increase in turbulent dispersion can potentially compete with the lift, causing the transmission to increase with increasing shear rate. This increase doesn't matter as much with lift velocity. One way to observe this would have been to keep increasing the shear rates to see if the transmission kept increasing more rapidly, however it was not done in this case. Shown below is the scaling of D_E and v_L with the shear rate to show the effect of increasing shear on the turbulent diffusivity. These were obtained by looking at Equations 4 and 7.

$$D_E \propto \gamma^3$$
$$v_L \propto \gamma^2 \qquad [24]$$

Additionally, calculating the theoretical lift velocity shows that it is around 10^4 μm/s, which is significantly higher than the permeate velocity of 10.74 μm/s that was set for the experiments. This can also mean that the permeate velocity has a small effect on the transmission ratio over the range of shear rates. We can show that the permeate velocity doesn't influence the transmission ratio by observing its change at a set shear rate of 87,763 1/s and varied permeate velocities. Figure 4.10 shows the results.

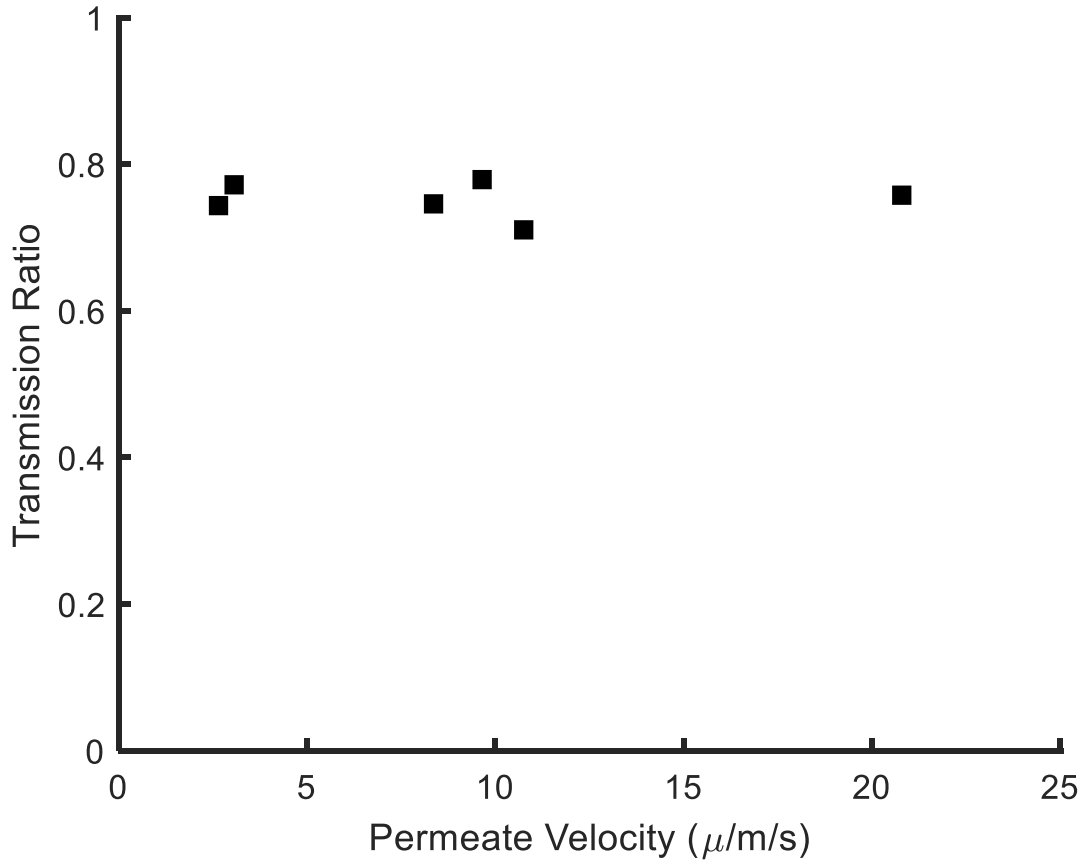

Figure 4.10: Transmission ratio as a function of permeate velocity at a fixed shear rate of 87,763 1/s for the 5 µm particles using the 20 µm membrane.

To match the theoretical data to the experimental results, Equation 12 was used by setting the mixed boundary layer height, z, to about 20 µm. This allowed the magnitude of the theoretical predictions to be shifted up to the experimental results, allowing them to be plotted as shown in Figure 4.11.

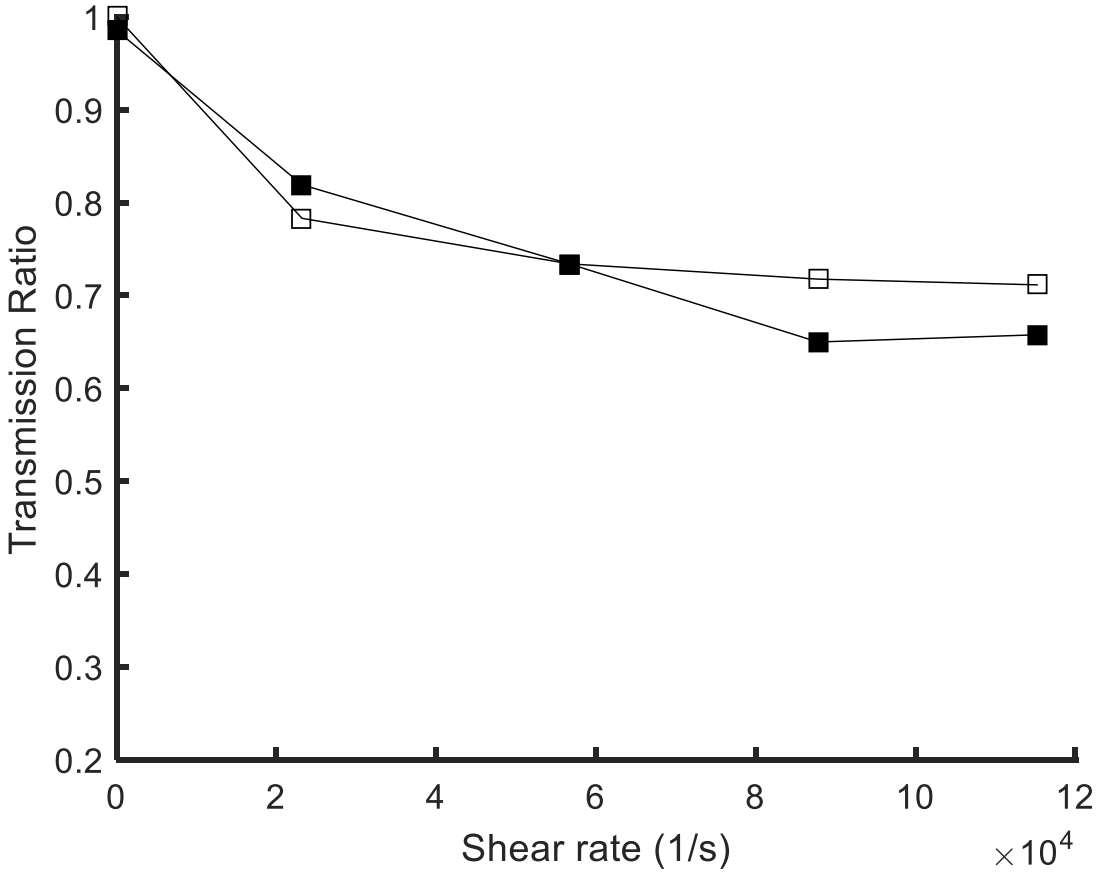

Figure 4.11: Plot of the transmission ratio as a function of shear rate for the 5 μm spheres through the 20 μm membrane. The closed symbols indicate experimental results and the open symbols indicates theoretical predictions.

There is a pretty good match between the experimental result and theoretical predictions in this case when the boundary layer thickness is adjusted. The trends again match up, however the decrease in transmission theoretically is not as it is for the experimental results. Between the shear rates of 20000 1/s and 80000 1/s, the gradient of decrease in transmission for the experiments is noticeably steeper than it is for the theoretically predicted values. Additionally, the transmission almost becomes constant theoretically, while for the experiments, a decrease can still be observed

along with a slight increase in transmission at the largest shear rate. Again, this can be attributed to the increase in turbulent diffusivity as the shear rate increases,

The final set of experiments using the cross-flow equipment was carried out to see if separation of nanospheres occurred because of particle ratcheting. As was mentioned previously, similar cross-flow experiments were done with globular proteins by Hurwitz and Brantley using two different pore sized membranes. Nanospheres were used in our experiments to see if their behavior was the same as the sphere-like globular proteins. A 100 KDa membrane was used, which corresponds to a pore diameter of approximately 10 nm. Using the synthesis method described in Appendix B, two set of spherical nanoparticles were created, sized 1.5 nm and 3.4 nm in diameter. The experimental results obtained are shown below in Figure 4.12 along with the predicted values using the base case assumptions.

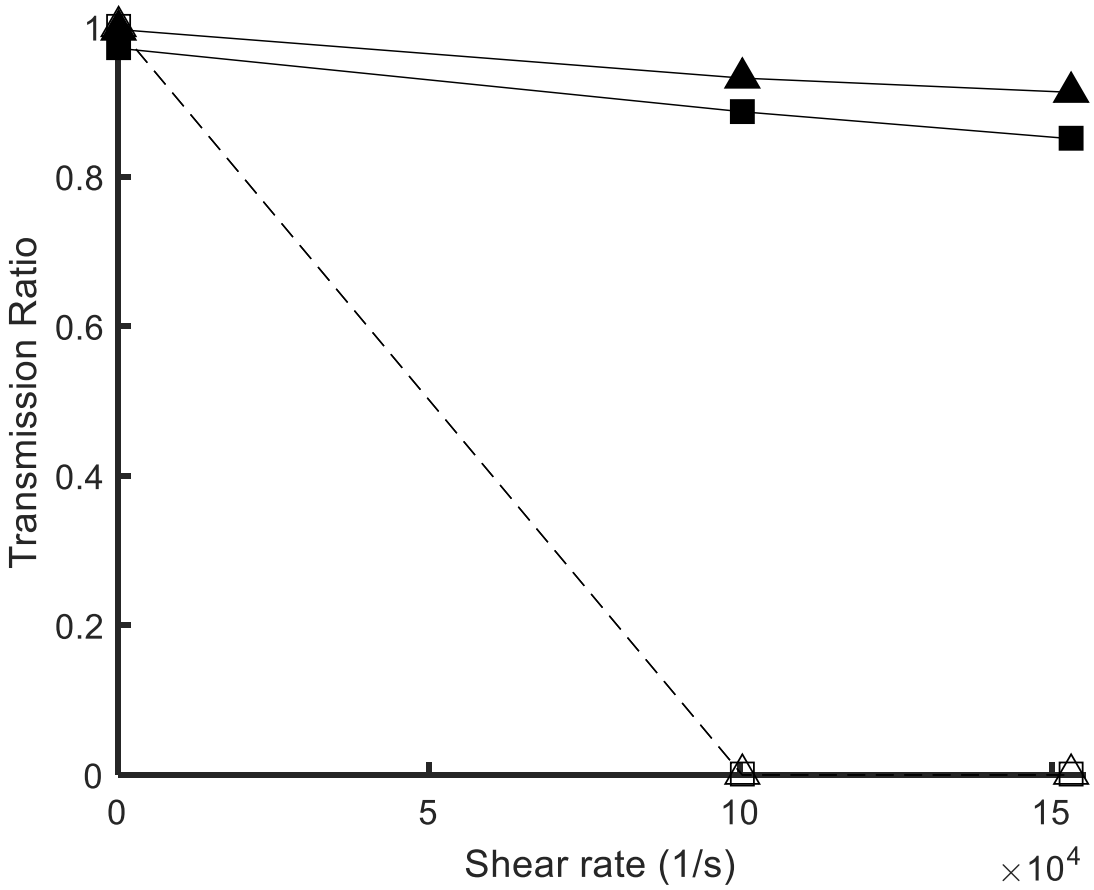

Figure 4.12: Transmission ratio as a function of shear rate for the nanospheres. The black lines indicate experimental results and the red dashed lines indicated predicted values. (▲ – 1.5 nm particle, ■ – 3.4 nm particle). The permeate velocity for both cases is 3.13 μm/s.

Using the base assumptions (Equation 19) to get the predicted values gives 0 transmission of the particles for both the sizes when using a membrane whose pore radii is 5 nm. However, this is not the case experimentally as the transmission ratios for both particles are close to 1. Further analysis needs to be done for these sets of results, to see what sort of adjustments can be made to the base equation to match the theoretical values closer to the experimental results.

Conclusion

Through the experiments and studies that were conducted, we could successfully demonstrate that lift-based cross-flow techniques allow for sieve-free separation based on size. Theoretical predictions also were derived to show that the same trends, such as the decrease in transmission ratio with increasing shear rate, could be achieved. Further analysis of the equations allowed for modifications to be made to the particle flux boundary condition that improved trends made between experiments and theory and magnitude match. The study of sieve-free separation of nanoparticles was started and we could show experimentally that a slight decrease in transmission ratio could be achieved with increasing shear rate. Since the nanoparticles are too small to experience inertial based lift, we can attribute this to ratcheting of particle trajectories. However, further experiments and theoretical analysis needs to be done to better understand the mechanism behind the separation of these particles.

Since we have shown that sieve-free separation is possible for spherical particles of different size, the next step is to observe the separation of particles that are non-spherical. A first step was taken was to stretch 5 μm polystyrene spheres into ellipsoids with an aspect ratio of 3. Synthesis of these particles is described in Appendix A. The next steps will be to run laminar experiments with these ellipsoidal particles and observe the transmission ratio with varying shear rates and permeate velocities.

Appendix A

Membrane Characterization

It is difficult to know the pore size of a membrane by looking at the cylinder since the pore diameters are very small. Since a few of the cylinders given weren't labeled with the pore size, a bubble point test was conducted. This was done by placing caps on both open ends of the stainless steel porous cylinder and clamping it so that it was sealed, as shown in Figure 3.3. The top cap has a tube fitting which can connect to a gas cylinder to pump air through. The full set up with the membrane and caps are submerged in water and allowed to become completely saturated. Once saturated, the tubing from the air cylinder is connected to the fitting and the air pressure is increased gradually until the first sign of a bubble appears on the surface of the cylinder. The pressure is recorded and input into Equation A.1 to determine the approximate diameter of the pores:

Figure A.1 Bubble point set up of porous stainless-steel cylinder

$$\frac{\pi d^2 P}{4} = d\sigma\pi\cos(\alpha), \qquad [A1]$$

P is the bubble point pressure and d is the diameter of the pore, which we are trying to find. We assume the liquid-solid contact angle is $\alpha = 0°$. This is because water molecules are strongly attracted to the bare metallic surface of the membrane, corresponding to a contact angle of 0° [15]. Finally, σ is the surface tension of the wetting fluid, which in this case is water. Equation A1 can be simplified and rearranged to give

$$d = \frac{4\sigma}{P} \qquad [A2]$$

The bubble point pressure from one of the tests was determined and the surface tension of water at room temperature was 72 dynes/cm. Therefore, from this test it could be confirmed that the largest pores in the cylinder were 5 µm in diameter. To further validate these values, AFM measurements were also taken of a portion of the surface of the membranes to characterize the pores and surface roughness as shown by the images in Figure A.2. The image on the left shows a three-dimensional topography of the 20 µm membrane while the image on the right shows a 2-dimensional surface map of the 20 µm membrane.

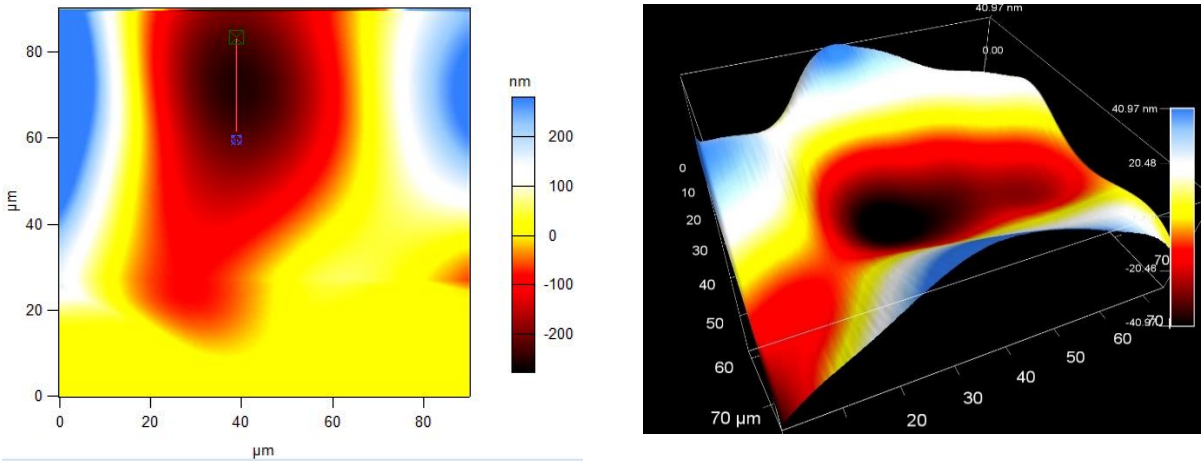

Figure A.2 AFM images of the membrane surfaces in 3D and 2D

One issue with AFM is that the probe that scans the sample and measures the surface roughness cannot deflect deep enough into pore to define a clear boundary of the pore. Instead getting a 3D image with a clearly defined circular well to represent the pore boundary and depth, a valley is formed, only allowing for an approximation to the edge of the pore to determine the diameter.

Particle Characterization

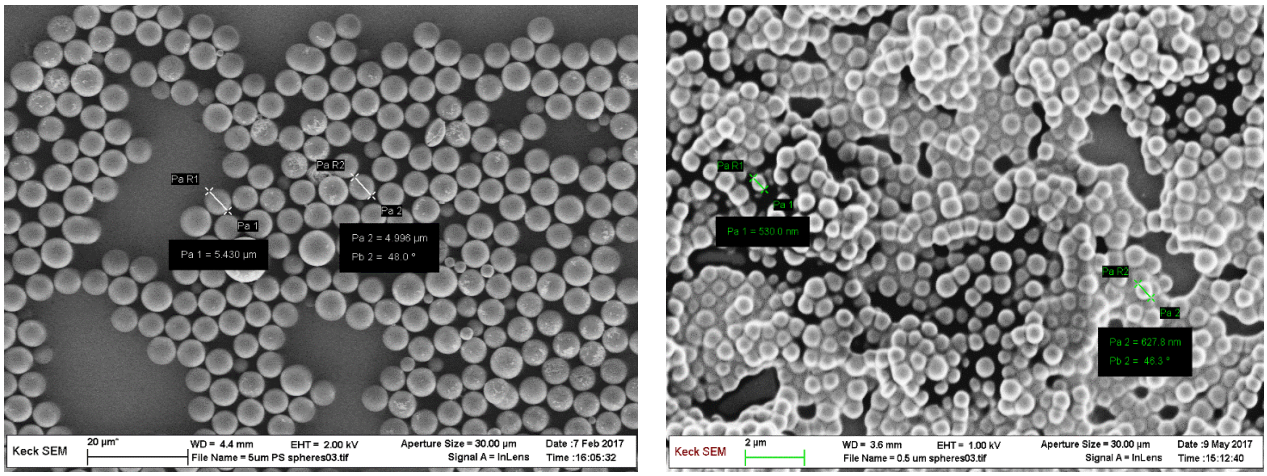

Figure A.3 SEM Images of the 5 µm (left) and 0.5 µm (right) polystyrene particles

Figure A.3 shows the SEM images of both the polystyrene spheres. The sample is monodispersed and the particles are indeed spherical in nature.

Organic hybrid nanosphere synthesis

The synthesis method for the nanoparticles used to test the predictions of sieve-free separation by trajectory ratcheting have been developed at Cornell by Krysmann et al[16] for use as tracers in geological reservoirs. They provided the conditions to create a range of sizes. Our focus was to use their synthesis method to create another size other than 3 nm nanospheres. An additional

study done by Li et al[17] has provided a modification to the recipe to create monodisperse nanospheres that are around 3 nm in diameter. We chose to use nanospheres of well-known size in these experiments to minimize the uncertainties associated with limited knowledge of size, non-spherical shape, flexibility, and intermolecular forces associated with proteins.

The table below provides the one step pyrolysis methods to create both sizes of particles for use in the experiments.

Table A1: Methods for synthesizing C-dots

Synthesis Method 1 (3.4 nm particles)	**Synthesis Method 1 (1.5 nm particles)**
Mix citric acid and ethanolamine in a 3:1 molar ratio and stir until completely mixed. While stirring, heat the mixture at 70°C until about 2/3 of the water has evaporated. Put the remaining solution in the oven and raise the temperature 10 °C/min until it's 200 °C. Pyrolyze for 8 hours.	**Mix citric acid and ethanolamine in a 3:1 molar ratio and stir until completely mixed. While stirring, heat the mixture at 70°C until about 2/3 of the water has evaporated. Put the remaining solution in the oven and raise the temperature 10 °C/min until it's 200 °C. Pyrolyze for 7 hours.**

Cryo-Transmission electron microscopy and dynamic light scattering techniques were used to characterize the size and shape of the nanospheres and ensure that a monodisperse sample was synthesized. Figures A.4 – A.6 show the results obtained by using these analysis tools.

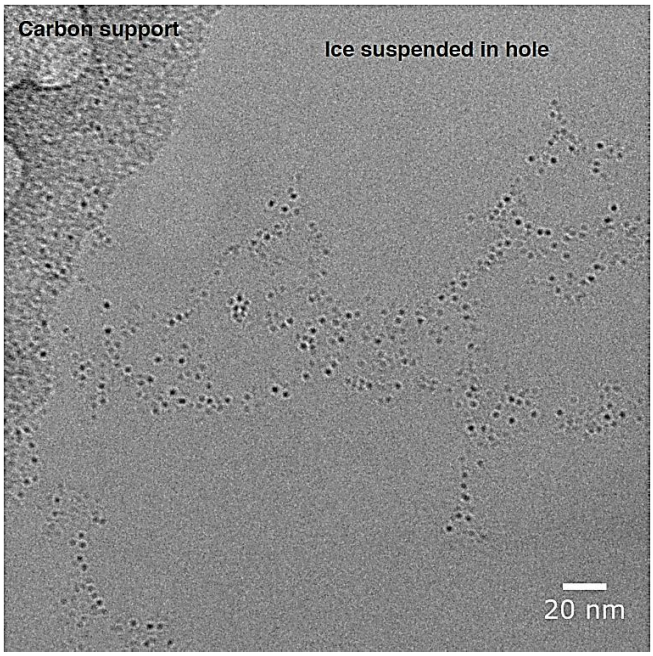

Figure A.4: Cryo-TEM images of the 3 nm nanospheres

Temperature (°C):	25.1	**Duration Used (s):**	70
Count Rate (kcps):	114.7	**Measurement Position (mm):**	3.00
Cell Description:	Disposable micro cuvette (40µl)	**Attenuator:**	11

			Size (d.nm):	% Number:	St Dev (d.nm):
Z-Average (d.nm):	101.1	**Peak 1:**	3.442	100.0	0.3013
PdI:	0.448	**Peak 2:**	0.000	0.0	0.000
Intercept:	0.599	**Peak 3:**	0.000	0.0	0.000

Result quality : Good

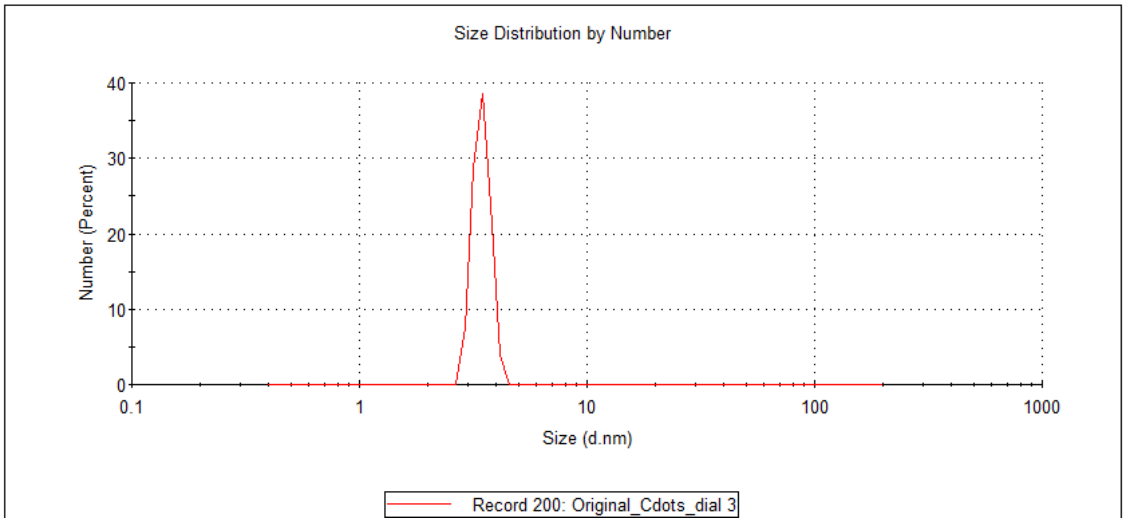

Figure A.5: DLS analysis of the 3 nm spheres

Temperature (°C):	25.1	**Duration Used (s):**	60
Count Rate (kcps):	279.6	**Measurement Position (mm):**	3.00
Cell Description:	Disposable micro cuvette (40µl)	**Attenuator:**	10

			Size (d.nm):	% Number:	St Dev (d.nm):
Z-Average (d.nm):	238.1	**Peak 1:**	1.561	100.0	0.1257
PdI:	0.263	**Peak 2:**	0.000	0.0	0.000
Intercept:	0.664	**Peak 3:**	0.000	0.0	0.000

Result quality : **Refer to quality report**

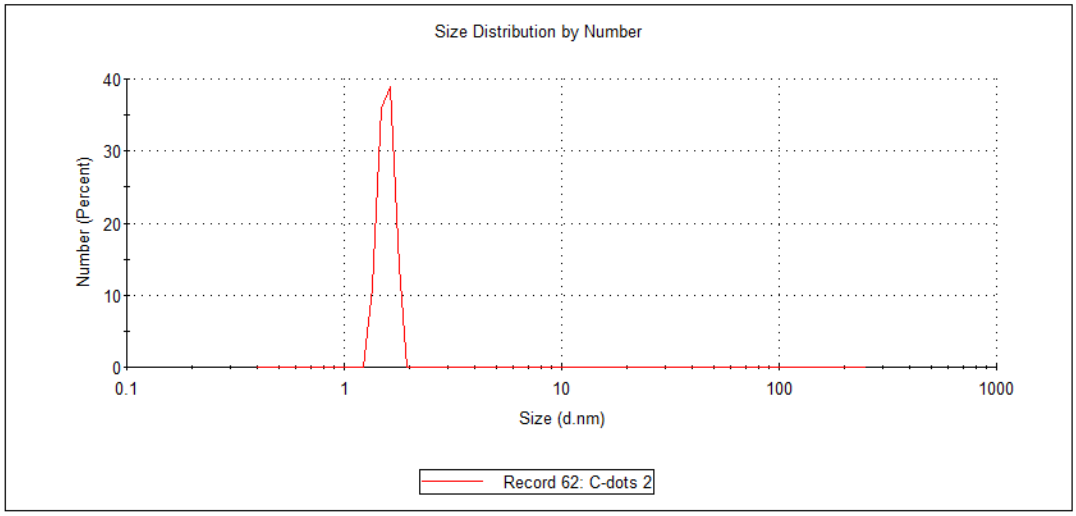

Figure A.6: DLS analysis of the 1.5 nm spheres

Determining the feed stock composition

Polystyrene does not disperse well in water and sticks to metal due to surface charge attractions. Initially, 1 L of DI water and about 1g of polystyrene was put into a bottle and allowed to be stirred overnight. This caused minimum dispersion of the particles in solution and most of it settled to the bottom due to the density difference between polystyrene and water.

To prevent aggregation of the particles and sticking to the metal surfaces, surfactant needs to be added to coat the polystyrene spheres and neutralize their surface charge. In addition to that, to ensure dispersion of the particles in the water, an ultrasonic bath system can be used for rapid distribution throughout the solution.

The first surfactant that was tried was sodium dodecyl sulfate (SDS). It is an anionic surfactant that is used commonly in the lab. An absorption spectrum was taken of the polystyrene-SDS mixture to make sure that the polystyrene concentration could be observed without interference. However, it was found that SDS had an absorption reading that overpowered the absorption value of polystyrene in the spectrophotometer at the full spectrum of wavelengths. Sodium chloride was added to see if the absorbance of the SDS could be minimized and, by adding about 0.5 mM, small absorbance readings of the polystyrene could be detected. This solution was tested in the cross-flow system to see if a baseline set of results could be achieved and that the equipment was functioning properly with no leaks or damaged parts.

Achieving a baseline set of results

A solution was made up with 700 ppm of the 0.5 µm polystyrene spheres, 4 mM of SDS and 0.5 mM of NaCl. The feed rate from the tank was set to 2 GPM and fluid was run through the cross-flow system with the 5 µm membrane. The spin rate was set to 1000 RPM and the permeate velocity was set to an initial value of 50 µm/s. The system ran until steady state was achieved and samples of the permeate stream were taken to measure the concentration. The permeate velocity was incrementally raised and allowed to reach steady state before concentration values were taken. Figure A.7 shows a graph of the results obtained.

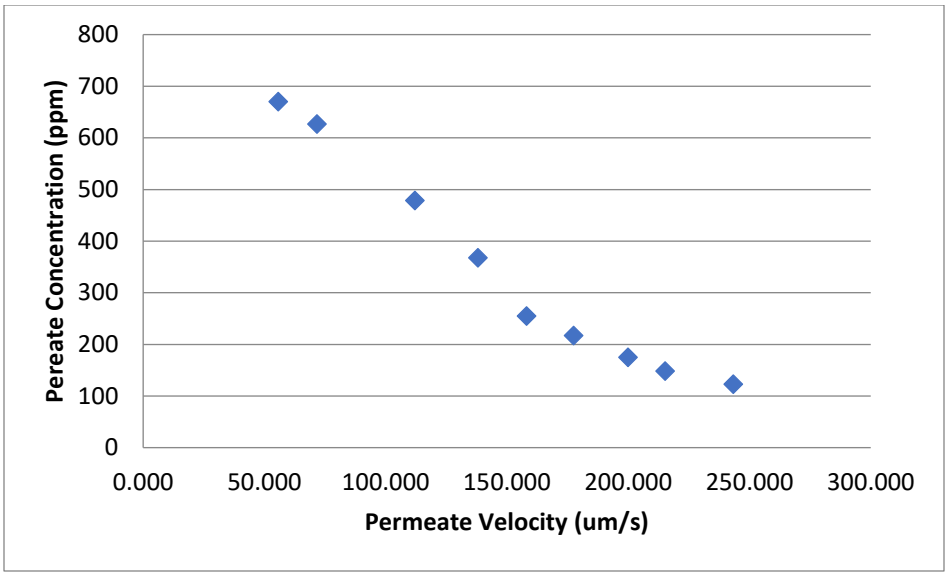

Figure A.7: Plot of the permeate concentration as a function of permeate velocity. The permeate velocity increases with the increase in the feed rate.

As can be seen from Figure A.7, the concentration in the permeate stream seems to decrease with increasing permeate velocity when the shear rate is set constant. This is in fact the opposite of what should be expected. At a constant shear rate, when the permeate velocity increases, we expect that the drag on particles towards the pores becomes greater than the effects of lift on the particles trying to push them away from the surface of the membrane. This means that the concentration of particles should increase with increasing permeate velocity. Also, by turning off the shear, the particle concentration did not go back to the initial bulk concentration value, but rather was significantly lower than the initial value. To investigate where the particles went, the Couette Cell was opened. As shown in Figure A.8, it was found that most of the particles were sticking to the surface of the cylinder, possibly due to the interaction of the polystyrene with the stainless-steel due to insufficient amount of surfactant. In addition, SDS is a highly foaming surfactant, so it is also possible that the spinning was generating foam in the cylinder, trapping the particles in the foam and settling it on the cylinder.

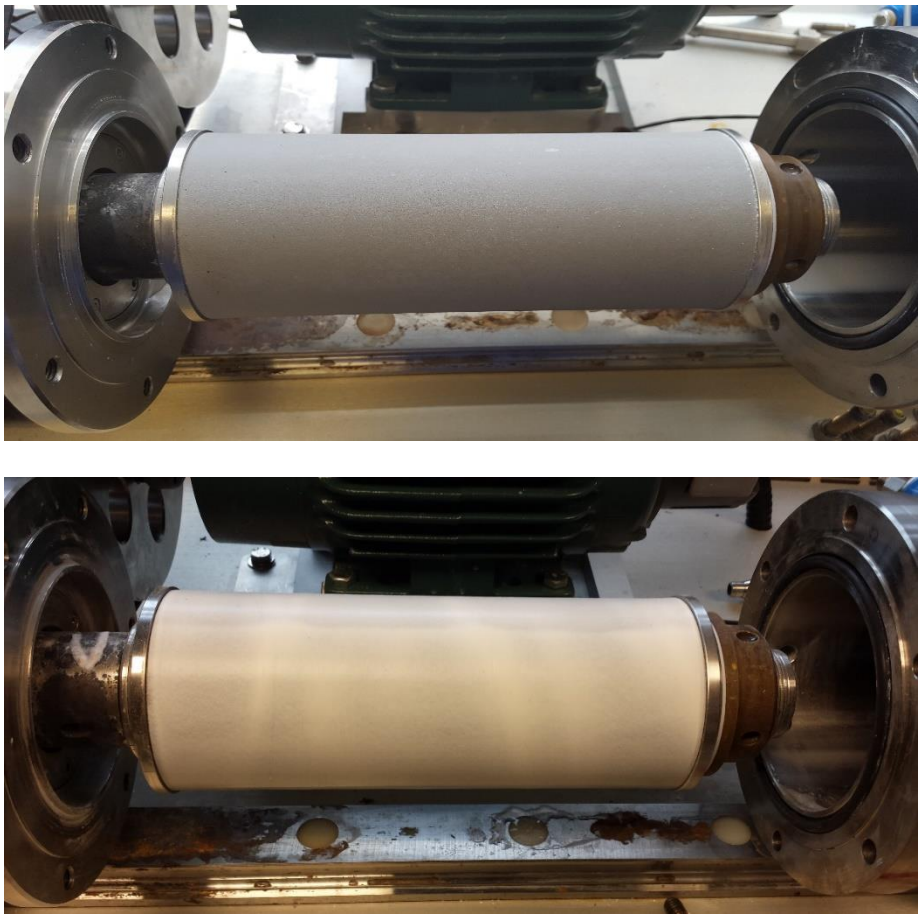

Figure A.8: The porous cylinder prior to running experiments (top) and after running the first set of experiments with the polystyrene, SDS and salt (bottom).

Adding more surfactant and preventing any air in the system to generate foam could have prevented sticking. However, adding more SDS would mean that more salt needs to be added to ensure that the proper detection limits could be reached, which subsequently increases the possibility of aggregation. To simplify the preparation and detection of the particles in solution, other surfactants were tried, mainly ones that were non-ionic, to additionally minimize the effects of foaming. Heffer at al[22] found that EO/PO based defoamers contain polyethylene glycol (PEG) and polypropylene glycol (PPG) copolymers. This proved to be beneficial since poloxamers (copolymers of PEG and PPG) are also an excellent example of nonionic surfactants.

Therefore, the final choice was to use a triblock co-polymer of PEG-PPG-PEG. This was a chemical that was readily available in the lab and helped disperse the polystyrene a lot quicker in water. A full absorbance spectrum curve was done on a sample of the co-polymer and it was found that at the full range of wavelengths, except for a wavelength of 290 nm, there was no significant absorbance of the triblock co-polymer, as shown in Figure A.9. In addition, changing the concentration of the co-polymer used didn't influence its absorbance spectrum. In addition, it was found that the polystyrene could show absorbance values at very low concentration when using higher wavelengths. Using the co-polymer, absorbance readings could be taken at a wavelength of 850 nm, which ensured that concentrations as low as 1 ppm of the polystyrene spheres could be detected in the water.

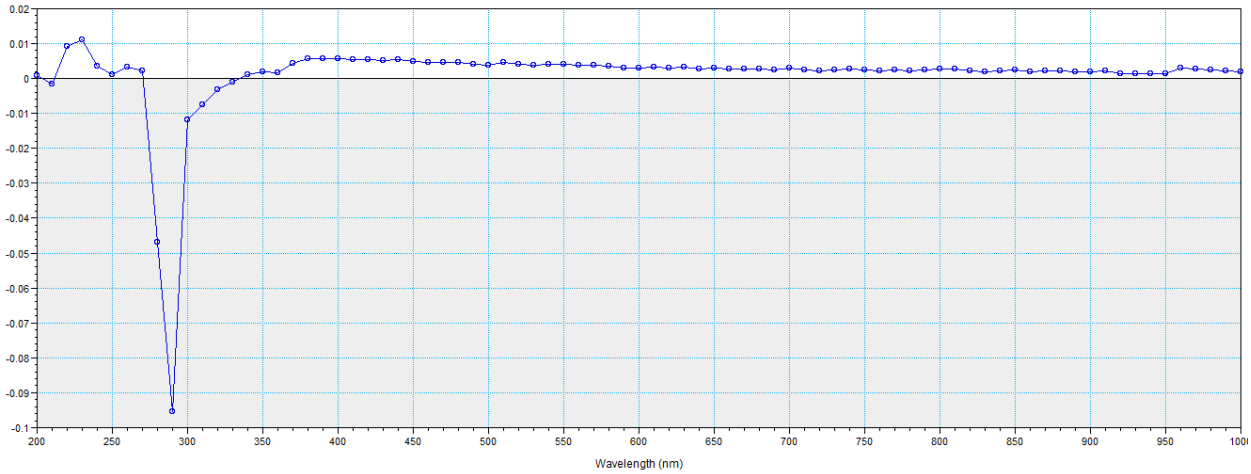

Figure A.9: Spectrum analysis on the absorbance of PEG-PPG-PEG as a function of the wavelength

No data has been found on the critical micelle concentration for PEG-PPG-PEG. The molecular weight of the co-polymer is ~5800 kDa. Through trial and error, it was found that for every 1 g of polystyrene put in the solution, 2 g of the co-polymer was more than sufficient in preventing the particles from sticking to the porous cylinder and not have much foaming. However,

it was found that in general, concentrated solutions of poloxamers can form hydrogels when mixed with water[23]. In the case of these experiments, the amount used in comparison to the volume of water used is small, so there is no worry of hydrogels forming. Two sets of experiments were conducted to determine the efficiency of the triblock as a surfactant.

In the first set, there was no spin set and the fluid ran through the system at a constant feed flow rate. Every 20 minutes a sample was taken from the feed stream and permeate stream to assess the concentration of the sample. The concentration results plotted against time is shown below.

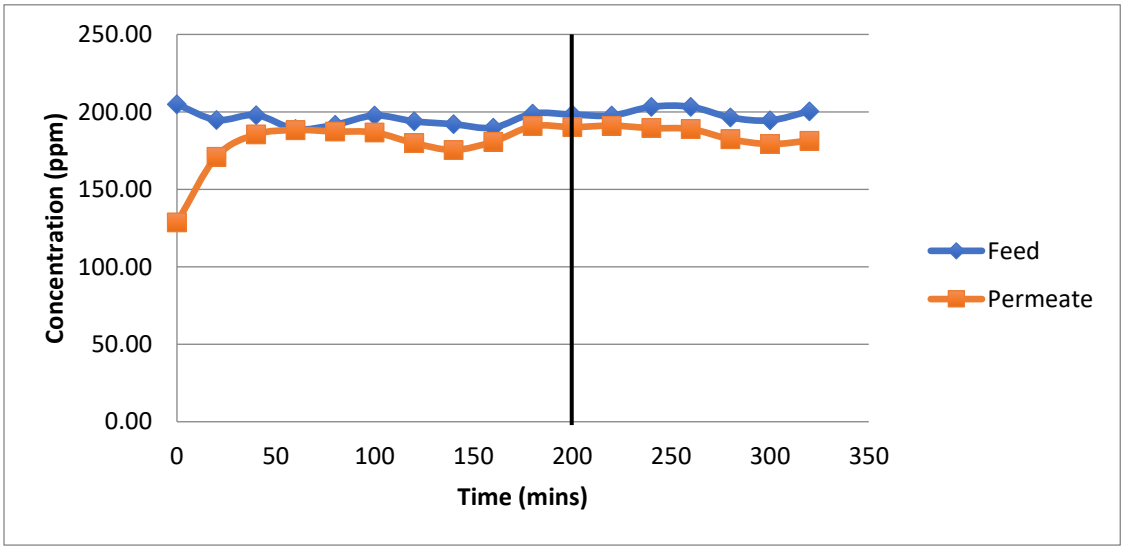

Figure A.10: Feed and permeate concentration as a function of time when there is no shear

Due to the large holdup volume in the system, a long residence time is required to obtain equilibrium of the system. This is evident in the beginning of the graph in Figure A.9, where the permeate concentration is slowly increasing and only reaches close to the feed concentration after 50 minutes. As can be seen from the graph in Figure A.10, the concentration of both the feed and permeate stays pretty much consistent over a long period of time without any significant decrease. The vertical line in the figure indicates the completion of one residence time on the permeate side.

In addition, after this experiment, once the Couette cell shell was opened, it was found that there were no particles stuck to the porous cylinder.

The second test was to see the effect of the surfactant while the cylinder was spinning. For this, the feed rate was set to 2 GPM and the shear was set such that the theoretical lift velocity was 106 µm/s. The permeate velocity was then set to 103 µm/s. The outcome that would be expected from this is that some of the particles get retained in the outer portion of the spinning cylinder by lift and the rest pass through the filter, resulting in a permeate concentration slightly lower than the feed concentration.

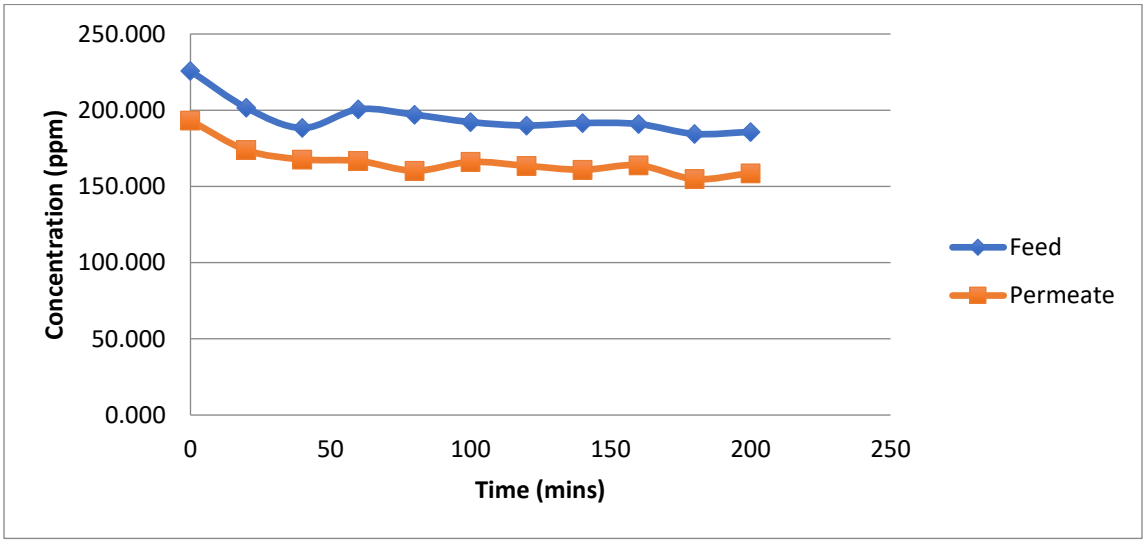

Figure A.11: Concentration of feed and permeate over time at a constant spin and feed rate

As can be seen in Figure A.11, there is a slight decrease in the permeate concentration compared to the feed concentration and both concentrations stay constant after an initial unsteady period. All the tests that were done have effectively shown us the correct combination of steps that need to be taken to ensure that a baseline set of results can be achieved. This means that the polystyrene particles are not sticking to any part of the equipment when run with and without spinning the outer cylinder and a suitable surfactant has been found that keeps the particles from

interacting with each other and the porous cylinder, but doesn't contribute to the spectrophotometer readings for concentration.

Synthesis of ellipsoidal particles

We want to extend the idea of sieve-free cross flow separation to non-spherical particles. To do that, we aim to study the translational and rotational motion and fluid velocity disturbance of spheroidal particles. A paper by Ho et al[23] proposed a method to stretch polystyrene spheres into ellipsoids with different aspect ratios. The spheres are dispersed in a solution of polyvinyl alcohol (PVA) and water and dried at room temperature on trays to form thin films that are around 70 μm thick. They are then cut into 2 in x 3 in strips. These strips are clamped on a metal frame, heated rapidly in an oil bath to 180 °C and stretched to a predetermined extent to convert the spheres into ellipsoids. The apparatus to stretch the films was made by Glenn Swan and is shown in Figure A.12. The stretched film is rapidly cooled and dissolved in a solution of isopropyl alcohol (IPA) and water and heated to 80 °C to dissolve the PVA. The dissolved solution is centrifuged at 8000 RPM and the pellet obtained from centrifugation is dispersed again in a new solution of IPA and water and the process is repeated 3 more times until most of the PVA has been removed from the polystyrene. It is important to note that all the PVA was not be removed from the polystyrene and there still may be some residue left. Potentially running more than 3 dispersion cycles with IPA and water can rectify this and remove the PVA.

This method was attempted on the 5 μm polystyrene spheres using a metal frame system as shown in Figure A.12.

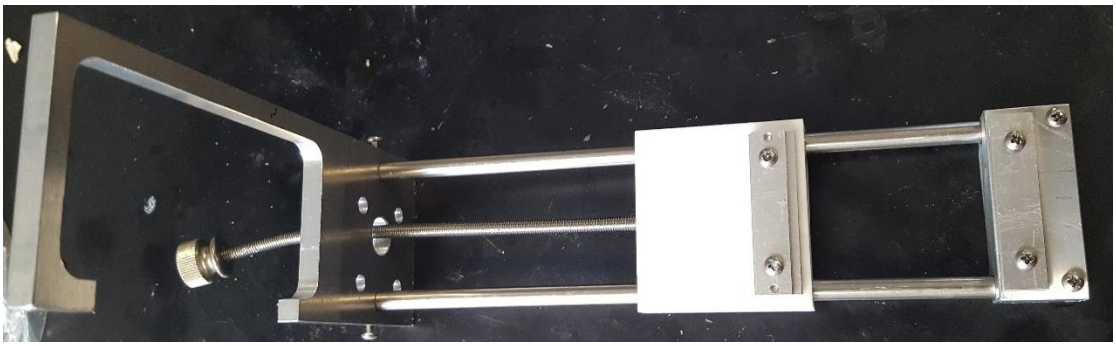

Figure A.12: Clamp system that is used to stretch the particles. The pieces of film are secured using the two metal rectangular pieces and screwed tightly so that they remain fixed. The bottom half of the clamp with the film is dipped into the silicone oil bath and the handle is pulled to stretch the film

The films were stretched to create ellipsoids of 2 different aspect ratios. Figure A.13 shows SEM micrographs of a single stretched particle with an aspect ratio of 2 along with a cluster of particles that have aspect ratios of ~3.

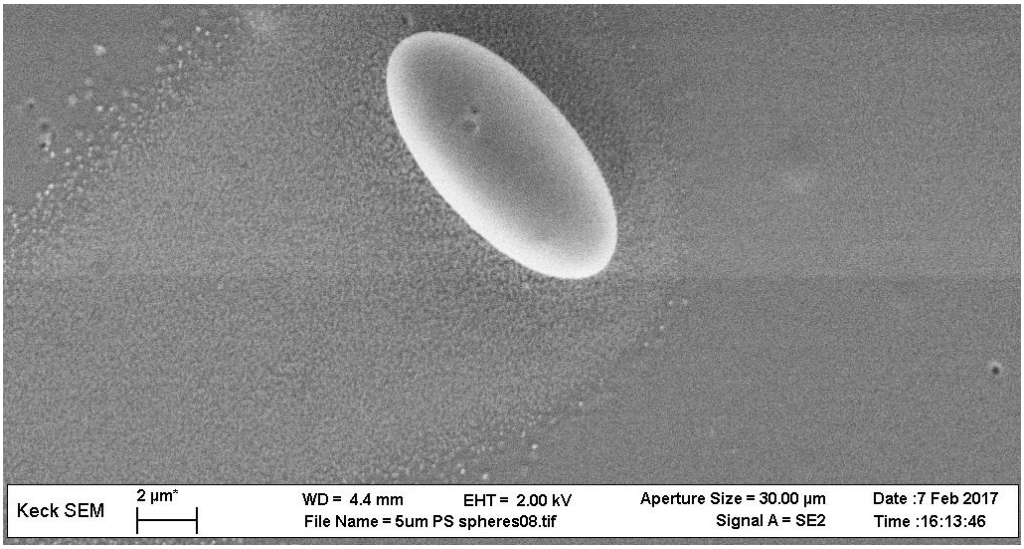

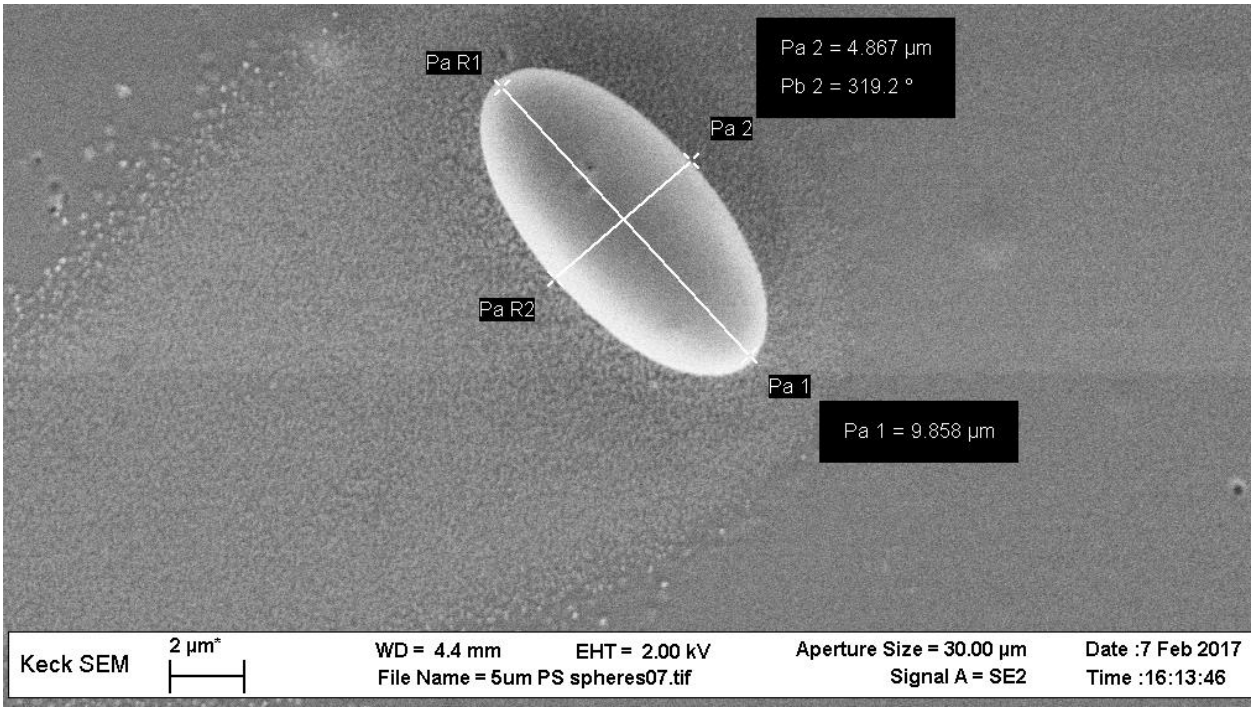

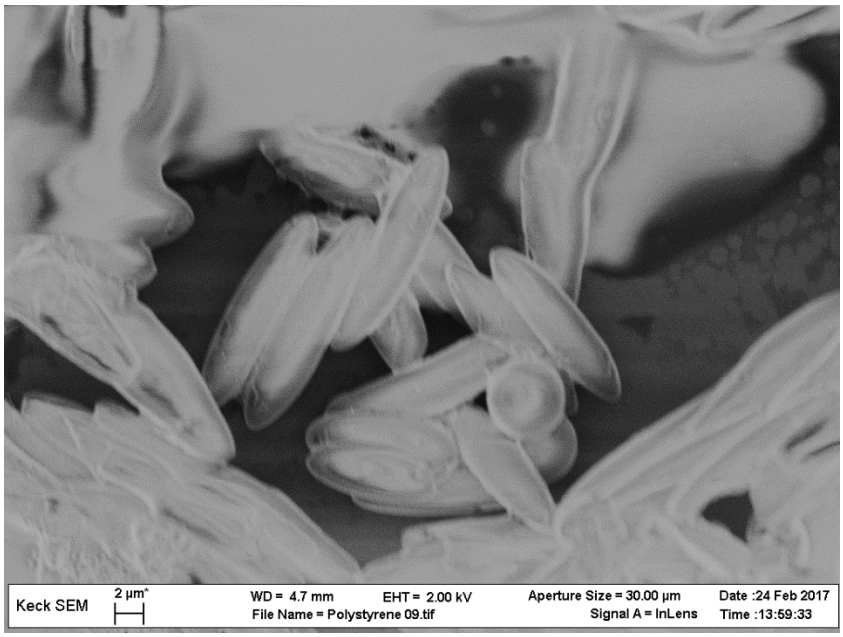

Figure A.13: SEM micrographs of the stretched ellipsoidal particles

Appendix B

Pall Synthesis Notes

Preparation of Highly Crosslinked Mondisperse Polystyrene Microspheres by Dispersion Polymerization

Report Number: **AM-D3-013396**

Project Number: **TEC-AM-000264**

Laboratory Notebook: **Notebook #1284 Page 39**

Date: **February 23, 2015**

By: **Yi Wang**
3669 State Route 281
Cortland, NY 11050
Tel. 607.758.4508

For: **Mark Hurwitz**

1.0 Summary

Synthesis of 0.5 µm polystyrene was successfully finished in one batch. Synthesis of 5 µm polystyrene did not lead to the desired result. The problem is the temperature of condensation water is too warm. Therefore, the ratio of toluene/IPA may change during the 24-hour reaction period. Another problem may arise from the poor quality of stirring.

2.0 Introduction

This request is to support Mark Hurwitz by synthesizing small batches of polystyrene particles. For this study two small batches of 0.5 µm and 5.0 µm polystyrene microspheres will be prepared through dispersion polymerization. The microspheres will then be provided to Port Washington for casting into polyvinylalcohol (PVA), and stretching where they are to be transposed to the shapes of ellipsoids. The ellipsoids are to be used for some cross-flow studies.

3.0 Test Methods

Synthesis of 0.5 µm Polystyrene Spherical Colloids

1. Clean all glassware and assemble synthesis apparatus appropriately.
2. In a separate funnel, add 200 mL of styrene (Alfa Aesar, lot# 10182421) and 200 mL of 10% sodium hydroxide (BDH, Lot#311024) to remove the anti-polymerizer. Shake separate funnel well and allow for separation to occur. Drain the sodium hydroxide portion and repeat treatment of styrene with 200 mL of 10% sodium hydroxide two additional times. Collected styrene in a 500 mL glass bottle, and store in refrigerator.
3. Add 2000 mL of ethanol pure 200 proof (EMD, Lot# 53164346) and 800 mL of DI water into a 5 L round bottom four-neck flask and heat to 70 °C in an oil bath.

4. One neck of flask is connected with water condenser; one is connected to nitrogen inlet; one is used for mechanic stir; one is connected with temperature probe.
5. Purge solution in flask with nitrogen and maintain under nitrogen condition.
6. Add 4.4 g of sodium lauryl sulfate (Sigma Aldrich, Lot#MKBQ4946V) and 4 g of potassium persulfate (J. T. Baker, Batch#0000066219) to the ethanol/water solution.
7. Purge the solution for 5 minutes.
8. Transfer 180 mL of sodium hydroxide treated styrene into a pressure equaling dropping funnel. Take nitrogen inlet off the neck of flask, and put the funnel on. Dropwise add styrene into the flask. After adding styrene, take off the funnel, and put nitrogen inlet back.
9. Rapidly stir the emulsion solution for 8 hours at 70 °C.
10. Stop the polymerization reaction by stopping heat and remove the round bottom flask.
11. Transfer equal portions of the polymer solution into centrifuge tubes.
12. Centrifuge for approximately 1 hour or until the polymer has separated from the solution.
13. Decant the solution portion (top layer); filter it through a 0.45 µm 47 mm nylon membrane disc; then wash with ethanol twice; collect the solid.
14. Combine all polymer solid and dry in a vacuum oven at 60 °C for two days.
15. Weigh and record the mass of the synthesized polystyrene beads.
16. Calculate the percent yield.
17. This protocol is designed based on a literature: *Jianhui Zhang, etc. Materials Letters, 57 (2003), 4466-4470.*

SEM Imaging

1. Tamped sample received from Yi Wang onto a sticky coated carbon stub.

2. Au/Pd coated each sample to render them conductive.
3. Placed in the Hitachi SEM.
4. Aligned the scope per typical operating levels.

4.0 Results

The experimental apparatus for both reactions are shown in **Figure 1** and **Figure 2.**

An SEM image was collected for the 0.5 µm polystyrene particles and is shown in **Figure 3**. There were two types of solid products resulting from the synthesis of the 5 µm polystyrene microspheres. SEM images are shown in **Figure 4** and **Figure 5**.

Particle size analysis of the 0.5 µm polystyrene microspheres will be reported separately. Particle size analysis for 5um polystyrene was not carried out.

We obtained 146.3 grams of the 0.5 µm polystyrene particles for a yield of 89%. For the 5 µm polystyrene particles, only 30 grams of usable polystyrene-powder was obtained, while 18 grams of a polystyrene-chunk that is not usable was obtained.

Yi Wang
Scientist II
Scientific & Laboratory Services
Pall Corporation

Addemdum by Mark Hurwitz, February 27, 2015:

Email from Shawn Hubbard, February 23, 2015

shawn_hubbard@pall.com

Mark,

Hello. Yi has completed a second attempt at preparing 5 µm polystyrene particles. Please see the images below. After an initial attempt to make a larger batch, only a large chunk of polymer was obtained (The stirrer had quit working some time in the night). A second attempt was done utilizing a smaller batch size and is described below in the following procedure. Results of SEM analysis indicate that the portion of polymer that formed chunks and was left in the flask had much material that is unusable. The powdered material looks better, but is still not as good as what was obtained last year. In total, we obtained about 30 grams of this material that may be usable. We believe that the stirring necessary to ensure spherical particle formation is critical and that our equipment is inadequate in this regard when increasing the batch size. We also do not have more time to continue preparing these particles and to modify our test set up as is apparently required. Therefore, we ask that you try to find someone at Cornell that with better equipment for polymer synthesis can prepare these particles on a much larger scale than we can. We have all together 146 grams of the 0.5 µm spheres and about 22 grams of the 5 µm spheres. In addition, we have about 30 grams of the 5 µm spheres from the most recent batch that may or may not be usable depending upon your thoughts.

Kind regards,

Shawn Hubbard

PS, In answer to your previous question about the use of 3% toluene, it is used as a co-solvent to aid in the solvation of the styrene. Any other aromatic co-solvent would be at least as hazardous as toluene, e.g., benzene or xylene. Maybe the people at Cornell could suggest a less hazardous co-solvent, but it is my belief that an aromatic solvent is necessary. It is also our feeling that most universities are not as particular about safety concerns as industry must be.

Synthesis of 5 µm Polystyrene Spherical Colloids

1. Pass both styrene and divinyl benzene (DVB) through two packed columns for removing *tert*-butylcatechol purchased from Aldrich. Collect treated styrene and divinyl benzene individually and store in refrigerator.

2. Make 400 gram of a solution with isopropanol (IPA) and toluene (97:3 w/w).
3. Add 380 gram of IPA and toluene solution into a three-necked 1-L round bottom flask with a magnetic stirrer. Put the flask into an oil bath which is kept at 70 °C.

4. Three necks of flask are connected with water condenser; nitrogen inlet and 100ml pressure equaling dropping funnel. A stir bar is used for stirring.

5. Add 7.8 gram of poly(N-vinylpyrrolidone (PVP, mw: 40,000); 42 gram of treated styrene; 0.9 gram of DVB into the flask. Bubble nitrogen through the solution. Stir at 150 rpm for 1 hour.

6. In a glass vial weigh 1.56 gram of 2,2'-azobisisobutyronitrile (AIBN) and 18 gram of styrene, then add 20 gram IPA and toluene solution to make sure AIBN totally dissolved.

7. Transfer the above solution into the dropping funnel. Add drop-wise into the flask.

8. The reaction can continue for 24 hours.

9. Pour the reaction solution into 400ml of methanol at room temperature. The product collected from this part is called polystyrene-powder.

10. There are some chunks left in flask after pouring out the reaction solution. The product collected from this part is called polystyrene-chunk.

11. Wash both parts with methanol, methanol and water (50:50 v/v), and water, individually. Transfer to a glass dish, dry under vacuum at 50 degree for two days.

12. Obtain 30 gram of polystyrene-powder; 18 gram of polystyrene-chunk.

13. This protocol is designed based on the following literature: *J. Chol, etc. Journal of polymer Science: Part A: Polymer Chemistry.* Vol. 40, 4368-4377 (2002)

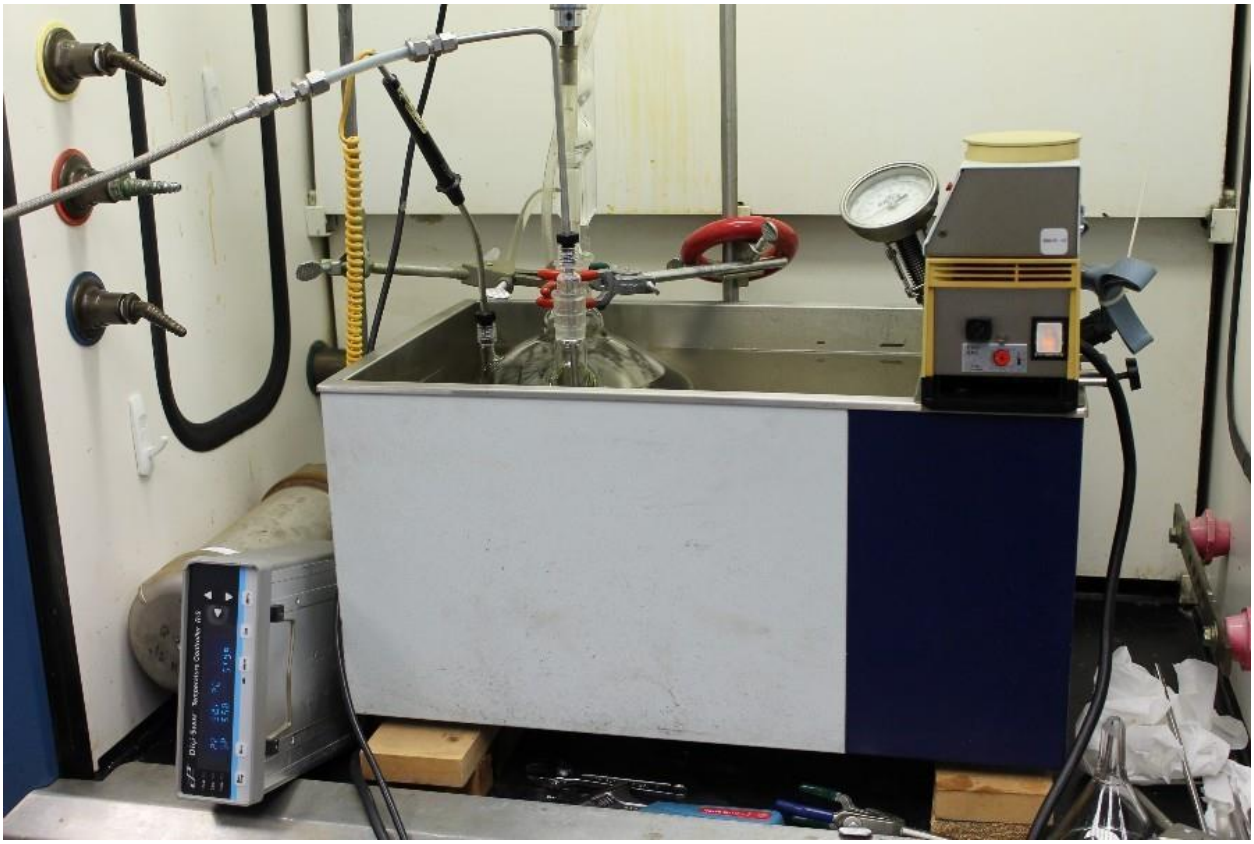

Figure B.1: Experiment Setup for 0.5 um Polystyrene

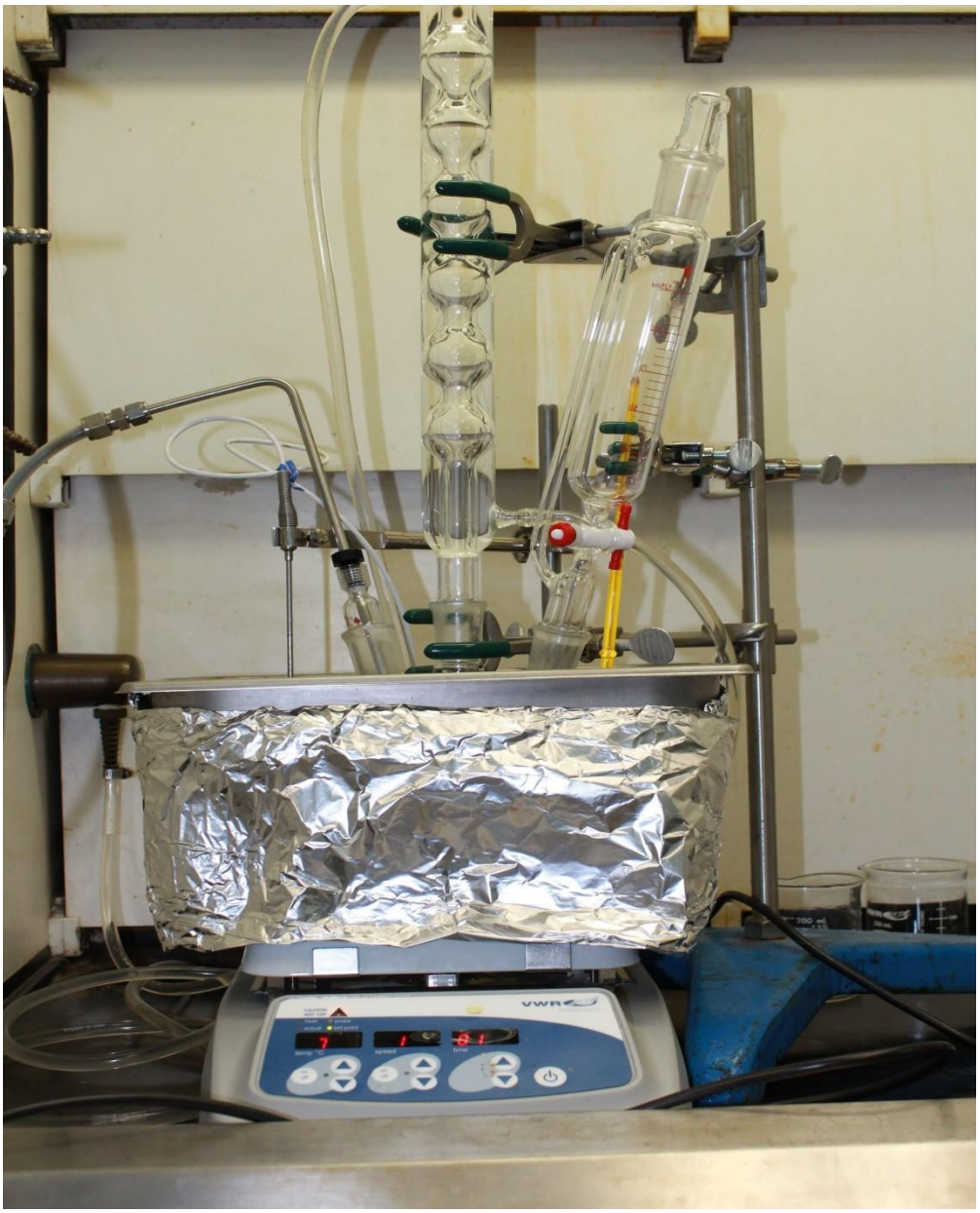

Figure B2: Experiment Setup for 5 um Polystyrene

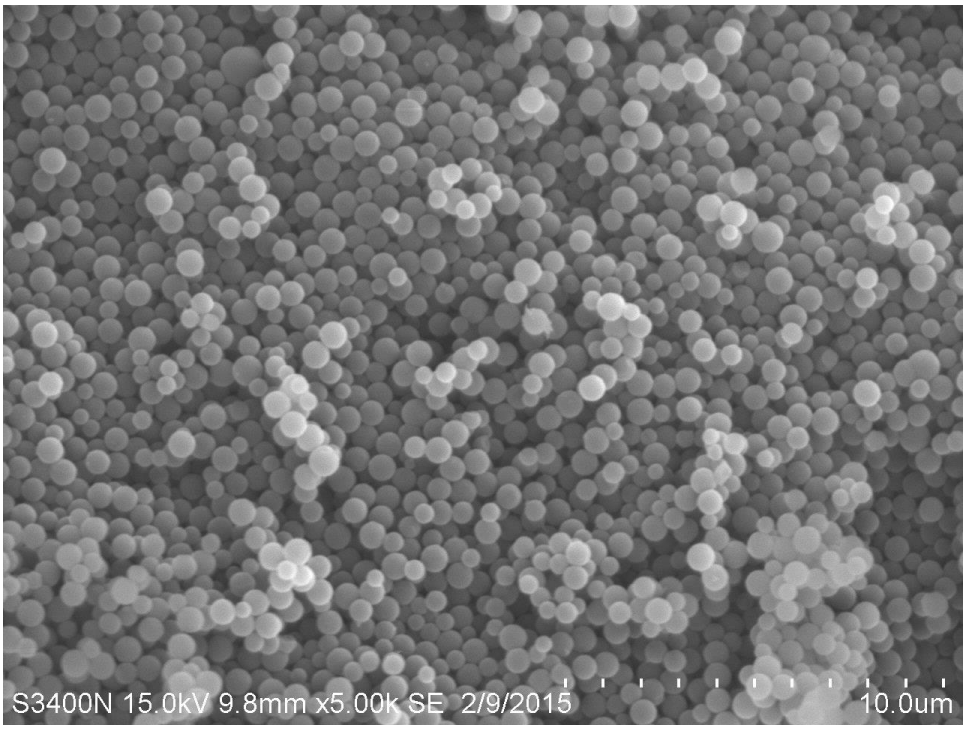

Figure B3: Digital Image of 0.5um Polystyrene

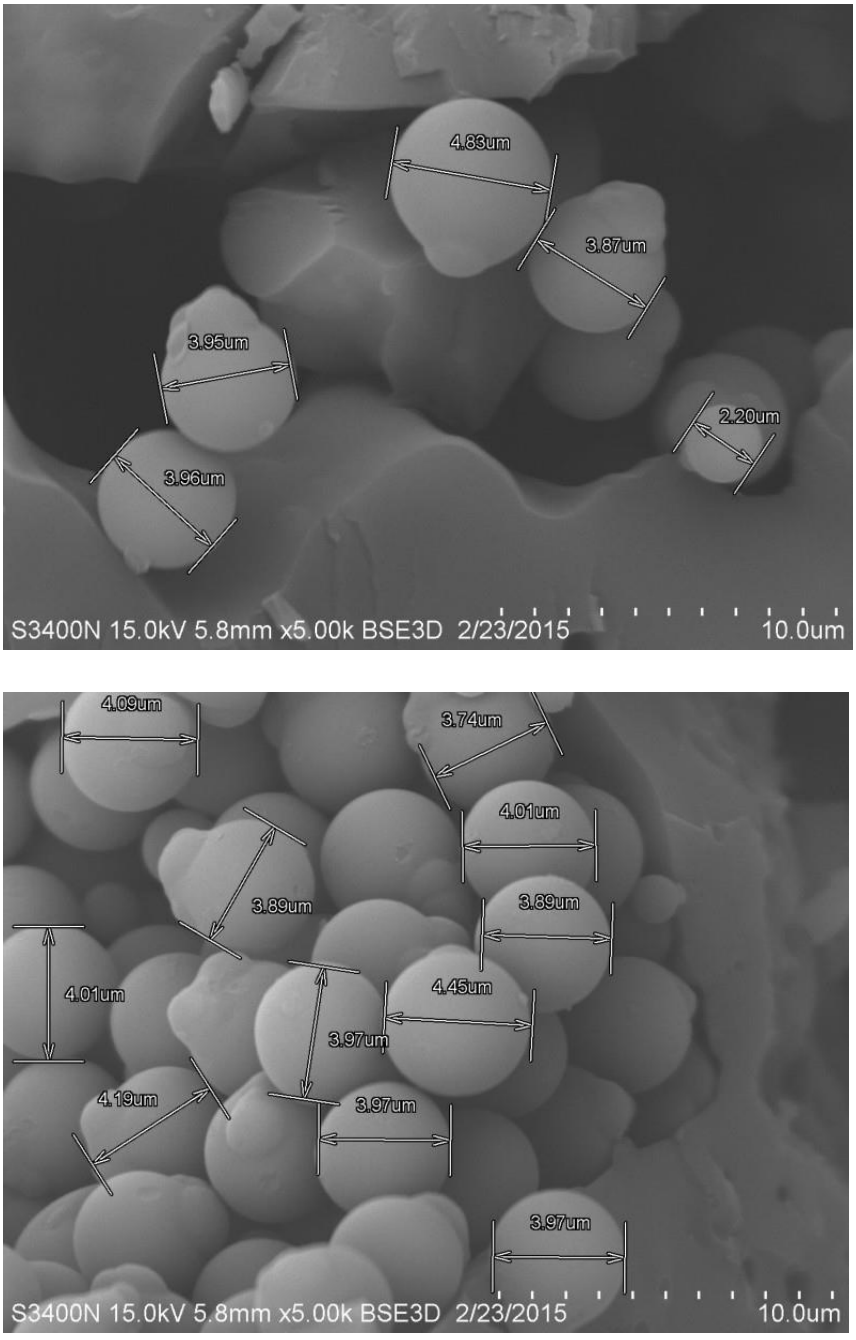

Figure B4: Two Digital Image of 5um Polystyrene-Chunk

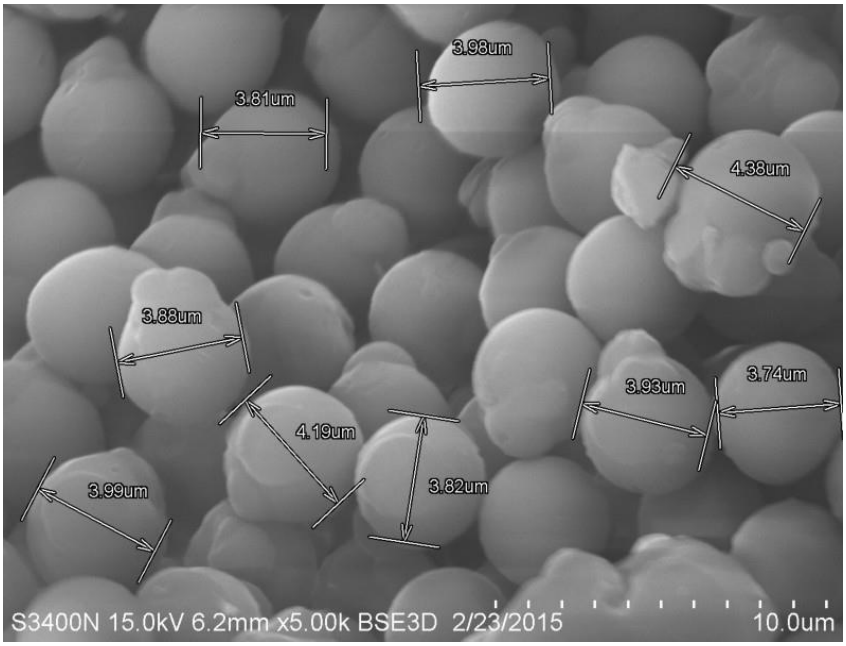

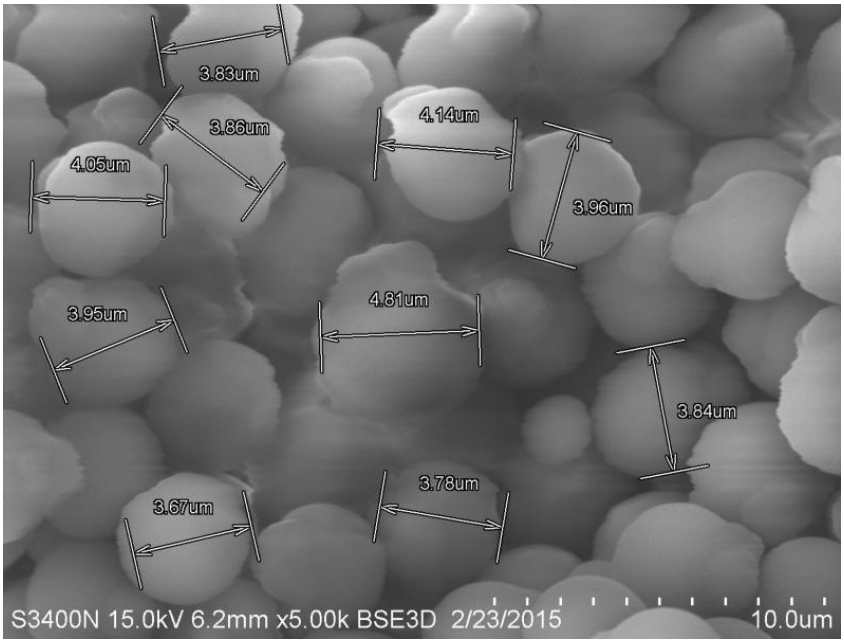

Figure B5: Two Digital Image of 5um Polystyrene-Power

Appendix C

C-Dot Characterization

Carbon nanodots (C-dots) have generated enormous excitement as a replacement for metal quantum dots because of their supremacy in water solubility, chemical inertness, low toxicity, and ease of functionalization [17]. Different methods to synthesize C-dots have been reported, but the recipes we follow are based on the single step pyrolysis method developed by Kryssmann et al [16]. The following two synthesis recipes have been used to generate C-dots in the 3-5 nm size range. In the cross-flow experiments, we use C-dots as a substitute for proteins and by using nanoparticles that are spherical, we are establishing a base experimental prediction of separation in this size range.

While the recipe to make these nanoparticles are straightforward, characterizing such small particles proved to be difficult. In addition, the original batch was made over a year ago, so characterization needed to be done to check if the sample degraded or the particles aggregated. The objectives of this characterization are to see if the original batch has degraded over time, if there are other species in the sample that are of different size, and if new batches made using the two synthesis methods can still produce particles in the 3-nm range.

Since the initial set of experiments using the 100 kDa membrane were conducted using the original batch, a dry sample was also imaged with a Cryo-TEM to see if there were still 3 nm particles present or if degradation or aggregation occurred. In addition to that, three new samples were synthesized and analyzed using the Malvern Zetasizer along with the original batch made over a year ago. Prior to analysis, the samples were also dialyzed to remove any intermediate products. The Zetasizer was used for both undialyzed and dialyzed samples.

Samples

1. **Original batch that was made over a year ago, in solution form**
2. **Solid form of a batch that was made on 12/1/16**
3. **Solid form of a batch that was made on 3/28/17**

Dialysis was done on all the samples including the original batch using a 3.5 kDa snakeskin membrane. Analysis was done to both the undialyzed and dialyzed samples. Along with using the Malvern Zetasizer, characterization of the samples using a spectrophotometer was done to ensure that fluorescent particles were present in the samples with the same excitation and emission properties as indicated by literature.

Zetasizer parameters and documentation

The instrument being used is the Malvern Zetasizer Nano ZS90 found in the CNET facility at Cornell University. This Zetasizer is an entry level system for the measurement of particle size and molecular size at a 90-degree scatter angle using Dynamic Light Scattering. The size range that can be measured is from 0.3 nm (diameter) to 5 microns. The C-dots are on the lower end of the scale, which can make it a little tedious to get good quality results as there is a larger range for noise from the instrument to affect the results and give incorrect results. To aid in observing particles in this size range, it is necessary to change the size range parameters in the measurement settings before starting a read on a sample. The screenshot shown below shows the screen where the size range parameters can be adjusted. If there are indeed particles detected outside this range, the equipment will output an error saying that there is insufficient signal to get a quality reading and then the range can be adjusted accordingly. It was found that setting the upper limit to 200 nm

was optimum for all the samples and didn't need to be adjusted. Having a high resolution will help in observing peaks with narrower ranges.

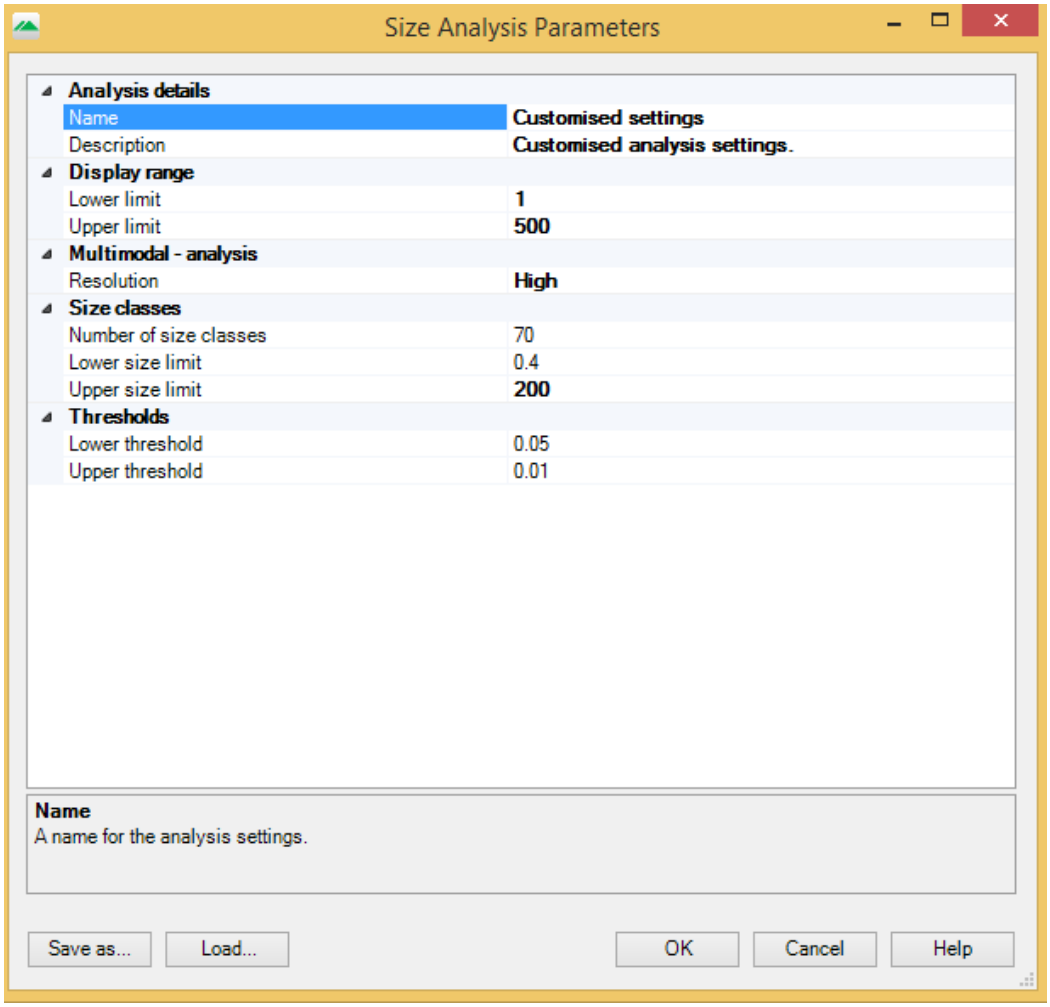

Figure C.1 Screenshot of the size analysis parameters set in the Malvern Zetasizer

Significant Zetasizer functions and terminology

There are three important parameters in the Zetasizer that help determine the quality of the data and whether it is reliable in predicting the size. When we look at the results of the C-dots, the following parameters are what we check to see if we can judge the results as reliable. The descriptions have been taken from the Malvern documentation on their website. [18,19]

Intensity – Dynamic light scattering techniques will give an intensity-weighted distribution, where the contribution of each particle in the distribution relates to the intensity of light scattered by the particle. When comparing the particle size data for the same sample measured by different techniques, it is important to stick to one type of distribution as each can produce very different particle size results. In our case, we want to stick to observing the intensity distribution peak and in the ideal case, there will only be a single peak corresponding to the size of the particle if the sample is indeed monodispersed.

PDI - The Polydispersity Index or PDI gives an indication of the width of the overall distribution and is dimensionless and scaled such that values smaller than 0.05 are rarely seen other than with highly monodisperse standards. Values greater than 0.7 indicate that the sample has a very broad size distribution and is probably not suitable for the DLS technique. This is an important standard to note as we want the PDI to be as low as possible to indicate that the sample is monodisperse. Also, having a PDI above 0.7 would indicate that the data quality/sample is not good.

Y-intercept or Intercept - In DLS the Y-Intercept or Intercept, refers to the intersection of the correlation curve on the y-axis of the correlogram. The y-intercept can be used to evaluate the signal-to-noise ratio from a measured sample and thus is often used to judge data quality. It is usually scaled such that an ideal signal will give a value of 1, and a good system will give intercepts more than 0.6, and greater than 0.9 for the best systems. For our data, we need to see an intercept value of greater than 0.6 to be able to assume that the quality of the data is good.

Analysis of Sample 1

Sample 1 was the original batch that was made using synthesis method 1 over a year ago. The dry powder obtained was dispersed in DI water and made up to a concentration of 96,000 ppm after being diafiltered using a 1 kDa membrane. A small sample was dried in powder form (no further dialysis was done using the 3.5 kDa membrane) and given for Cryo TEM imaging. A concentration of 0.4 mg/ml was made up and vortexed for 30s before plunge freezing occurred to prep the sample for the TEM. A few images of the sample under the microscope is shown below.

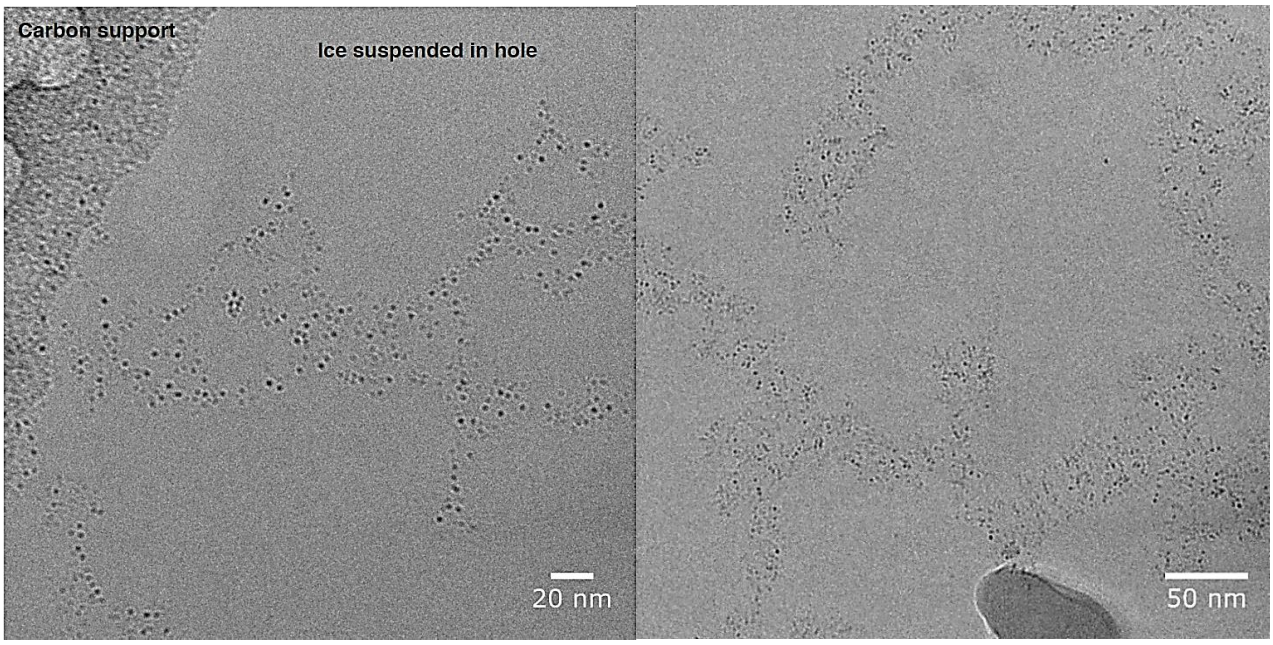

Figure C.2: Cryo-TEM images of the 3.4 nm C-dots

From the Cryo-TEM images, there is a clear presence of the nanoparticles in ice in the grid holes. It was a bit difficult to find the particles on the grid, but this can be rectified by using a higher concentration of particles. The measured size of these particles was on average 3 nm.

The absorbance and fluorescence spectra of both the undialyzed and dialyzed sample was taken to ensure that there was a presence of fluorescent particles. The spectrum curves are shown

in Figures C.3 and C.4 for absorbance to determine the peak excitation wavelength and the fluorescence emission spectrum at the determined excitation wavelength for all the samples.

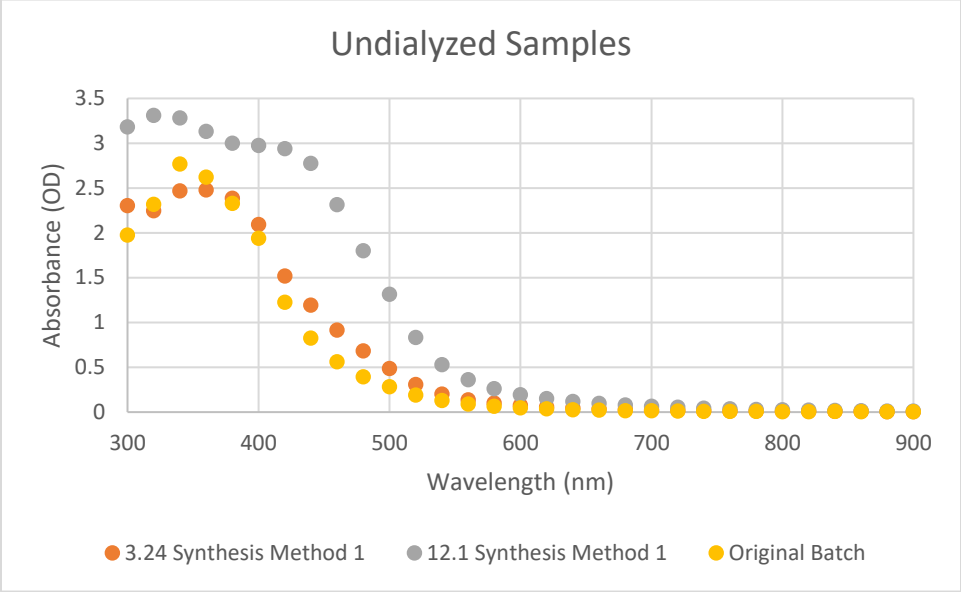

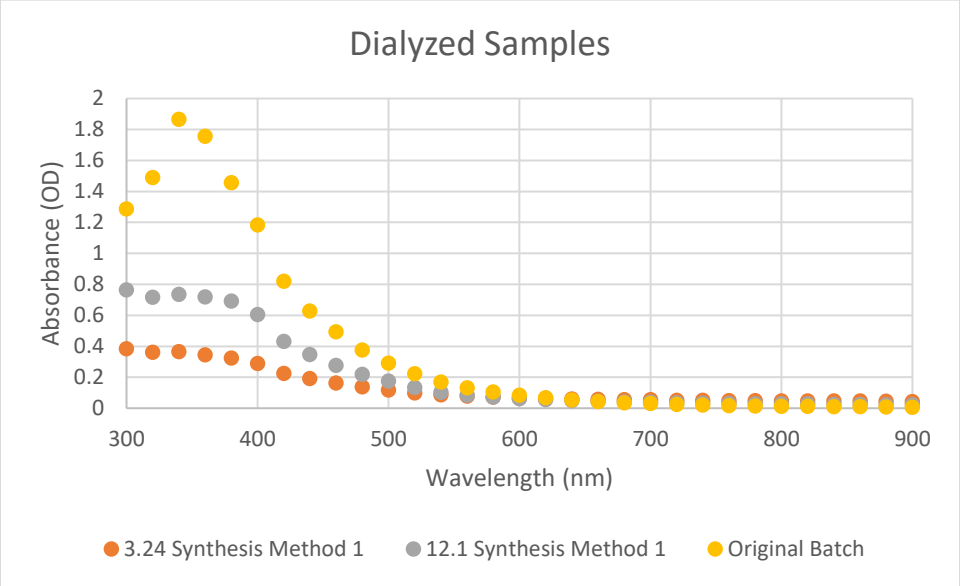

Figure C.3: Absorbance spectra of the undialyzed (top) and dialyzed (bottom) samples

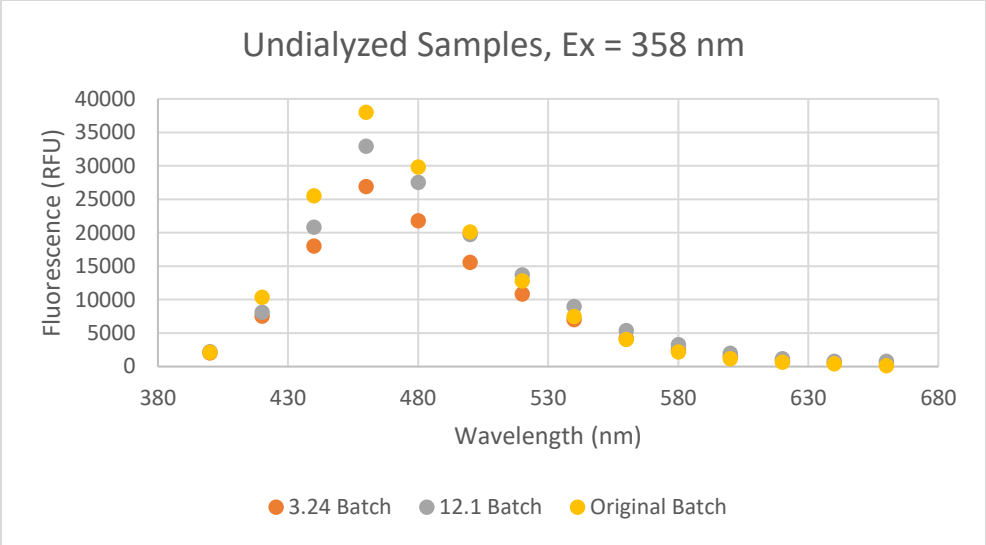

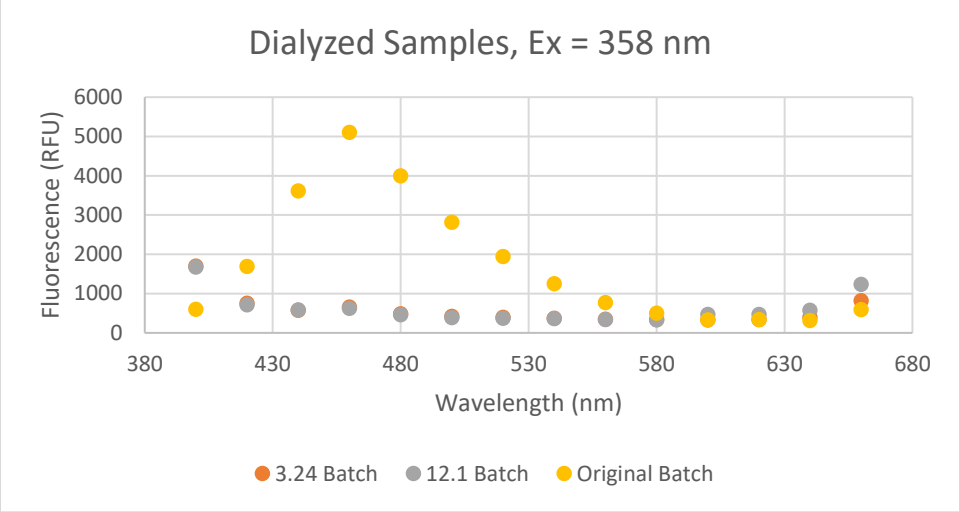

Figure C.4: Emission spectra at a fixed excitation wavelength of 358 nm for both undialyzed (top) and dialyzed (bottom) samples

The size of the particles was characterized using dynamic light scattering techniques with the Zetasizer. It is still a work in progress to optimize the three parameters in the Zetasizer that are important to get a reliable measure of size of the particles. There is still some difficulty in bringing down the PDI further and increasing the intercept value to above 0.6, but the values are close and provides a baseline in showing that the DLS can be used to detect particles in the sample that are in the correct size range.

Temperature (°C):	20.0			**Duration Used (s):**	50
Count Rate (kcps):	158.2			**Measurement Position (mm):**	3.00
Cell Description:	Disposable micro cuvette (40µl)			**Attenuator:**	11

			Size (d.nm):	**% Intensity:**	**St Dev (d.nm):**
Z-Average (d.nm):	160.5	**Peak 1:**	210.6	77.4	65.33
PdI:	0.348	**Peak 2:**	50.13	13.4	9.343
Intercept:	0.272	**Peak 3:**	3.661	9.3	0.3945
Result quality :	Refer to quality report				

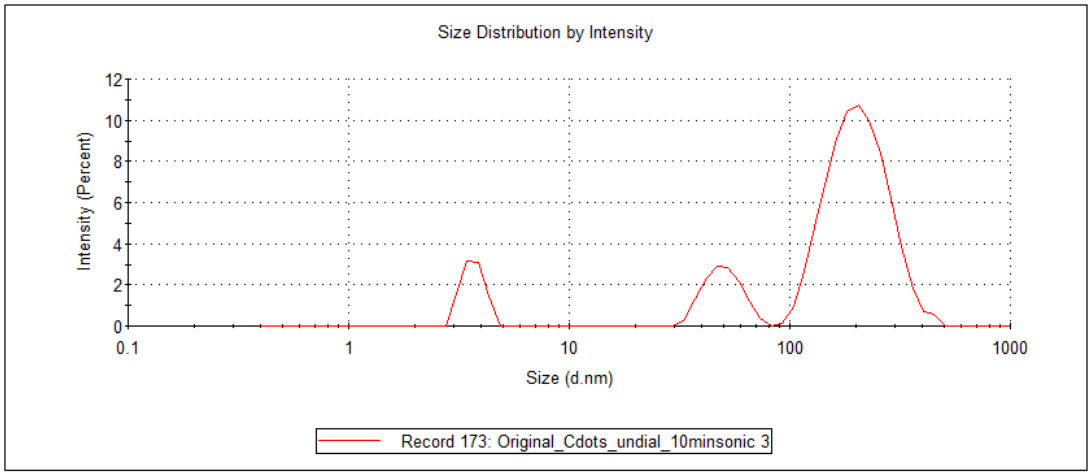

Figure C.5: DLS intensity distribution of the undialyzed sample 1

Shown in Figure C.5 is the DLS analysis of the undialyzed sample of C-dots. The intensity distribution has a peak in 3.6 nm size range, which shows us that there is a presence of this size particles in the sample.

Going further and looking at the number distribution shows a single peak with a size of 3.4 nm as shown in Figure C.6. What can be inferred from this is that even though there are additional peaks of 50.1 nm and 210.6 nm in the intensity distribution, the number of particles in that size is negligible compared to the number of 3.4 nm particles, which could indicate that what's in that size range can be dust or some obstruction on the cuvette. Ideally, we only want to see one peak in the intensity distribution and a higher intercept value, but efforts are being made to see if adjusting the concentration of the sample can give better quality distributions.

Temperature (°C):	20.0	**Duration Used (s):**	50
Count Rate (kcps):	158.2	**Measurement Position (mm):**	3.00
Cell Description:	Disposable micro cuvette (40µl)	**Attenuator:**	11

		Size (d.nm):	**% Number:**	**St Dev (d.nm):**
Z-Average (d.nm):	160.5	**Peak 1:**	3.438	100.0	0.4430
PdI:	0.348	**Peak 2:**	0.000	0.0	0.000
Intercept:	0.272	**Peak 3:**	0.000	0.0	0.000

Result quality : **Refer to quality report**

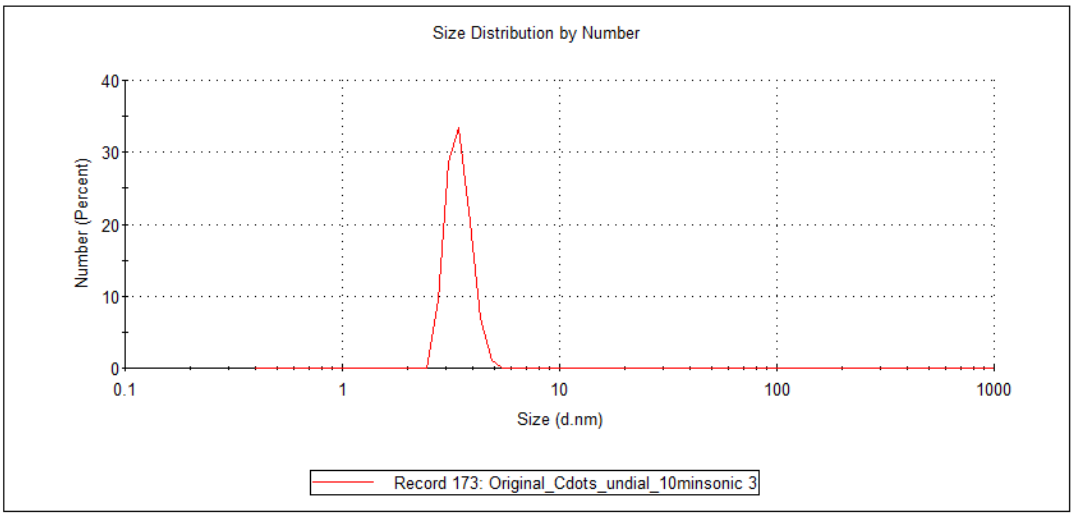

Figure C.6: DLS number distribution of the undialyzed sample

The same analysis is done for the dialyzed sample. Shown in Figures C.7 and C.8 are the intensity and number distributions respectively. In this analysis, the intercept value is almost 0.6, however there are additional peaks. Again, we ideally want to see only a single peak in the 3-nm size range.

Additionally, the same techniques were followed for Samples 2 and 3. Samples 2 and 3 were batches made using the same synthesis method, with one being made a couple of weeks ago and one being made a few months ago. The rest of the report documents the figures and graphs showing the size characterization of each sample using the Zetasizer.

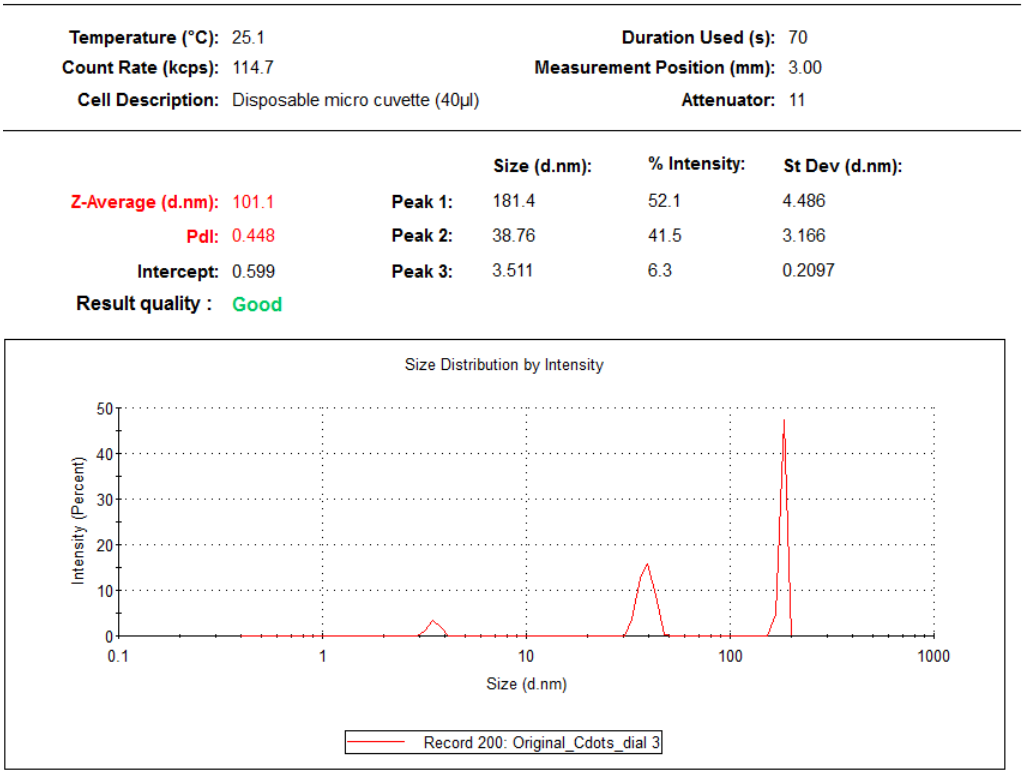

Figure C.7: DLS intensity distribution of the dialyzed sample 1

Temperature (°C):	25.1	**Duration Used (s):**	70
Count Rate (kcps):	114.7	**Measurement Position (mm):**	3.00
Cell Description:	Disposable micro cuvette (40µl)	**Attenuator:**	11

		Size (d.nm):	**% Number:**	**St Dev (d.nm):**
Z-Average (d.nm): 101.1	**Peak 1:**	3.442	100.0	0.3013
PdI: 0.448	**Peak 2:**	0.000	0.0	0.000
Intercept: 0.599	**Peak 3:**	0.000	0.0	0.000

Result quality : Good

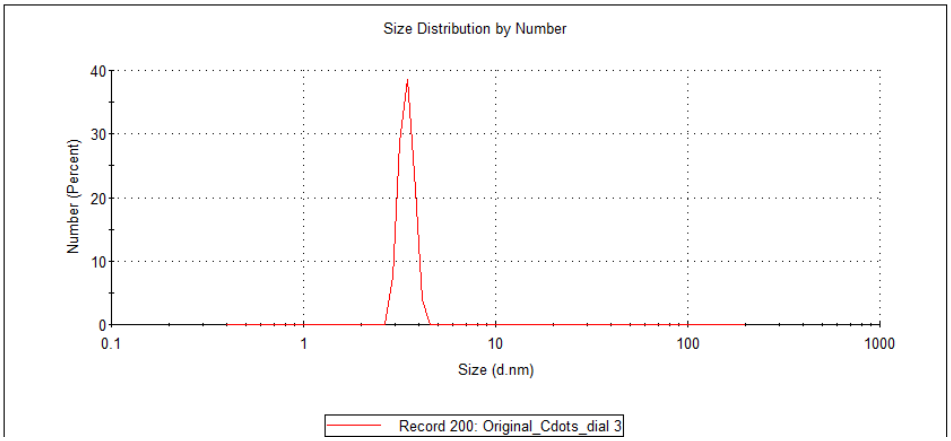

Figure C.8: DLS number distribution of the dialyzed sample 1

Analysis of Sample 2

Temperature (°C):	25.0	**Duration Used (s):**	50
Count Rate (kcps):	74.3	**Measurement Position (mm):**	3.00
Cell Description:	Disposable micro cuvette (40µl)	**Attenuator:**	11

			Size (d.nm):	**% Intensity:**	**St Dev (d.nm):**
Z-Average (d.nm):	121.2	**Peak 1:**	4.926	100.0	0.3041
PdI:	0.646	**Peak 2:**	0.000	0.0	0.000
Intercept:	0.311	**Peak 3:**	0.000	0.0	0.000

Result quality : Refer to quality report

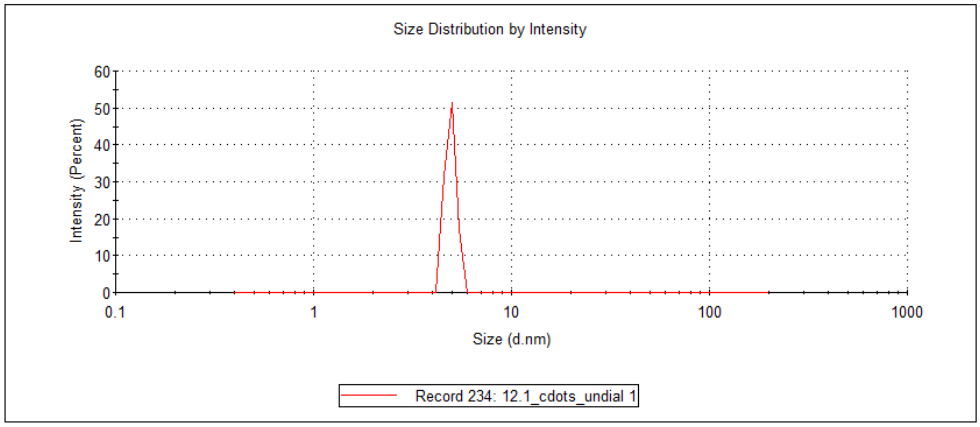

Figure C.9: DLS intensity distribution of the undialyzed sample 2

Temperature (°C):	25.0	**Duration Used (s):**	50
Count Rate (kcps):	74.3	**Measurement Position (mm):**	3.00
Cell Description:	Disposable micro cuvette (40µl)	**Attenuator:**	11

			Size (d.nm):	**% Number:**	**St Dev (d.nm):**
Z-Average (d.nm):	121.2	**Peak 1:**	4.830	100.0	0.4178
PdI:	0.646	**Peak 2:**	0.000	0.0	0.000
Intercept:	0.311	**Peak 3:**	0.000	0.0	0.000

Result quality : Refer to quality report

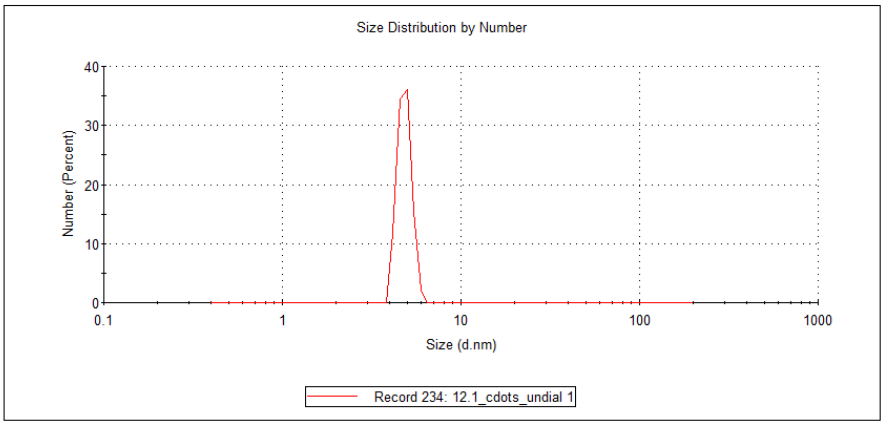

Figure C.10: DLS number distribution of the undialyzed sample 2

Temperature (°C):	24.9	**Duration Used (s):**	80
Count Rate (kcps):	41.5	**Measurement Position (mm):**	4.65
Cell Description:	Disposable sizing cuvette	**Attenuator:**	11

			Size (d.nm):	**% Intensity:**	**St Dev (d.nm):**
Z-Average (d.nm):	105.4	**Peak 1:**	87.74	93.6	28.57
PdI:	0.390	**Peak 2:**	4.244	6.4	0.3511
Intercept:	0.396	**Peak 3:**	0.000	0.0	0.000

Result quality : Refer to quality report

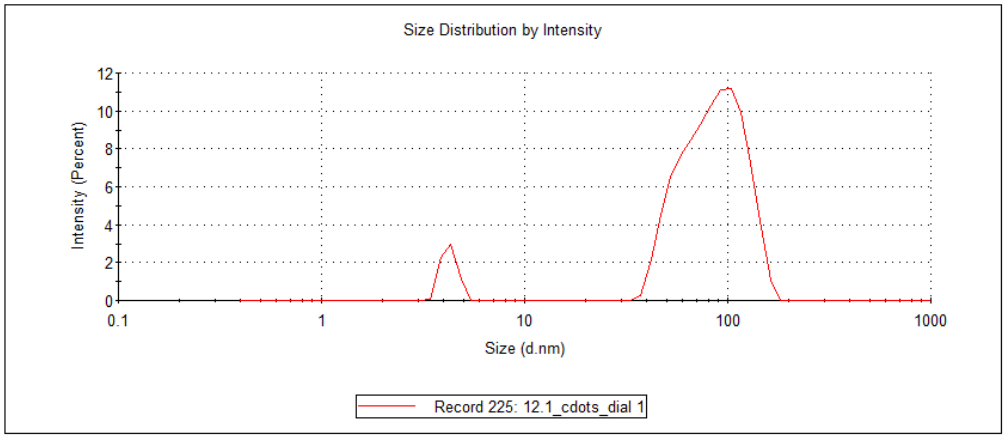

Figure C.11: DLS intensity distribution of the dialyzed sample 2

Temperature (°C):	24.9	**Duration Used (s):**	80
Count Rate (kcps):	41.5	**Measurement Position (mm):**	4.65
Cell Description:	Disposable sizing cuvette	**Attenuator:**	11

			Size (d.nm):	**% Number:**	**St Dev (d.nm):**
Z-Average (d.nm):	105.4	**Peak 1:**	4.098	100.0	0.4560
PdI:	0.390	**Peak 2:**	0.000	0.0	0.000
Intercept:	0.396	**Peak 3:**	0.000	0.0	0.000

Result quality : Refer to quality report

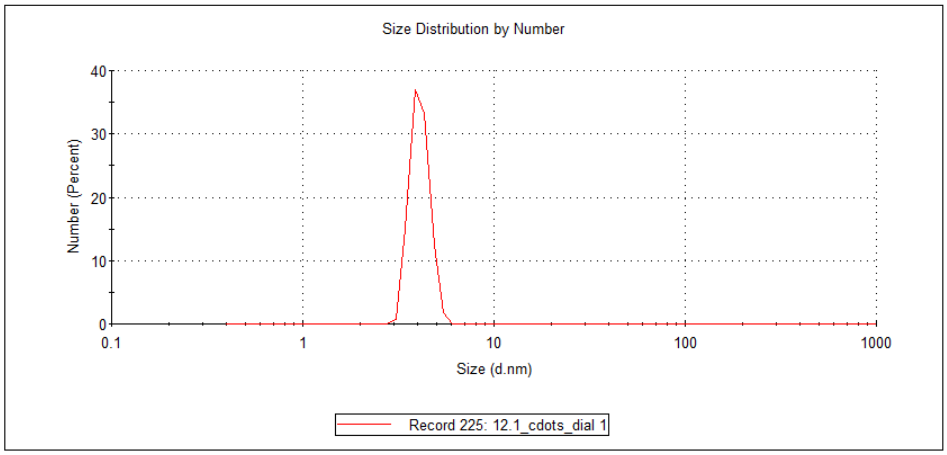

Figure C.12: DLS number distribution of the dialyzed sample 2

Sample 2, which was the batch made a few months ago, shows a similar trend as the original batch that was made over a year ago. The size of the particles still fall in the 3-5 nm range and we can see that in the intensity and number distribution using the Zetasizer. Further improvements can be made to see if the quality of data can be improved by increasing the intercept value and bringing down the PDI value even further.

Analysis of Sample 3

Temperature (°C):	20.0			**Duration Used (s):**	50
Count Rate (kcps):	55.5			**Measurement Position (mm):**	3.00
Cell Description:	Disposable micro cuvette (40µl)			**Attenuator:**	11

			Size (d.nm):	**% Intensity:**	**St Dev (d.nm):**
Z-Average (d.nm):	167.3	**Peak 1:**	123.2	82.7	19.39
PdI:	0.374	**Peak 2:**	21.90	11.8	2.624
Intercept:	0.399	**Peak 3:**	4.008	5.5	0.3926
Result quality :	Refer to quality report				

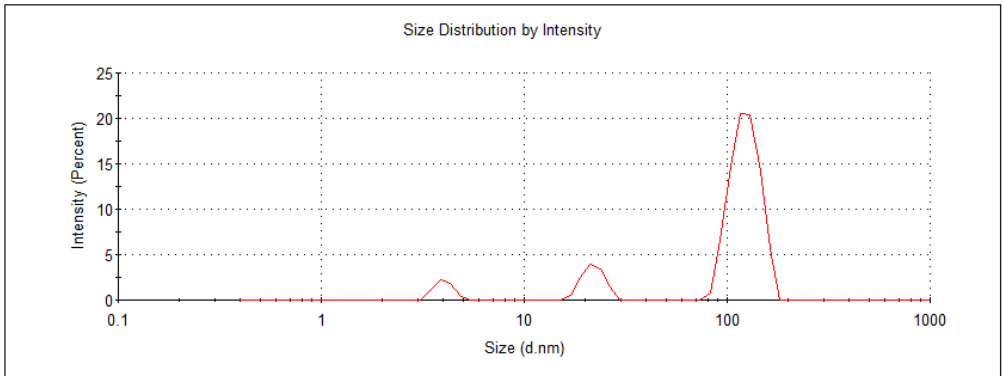

Figure C.13: DLS intensity distribution of the undialyzed sample 3

Temperature (°C):	20.0	**Duration Used (s):**	50
Count Rate (kcps):	55.5	**Measurement Position (mm):**	3.00
Cell Description:	Disposable micro cuvette (40µl)	**Attenuator:**	11

			Size (d.nm):	**% Number:**	**St Dev (d.nm):**
Z-Average (d.nm):	167.3	**Peak 1:**	3.812	100.0	0.4617
PdI:	0.374	**Peak 2:**	0.000	0.0	0.000
Intercept:	0.399	**Peak 3:**	0.000	0.0	0.000

Result quality : Refer to quality report

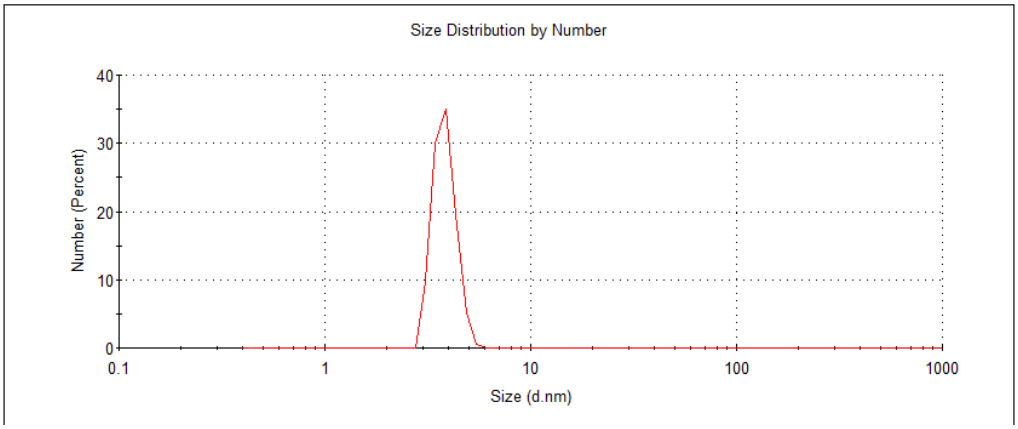

Figure C.14: DLS number distribution of the undialyzed sample 3

Temperature (°C):	20.0	**Duration Used (s):**	50
Count Rate (kcps):	66.6	**Measurement Position (mm):**	3.00
Cell Description:	Disposable micro cuvette (40µl)	**Attenuator:**	11

			Size (d.nm):	**% Intensity:**	**St Dev (d.nm):**
Z-Average (d.nm):	173.6	**Peak 1:**	144.2	79.7	25.52
PdI:	0.434	**Peak 2:**	31.17	13.6	3.451
Intercept:	0.410	**Peak 3:**	3.955	6.6	0.2776

Result quality : Refer to quality report

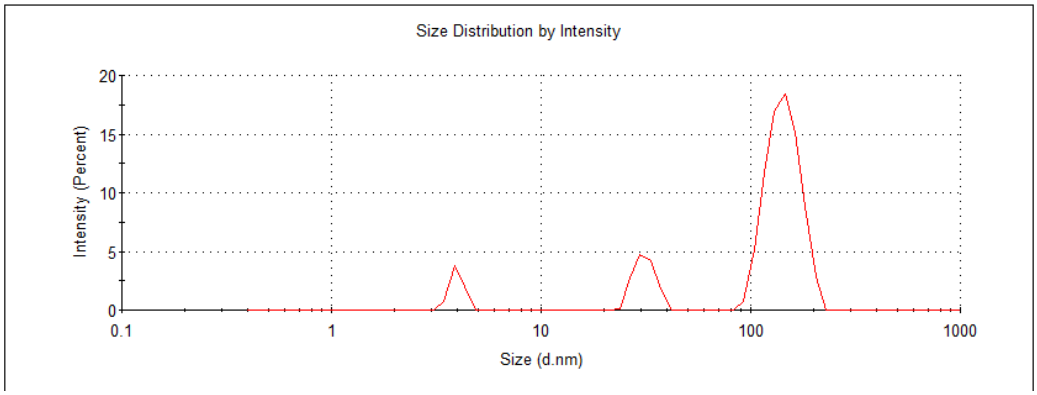

Figure C.15: DLS intensity distribution of the dialyzed sample 3

Temperature (°C):	20.0	**Duration Used (s):**	50
Count Rate (kcps):	66.6	**Measurement Position (mm):**	3.00
Cell Description:	Disposable micro cuvette (40µl)	**Attenuator:**	11

			Size (d.nm):	**% Number:**	**St Dev (d.nm):**
Z-Average (d.nm):	173.6	**Peak 1:**	3.850	100.0	0.4137
PdI:	0.434	**Peak 2:**	0.000	0.0	0.000
Intercept:	0.410	**Peak 3:**	0.000	0.0	0.000

Result quality : Refer to quality report

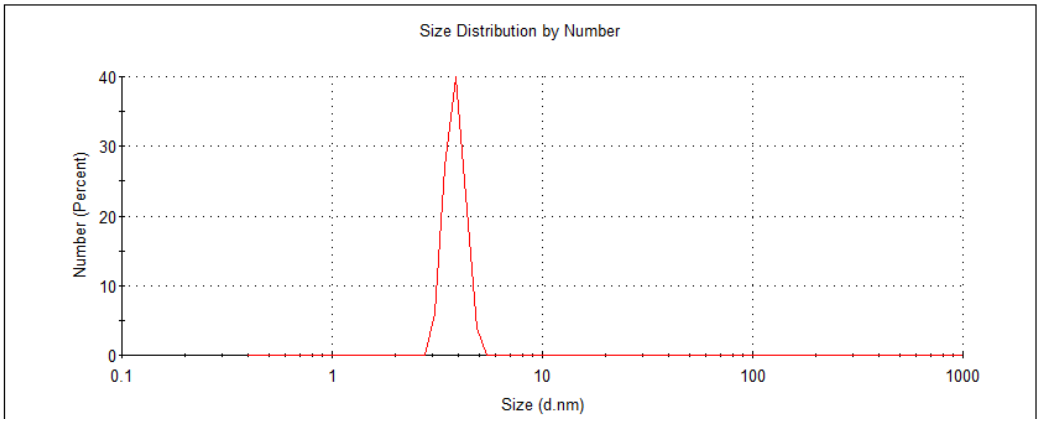

Figure C.16: DLS number distribution of the dialyzed sample 3

Summary of Results

1. By optimizing the parameters in the Zetasizer to focus on scattering the sample to get small sizes, we can show that 3 nm particles can be detected
    a. We can identify and set the important parameters in the Zetasizer that are needed to obtain an accurate representation of the size of particles in the solution
    b. The intercept value from the Zetasizer is still not above 0.6 for the data that shows an intensity peak in the 3-nm range, but optimization of the settings is still in progress.
2. We can consistently synthesize the same sized particles using the synthesis method published in literature
    a. The size measurements obtained from the Zetasizer can be backed up with images obtained from a Cryo-TEM microscope for the original sample

3. Absorbance and fluorescence spectra measurements show fluorescence with excitation at 358 nm and emission at 450 nm, which is consistent with the literature
4. While the Zetasizer is showing that there are particles in the 3-5 nm size range, further optimization of the sample and parameters need to be done to achieve better quality results.
    a. The main issue is bringing up the intercept value (decreasing the signal to noise ratio).
        i. One solution offered to this in literature is to change the concentration of the sample to improve the value.
        ii. Another solution mentioned is to add a little bit of surfactant to improve the dispersion and minimize the signal to noise ratio
    b. Ideally want only a single intensity distribution peak in the 3-5 nm range. This was achieved for some of the samples, but still needs to be done for the rest
        i. The larger sizes shown could be due to some imperfection or dust on the cuvette

REFERENCES

[1] Koros WJ, Ma YH, Shimidzu T (June 1996). "Terminology for membranes and membrane processes (IUPAC)". *Pure & Appl. Chem.* 86 (7): 1479–1489.

[2] Belfort, G., Davis, R.H., Zydney, A.L. 1994 The behavior of suspensions and macromolecular solutions in cross-flow filtration. *J. Membrane Sci.* **96**, 1.

[3] http://www.xtractfiltrationsystems.com/sites/default/files/shared/crossflow_diagram.png

[4] van der Smann, R.G.M. and Vollebregt, H.M. 2013 Transient critical flux due to coupling of fouling mechanisms during crossflow microfiltration of beer. *J. Membrane Sci*. **435**, 21.

[5] Davis, R.H. and Leighton, D.T. 1987 Shear-induced transport of a particle layer along a porous wall. *Chem. Eng. Sci.* **42**, 275.

[6] Davis, R.H. and Sherwood, J.D. 1990 A similarity solution for steady-state cross-flow microfiltration. *Chem. Eng. Sci.* **45**, 3204.

[7] Drew, D.A., Schonberg, J.A. and Belfort, G. 1991 Lateral inertial migration of a small sphere in fast laminar flow through a membrane duct. *Chem. Eng. Sci.* **46**, 3219.

[8] van Dinther, A.M.C., Schroën, C.G.P.H. and Boom, R.M. 2011, High-flux membrane separation using fluid skimming dominated convective fluid flow, *J. Membrane Sci.* **371**, 20.

[9] Levesley, J.A. and Bellhouse, B.J. 1993 Particulate separation using inertial lift forces. *Chem. Eng. Sci.* **48**, 3657.

[10] Hurwitz, M.F. and Brantley J.D. 2000 Shear separation: A promising method for protein fractionation. *Lait* **80**, 121.

[11] van Dinther, A.M.C., Schroën , C.G.P.H. and Boom, R.M. 2013 Separation process for very concentrated emulsions and suspensions in the food industry, *Innovative Food Science and Emerging Technologies* **18**, 177.

[12] G. K. Batchelor. (2000). *An Introduction to Fluid Dynamics*. Cambridge Mathematical Library. Cambridge: Cambridge University Press. pg. 202, eqn. 4.5.7.

[13] Hermann Schlichting, Klaus Gersten (2004), Boundary Layer Theory, 8th ed. Springer-Verlag

[14] Yan, Z.-Y., Acrivos, A. and Weinbaum, S. 1991 Fluid skimming and particle entrainment into a small circular side pore. *J. Fluid Mech.* **229**, 1.

[15] *Zisman, W.A. (1964). F. Fowkes, ed. Contact Angle, Wettability, and Adhesion. ACS. pp. 1 51*

[16] A.B. Bourlinos, R. Zboǐil, J. Petr, A. Bakandritsos, M. Krysmann, E.P. Giannelis. Luminescent surface quaternized carbon dots. Chem Matter, 24 (1) (2012), pp. 6–8

[17] Y. V. Li, L. M. Cathles, and L. A. Archer, Nanoparticle Tracers in Calcium Carbonate Porous Media, Journal of Nanoparticle Research, 2014, 16(8), 1-14.

[18] A basic guide to particle characterization. http://www.malvern.com/en/support/resource-center/Whitepapers/WP120620BasicGuidePartChar.aspx

[19] Dynamic light scattering - common terms defined.

http://www.malvern.com/en/support/resourcecenter/Whitepapers/WP111214DLSTermsDefined.aspx

[20] Koch, D. Employing hydrodynamic lift and particle trajectory ratcheting to achieve sieve-free separation based on size and shape in cross-flow filtration. NSF Proposal, June 2015

[21] Ravelet, F., Delfos, R.. & Westerweel, J. 2010 Influence of global rotation and Reynolds number on the large-scale features of a turbulent Taylor–Couette flow. Phys. Fluids 22, 055103

[22] Rainer Höfer, Franz Jost, Milan J. Schwuger, Rolf Scharf, Jürgen Geke, Josef Kresse, Herbert Lingmann, Rudolf Veitenhansl and Werner Erwied "Foams and Foam Control" Ullmann's Encyclopedia of Industrial Chemistry, 2000, Wiley-VCH, Weinheim. doi:10.1002/14356007.a11_465

[23] Feilden, Ezra (2016). *"Robocasting of structural ceramic parts with hydrogel inks"*. Journal of the European Ceramic Society. Elsevier BV. **36** (10): 2525–2533. *doi:10.1016/j.jeurceramsoc.2016.03.001*. *Retrieved 2017-02-23*.

[24] Long, B.R., Hller, M., Beech, J.P., Linke, H., Bruus, H., and Tegenfeldt, J.O. 2008 Multidirectional sorting modes in deterministic lateral displacement devices. *Phys. Rev. E* **78**, 046304.

[25] Wang, Yi. (2015). *Preparationof Highly Crosslinked Monodisperse Polystyrene Microspheres by Dispersion Polymerization.* (Report No. AM-D3-013396). Cortland, NY. Pall Corporation Technical Report.

[26] Cheng, N. S. (2008). “Formula for viscosity of glycerol-water mixture.” Industrial and Engineering Chemistry Research, 47, 3285-3288.